URBAN SURFACE TEMPERATURE RETRIEVAL FROM SPACE THROUGH EMISSIVITY CLASSIFICATION

by

HYO JIN AHN

A dissertation submitted to the Graduate Faculty in Earth and Environmental Sciences in partial fulfillment of the requirements for the degree of Doctor of Philosophy, The City University of New York

2008

This manuscript has been read and accepted for the
Graduate Faculty in Earth and Environmental Sciences in satisfaction of the
dissertation requirement for the degree of Doctor of Philosophy.

Professor Karl-Heinz Szekielda

February 6, 2008 — Karl Heinz Szekielda

Date — Chair of Examining Committee

Professor Yehuda L. Klein

3/4/2008 — Yehuda L Klein

Date — Executive Officer

Professor Allan Frei

Professor Edward Hindman

Professor Karl-Heinz Szekielda
Supervisory Committee

THE CITY UNIVERSITY OF NEW YORK

ABSTRACT

URBAN SURFACE TEMPERATURE RETRIEVAL FROM SPACE THROUGH EMISSIVITY CLASSIFICATION

by

Hyo Jin Ahn

Adviser: Professor Karl-Heinz Szekielda

Deriving accurate surface temperatures from satellite remote sensing data for urban environment and climate studies is problematic because it requires at least 10 to 15 m spatial resolution with pre-knowledge of emissivity information. This research focused on developing new techniques for the enhancement of spatial resolution to a 15 m urban surface temperature mapping through image fusion, improving classification accuracy, and application of classified emissivity and atmospheric corrections. The major findings are as follows:

1. In enhancing spatial resolution of Landsat 7 Enahnced Thematic Mapper Plus (ETM+) to 15 m pixel size, the principal component spectral sharpening and the Gram-Schmidt sharpening provide the best result with the least distortion of the original spectral properties. The consequent classification product by maximum likelihood classifier shows an overall accuracy of 97% and a Kappa coefficient of 0.82 by increased number of input bands including three principal components, and twelve ratio bands.

2. As a part of classification accuracy test, the Scaled Difference Vegetation Index (SDVI) method shows an efficient quantitative analysis for vegetation estimation within less than 0 to 0.4% deviations.

3. For deriving the ETM+ surface temperature from its radiance data, applying the emissivities retrieved from the Advanced Spaceborne Thermal Emission and Reflection Radiometer (ASTER) at the wavelength region 10.95–11.65 μm is superior to those from the wavelength region 10.25-10.95 μm.

4. The cross examination shows that 0.30 ºC higher by ETM+ surface temperature and 0.55 ºC higher by ASTER surface temperature than the buoy measurements of sea surface temperatures (SSTs), but both measurements are acceptable at the 95% confidence interval. The comparison between ASTER and Moderate Resolution Imaging Spectroradiometer (MODIS) shows that the MODIS LST underestimates the average 3.8 ºC. This new approach provides an improvement over existing techniques that retrieve surface temperature based on single or few levels of surface emissivities.

Therefore, semi-automated approaches in the retrieval of urban surface temperatures using the enhanced pixel resolution of Landsat ETM+ thermal data based on differentiated surface emissivity classes with the atmospheric correction parameter sets show that it is possible to establish a mapping with surface temperature database in its accuracy up to 96% relative to the ASTER surface temperatures.

DEDICATION

I dedicate this dissertation to my mother and the late grandmother for their endless sacrifice, love, hope, and belief with showing me the greatness comes only through the misery.

ACKNOWLEDGEMENTS

I would like to take opportunity to express my sincere gratitude to Professor Yehuda Klein for his continuous support. My very special thanks go to Professor Allan Frei, who guided my research work and allowed me to use his laboratory and facilities continuously. I would also like to thank Professor Edward Hindman for the constructive comments and guidance on my thesis work.

Finally, this dissertation would not have been possible without the guidance and encouragement of my advisor Professor Karl Heinz Szekielda. His enormous patience, unconditional trust, and endless support helped me finish this dissertation.

TABLE OF CONTENTS

List of Tables

List of Figures

1. Introduction

Urban areas account for about 3% of the total land areas of Earth (Global Rural-Urban Mapping Project 2005). The extent of urban areas may not seem to be significant enough to draw attention. However, recent estimates by Global Rural-Urban Mapping Project indicate that the increasing rate of urban areas is at least 50% over previous estimates that urban areas were 1 to 2% of the Earth's total land area. The global proportion of urban population projects that 60% of the world's population will be city dwellers by 2025 (United Nations 2006). Considering this anticipated high concentration of population in urban areas and its increasing rate, the importance of understanding and accurately assessing urban environments and climatic variations has to be incorporated into future planning and development of urban areas.

Surface temperature is a prime parameter to study urban climatology. With the advent of thermal infrared (TIR) remote sensing technology, remote sensing-based temperature measurements became available. The significant advantages of satellite image sensors are their ability to cover large areas on a routine basis that lead to large archives (Ben-Dor 2001). For studies on Earth's radiation budget and climate change detection, or mapping surface temperature from global to local scales, TIR remote sensing data have been superior to the data obtained by point measurements on the ground (Dash *et al*. 2002).

Coarse spatial resolution data of about 1 km that are recorded with space-borne thermal remote sensors by the National Oceanic and Atmospheric Administration (NOAA) such as the Advanced Very High Resolution Radiometer (AVHRR) and the Moderate Resolution Imaging Spectrometer (MODIS), have been extensively used for

global or continental scale surface temperature mapping (Price 1983; Wan and Dozier 1996; Pinheiro et al. 2006), or for the comparisons of the surface temperature distributions between urban heat islands and rural areas (Roth *et al*. 1989; Gallo *et al.* 1993).

Moderate spatial resolution data from the Landsat Thematic Mapper (TM) TIR band with a spatial resolution of 120 m, have been used for small region or urban scale studies such as observation of mesoscale surface temperature differences between urban and rural areas (Carnahan and Larson 1990; Kim 1992), mapping air quality parameters related to surface temperature in a city (Wald and Baleynaud 1999), or detecting urban-induced surface temperature change over time at a local level (Weng 2001).

The Landsat 7 ETM+ TIR band with a 60 m spatial resolution and the ASTER with five thermal bands at 90 m spatial resolution, have shown a great improvement in their accuracy in radiometric measurements through more advanced calibrations. This includes improvements to assess urban thermal patterns based on their relation to urban biophysical descriptors i.e., impervious surface, green vegetation, and soil, and the thermal feature fractions (Lu and Weng 2006), and to evaluate urbanization influences on urban surface radiant temperature (Xian and Crane 2004).

Although considerable research was performed since 1972 to use remotely sensed thermal information for detection of thermal characteristics of urban areas, the progress has been relatively slow. Reasons are the coarse or moderate spatial resolution of thermal imagery that has limited capability of discerning complex urban areas and the deficiency of fundamental surface descriptors, such as the types of materials, emissivity, and structural features (Voogt and Oke 2003).

Recommended optimal resolution to resolve spatially individual urban surfaces associated with their thermal energy regimes is between 10 m and 20 m (Small 2001), or finer than 15 m (Gorsevski *et al*. 1998). The only space-borne TIR remote sensing system is the Multispectral Thermal Imager (MTI) with a 20 m resolution, but the data from this measurement are not available in the public domain.

At present, most of the high spatial resolution TIR images at a 5 m to 15 m resolution are available from airborne remote sensing systems, such as the Thermal Infrared Multispectral Scanner (TIMS), the Advanced Thermal and Land Application Sensor (ATLAS), the Multispectral Infrared and Visible Imaging Spectrometer (MIVIS), the MODIS ASTER (MASTER) airborne simulator, and the Spatially Enhanced Broadband Array Spectrography System (SEBASS). Most of these data are costly and available only by special acquisition request. For example, the airborne Thermal Infrared Multispectral Scanner (TIMS) data at 5 m resolution were used for the project ATLANTA-urban heat island study, and supportive to improve differentiation of the thermal behavior of seven discrete urban surfaces (Quattrochi and Ridd 1994). The Advanced Thermal and Land Applications Sensor (ATLAS) provided detailed thermal signatures corresponding to ten major land cover classes with two to five sub-classes (Lo *et al.* 1997). However, these analyses showed only the estimation of blackbody radiance temperature, or irradiance variations but not the actual physical surface temperature associated with surface covers. Detailed information of a physical descriptor, especially surface emissivity, is essential to retrieve actual surface temperature corresponding to differentiated urban surface covers. Very few studies attempted to retrieve the surface

temperature in conjunction with detailed observations of individual urban surface emissivity (Artis and Carnahan 1982).

This study focuses on improving (1) the understanding between urban thermal patterns and discrete urban surface cover types, and (2) the techniques to retrieve urban surface temperature from satellite measured TIR. To accomplish an improved surface temperature retrieval method at 15 m spatial resolution using Landsat 7 ETM+ TIR data, two investigations are the center of this study:

1) Identifying detailed emissivity values in each urban surface covers, and

2) Enhancing spatial details of urban surface temperature.

The experimental design for those investigations is based on two assumptions. The first is that the identification and classification of each discrete urban surface cover type can be improved by using data fusion products. The products are based on combined moderate resolution multispectral Landsat 7 ETM+ image layers and a high resolution panchromatic image in addition to some ancillary image fusion products from 1 m IKONOS data and 70 cm QuickBird data. The other assumption is that the accuracy of urban surface temperature can be improved by the application of detailed urban surface emissivity values as well as a model based atmospheric correction.

Finally, to validate the new technique results are cross examined with ground truth data from sea surface measurements and satellite observation data based on ASTER and MODIS LST.

2. Background

2.1. Thermal Remote Sensing of Urban Areas

Remote sensing derived biophysical attributes provide great potential for establishing parameters describing urban construction materials and the composition and structure of urban canopies. This is important for improving the understanding of urban surface energy budgets, and observing the urban heat island (UHI) effect. Utilization of thermal remote sensing for studies of land surface temperatures and urban energy budget characteristics has been growing since the knowledge of urban surface energy budgets and urban climatology is important for planning and management practices (Weng and Quattrochi, 2006).

The characteristics of urban areas in the aspect of thermal distribution have been studied in the urban heat islands fields. Roth *et al*. (1989) observed that the greatest differences in surface radiant temperature between urban and rural regions appear during midday, while the greatest air temperature differences occur at night. Their results also indicate that night time urban-rural differences and intra-urban variability in surface temperatures are much smaller than during day time. This finding associated with the higher minimum surface temperature in urban area has been interpreted by Gallo *et. al.* (1993), that heat contributions may be from the sides of buildings and the characteristics of other urban features. Roth *et al*. (1989) also state that the heat islands intensity is more tied to the degree and type of urban development in the city center than of population.

The relationship between urban heat island effects and vegetation cover has been extensively assessed based on vegetation indices such as the NDVI (Gallo *et al.* 1993; Lo *et al.* 1997; Owen *et al*. 1998). For example, Gallo *et al*. (1993) show that satellite

observed NDVI is linearly related to the differences in observed urban and rural minimum temperatures. It indicates that the difference in the NDVI between urban and rural regions is an indicator for the difference in surface properties such as evaporation and heat storage capacity. A more detailed description about the relationship between NDVI and the irradiance of land cover categories was described by Lo *et al*. (1997). Their research used a 5 m high spatial resolution airborne TIR data from ATLAS, which was able to provide very detailed irradiance and NDVI descriptions of 34 classified land use and land covers in Huntsville, Alabama. The land use and land cover classes used in their study are based on the United States Geological Survey (USGS) land use/land cover classification Level III and Level IV, which rely on land usage or utility types, not absolute physical and chemical material types. Their findings show that the irradiance values of highly detailed land use and land cover (Level III/IV) are lowered by the association with biomass. According to their results, land surface irradiances are lowering from vacant/transitional, residential, agricultural and vegetation cover. A problem in the analysis based on the relation between land surface temperature and NDVI is that NDVI does not provide aerial estimates of the amount of vegetation (Small 2001, 2004).

Most of the urban heat islands studies used qualitatively based land use data and not quantitative urban surface descriptors (Voogt and Oke 2003; Weng *et al*. 2006). To understand the urban heat island effects and advance studies related to climatic change and urban ecosystems, quantitatively based surface physical or biophysical property data are required. To accomplish quantitative urban studies, assessment of adequate scales of thermal remote sensors is necessary. Studies by Pu *et al* (2006) which focused on the

assessment of the relationship between LST and NDVI, show that the MODIS thermal data can be used for the synoptic inventory of an urban thermal environment. They indicate that the ASTER thermal data allow for an accurate determination of thermal patterns and properties of urban land use/land cover types whereas the Thermal Airborne Broadband Imager data of 2-m resolution can be used for more detailed distribution of LST at the individual house level.

Gluch *et al*. (2006) studied urban thermal pattern, which included an analysis of thermal properties of individual land covers in a multi-scale approach at the micro scale (community level) and the mesoscale (regional level). Their study was based on total energy upwelling radiance for a given surface, but did not convert the data to surface temperature. Their results show that airborne ATLAS data at spatial resolution of 10-m performed well in community level studies in terms of land cover and thermal exchange but found that Landsat TM data are more appropriate for large areas.

The important physical properties in urban areas, which are essential to represent land surface processes, are surface temperature, surface albedo, surface emissivity, vegetation cover, and surface structure or roughness (Jin and Peters-Lidard 2005). The most evident urban surfaces are dominated by impervious covers such as concrete, cement, asphalt, tar, bricks, shingles, metals, or glasses. Natural surfaces like vegetation and bare soil in urban areas are relatively small and are highly fractionized. The transformations of urban surfaces affects the surface energy dynamics, resulting in a higher solar radiation absorption, a change in thermal capacity and a conductivity that contribute to the creation of urban heat island and consequent deterioration of urban air quality (Weng 2001).

In an urban scheme study for a land surface model, Jin and Peters-Lidard (2005) state that man-made urban surfaces enhance sensible heat flux, upwelling longwave radiation, overlaying atmospheric instability and convective clouds and rainfall, but decrease urban surface albedo, emissivity, and ground heat flux. These integrated effects have had affect local weather patterns such as heavy precipitation over or downwind of cities in the late afternoon (Shepherd *et al.* 2002).

A limited number of studies have shown quantitative assessments of urban surfaces related to their physical or biophysical character. Urban biophysical descriptors, low and high albedo of impervious surfaces, vegetation cover, and soil from the ASTER visible infrared and short wave infrared bands, and hot-and cold-object from the ASTER TIR bands have been extracted using linear spectral mixture analysis technique (Lu and Weng 2006). It was shown that land surface temperature possess a stronger positive correlation with the hot-objects such as impervious surface than with the cold-objects wherein the classified surfaces are commercial, high-density residential, forest, and agricultural area.

Using airborne remote sensing high spatial resolution (HSR) imagery, both urban heat island source and quantitative assessment of the thermal behavior of each urban surface material became also possible by its high spectral resolution, which enable to capture the individual urban target or feature (Ben-Dor and Saaroni 1997; Ben-Dor 2001). High spatial resolution imagery obtained from airborne remote sensing Thermal Video Radiometer (TVR) has been used to assess the thermal behavior of Tel-Aviv urban surfaces in relation to surface materials (Ben-Dor and Saaroni 1997). Their result demonstrates that one of the major components adding heat to a city is non-shaded

asphalt. The study by Ben-Dor (2001) shows much detailed thermal fluxes, surface temperature, albedo, sensible flux, latent heat flux, ground heat flux, absorbed solar radiation flux, and Soil Adjusted Vegetation Index (SAVI) over the city of Beit Shean and Afula, Israel. The results reveal how each urban target contributes to the urban heat island phenomenon.

Some recent urban heat estimates have been focused on the three-dimensional (3-D) roughness of urban environment (Nichol 1998; Voogt and Oke 1997; Voogt and Grimmond 2000). Nichol and Wong (2005) used a satellite-based method for 3-D structural details of the built environment including vertical walls, which can be applied at both micro-and city-wide scales. Their approach was based on the assumption that the resolution convergence of a high spatial resolution and a moderate spatial resolution satellite data permits the use of satellite data to represent the urban thermal environment by depicting the complete radiating surface involved in energy exchange between the surface and the atmosphere. In this study, a Landsat ETM+ thermal image was fused with a 4 m spatial resolution IKONOS image, and combined with a 3-D Virtual Reality model. The model was constructed from digital data of building outlines and calculated building heights and adding vertical surfaces as 3-D facets and weighted horizontal surfaces. One limited fact in this study is that they used only two different levels of urban surface emissivities namely for vegetation 0.96 and for non-vegetation 0.92.

Stathopoulou *et al*. (2007) indicates that the emissivity values of typical man-made materials on urban environments range from 0.40 to 0.98 in the thermal region of the Landsat TM band 6 (10.5-12.5μm) as referred the ASTER spectral reflectance library data. Their study demonstrated that it is possible to derive urban surface emissivity using

Landsat data in combination with the modified NDVI thresholds method. The approach was based on estimating mean emissivity values for selected urban/non-urban land cover types by using different computations in function of three NDVI value intervals. Since most of past urban thermal studies did not apply emissivity values for discrete surface covers due to technical difficulty of gaining surface emissivity values, the study provided improvement of urban thermal studies to derive accurate LST estimates. However, considering the limits of the NDVI method that usually overestimates the abundance of interspersed non-park vegetation relative to more densely vegetated areas in parks (Small 2001), it still contains uncertainty or LSE estimates with the applied three NDVI values. Other possible errors in their study could be also in the assigning emissivity values that were derived from the ASTER spectral library data. In addition their surface classification classes, which contained some grouped land use categories, did not represent sole land cover type.

Based on the recognized problems and limitations identified in previous research, this study will develop a new technique in order to derive detailed and realistic urban surface emissivity map on the basis of land cover types.

2.2. Spectral Characteristics of Urban Surface Material

This section reviews the spectral data that are required for monitoring and differentiating of surfaces that are typical for urban environments. It is known that high spatial resolution information is used more as a pattern recognition tool than as a source of information about the material's nature and composition (Ben-Dor 2001). Since characterization of urban radiance and reflectance requires quantification of both spatial

and spectral variability across a range of scales, detailed spectral characteristics of urban surfaces also require high resolution spectral information.

Urban areas represent a variability of surfaces that are based on both their physical and chemical composition that define the absorption and reflectance properties. When light interacts with a substance, light of certain wavelengths are preferentially absorbed while others are transmitted in the substance (Van Der Meer 2001). When photons encounter a surface, several different processes are involved in their absorption and reflection. The variety of absorption processes and their wavelength dependence reveal information about the chemistry of each material from its reflected or emitted light. The total remote sensing reflectance of a given object across the entire visible region is related to the physical condition of the relevant targets such as shadowing effects, slope and aspect, particle size and their refraction index. Spectral absorption features are more related to the chemical condition of the sensed target that leads to specific peaks and troughs (Clark 1999; Ben-Dor 2001).

Absorption by surfaces in the visible-near infrared region is governed by electronic processes, and the absorption in the shortwave infrared region is dominated by the combination and overtone modes of vibrational process (Hunt 1977; Clark 1999; Abrams *et al*. 2001). Position, shape, depth, and width of these absorption features are controlled by particular crystal structure and by the chemical structure of the material, characterizing absorption features that are the direct expression of a specific substance (Van Der Meer 2001). In order to capture these diverse absorption features by sensor devices, it is necessary to know the spectroscopic properties of a target.

Electronic transitions produce broad absorption features that require higher energy levels than do vibrational processes, and therefore take place at shorter wavelengths in the visible and near-infrared regions (Hunt 1970). Most surfaces containing iron, hydroxyl, sulfate, water and carbonate minerals display diagnostic spectral features in the visible and near infrared wavelength region by the product of electronic processes (Hunt 1980; Abrams *et al.* 2001).

Vibrational processes, which are small displacements of the atoms about their resting positions, produce fundamental overtone absorptions (Hunt 1977). A vibrational absorption appears in the infrared spectrum only if the molecule responsible shows a dipole moment (Clark 1999). CO_2 absorbs at 2.01 μm and 2.08 μm, and has a weak doublet near 1.60 μm. The major atmospheric water absorption features are located approximately at 0.97 μm, 1.19 μm, 1.45 μm, 1.94 μm, and 2.7 μm in the near infrared through mid infrared region (Clark 1999). The atmospheric absorption above the 3 μm region is mainly due to water, O_2, CO_2, and O_3.

Some natural objects such as water bodies and vegetations in the urban areas can be distinguished with even coarse and discrete types of remote sensing sensors based on their different spectral signatures. However, it is challenging to identify and quantify different types of manmade objects with moderate resolution space-borne remote sensing data, having very similar spectral reflectance patterns in urban areas. Some of previous studies presented alternative approaches or combined techniques to deal with this issue.

High spectral resolution information is available through imaging spectrometry or Hyperspectral Remote Sensing (HSR) sensors which cover both the reflective visible (0.4 to 0.7 μm), near infrared (0.7 to 1.1 μm), shortwave infrared (1.1 to 2.5 μm) and thermal

infrared (3 to 14 μm) spectral regions. HSR represents targets better with respect to their physical effects and chemical compositions than does laboratory produced spectral library information (Ben-Dor 2001).

A synthetic spectral library, the Pure Spectra Urban Spectral Library (PUSL) by Ben-Dor (2001) was generated based on comparing the Price's library data with the in-situ measurements of a HSR, Compact Airborne Spectrographic Imager (CASI). This alternative approach permits better accuracy of the spectral recognitions of urban targets due to the fact that it takes into consideration the atmospheric environment. There is also an expanded spectral library that covers the spectral region from the visible to the shortwave infrared and is built from in-situ measurements using the Analytical Spectral Devices (ASD) (Ben-Dor 2001).

In addition to integrating spectral library information, use of a sophisticated classification technique is another important key for the successful HSR application in urban environmental analysis (Ben-Dor 2001). The small urban structures and the high spectral information content of the hyperspectral image data require special methods capable of dealing with the resulting large number of mixed pixels. Segl and Roessner (1999) and Roessner *et al.* (2001) developed a new technique with pixel-oriented endmember selections to overcome mixed pixel problem and lead to more sensible differentiation over mixed urban surfaces. Their comparison with standard linear spectral unmixing method shows that pixel- and context-based method performs a reasonable area wide differentiation of urban surfaces. Related to the mixed pixel problems of urban surfaces, Small (2001) showed the applicability of linear spectral mixture models to quantify New York City's vegetation using multispectral image Landsat TM data. The

results indicate that the dimensionality of reflectance in the New York City area may be represented by a three component linear mixing model. An enhanced identification capability for complex urban objects having similar reflectance was possible by using this extended HSR measurement database. One of the samples collected by Ben-Dor (2001) uses the ASD measurements and shows good differentiations among impermeable paved materials

Furthermore, using a database generated from the HSR measurements that cover the entire spectral region from the visible to the thermal infrared is a desirable way to extract accurate urban surface spectral information. Unfortunately, there is no published spectral profile database representing the entire spectral region from the visible to the thermal infrared based on field measurements of urban targets. However, there are published spectral library data that are based on laboratory measurements covering the thermal infrared region for manmade materials. For example, the ASTER spectral library provides an integrated database from three other spectral libraries: the Johns Hopkins University (JHU) Spectral Library, the Jet Propulsion Laboratory (JPL) Spectral Library, and the USGS Spectral Library.

Several spectral profiles representing typical urban targets are shown in Figure 2.2 that covers the region from the visible to the thermal infrared region for manmade materials. They were generated from the ASTER Spectral Library-JHU Spectral Library data.

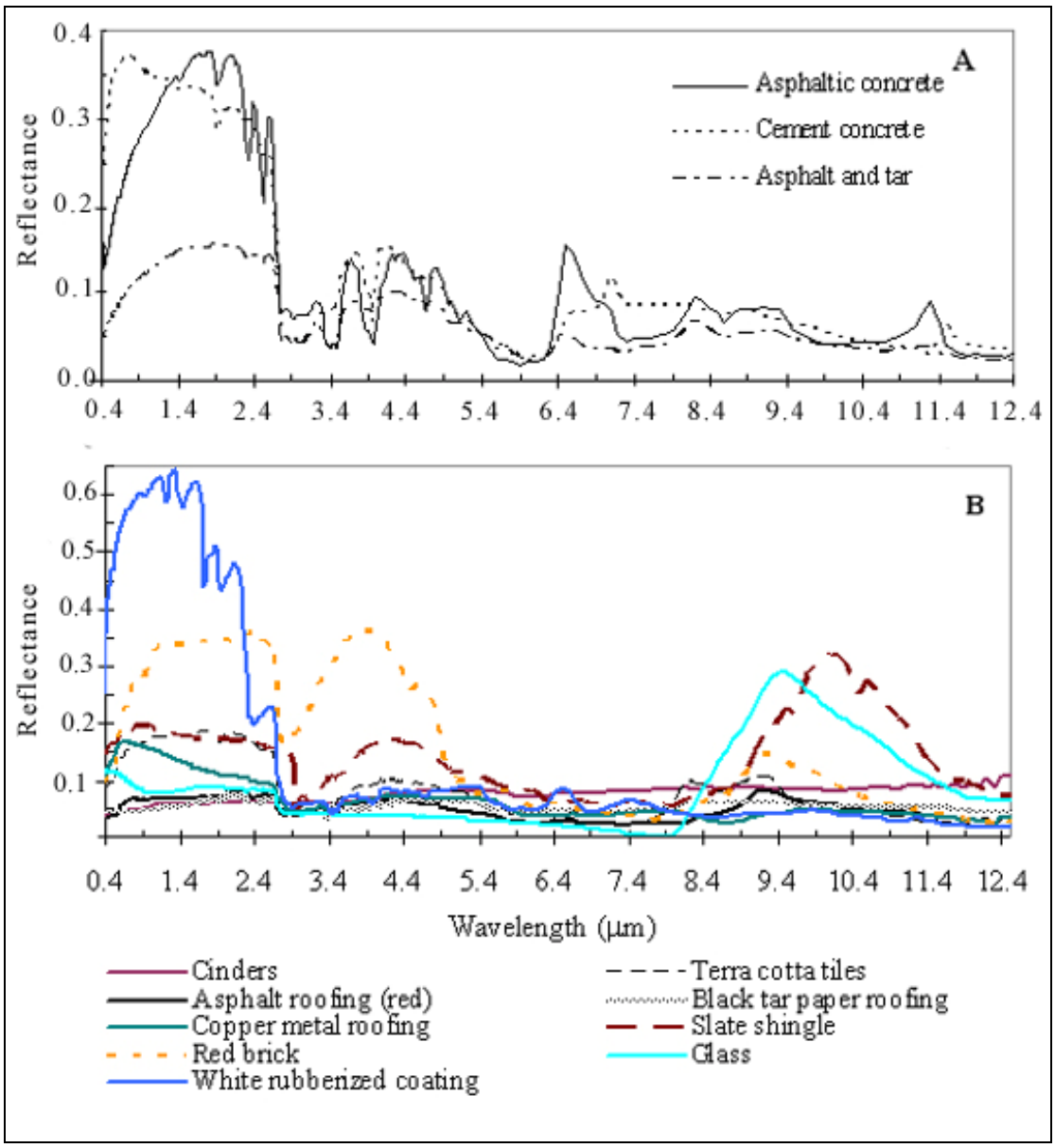

Figure 2.2. Spectra of urban construction materials generated from the ASTER Spectral Library originally in text file at the Johns Hopkins University Spectral Library.

Diagram in Figure 2.2.A shows the typical spectral profiles of impervious paved surfaces such as asphalt and tar roads, paved parking areas, and cement concrete covered streets. Asphalt mixed with tar shows the lowest reflection and emission throughout the entire spectral region. The comparison between asphalt pave and cement concrete pave demonstrates that cement concrete pave material emits slightly higher reflective radiance than asphalt and tar pavements in the thermal wavelength regions between 6.4 to 7.0 μm and 10.40 to 11.40 μm.

Figure 2.2.B represents spectral profiles of roofing materials. In the visible to the shortwave infrared region, reflectance and emittance levels of roofing materials show good separation except for asphalt roofing, cinder and black tar paper roofing. Distinct emittance features in the mid infrared and thermal infrared regions are also noticeable in the spectra for red brick and slate shingles. The spectral profile of white rubberized coating surfaces has very high reflectance in the visible as well as in the shortwave infrared. Glass materials, with increasing trends in their usage of most high-rising building constructions in urban areas, show another unique reflectance and emittance feature in the visible through to the mid infrared regions. They have relatively low values but increasing emittance of about 30% at around 9 μm.

In order to select the proper spectra for target detection, several concepts have to be considered. In spectrometry, spectral band and bandwidth, the central wavelength, response sensitivity at the edges of a band, spectral sensitivity at outer wavelengths and sensitivity of polarization are used to describe the feature in a spectrum. The spectral response of a sensor describes the spectral bandwidth, which is the width of an individual spectral band. The instrument response is defined as the Full Width at Half Maximum

(FWHM) and refers to the spectral resolution. To determine the spectral resolution, the shape of the band-pass profile corresponding to the response sensitivity is important. Spectral sampling is the distance in wavelength between the spectral band-pass profiles for each band as a function of wavelength. To resolve two spectral features without getting sampling bias, the samples must be close enough together to measure the peak and valley locations (Clark 1999).

3. Study Area and Data Sources

The study area as shown in Figure 3 is part of the New York Metropolitan Area, which includes the City of New York and the northeastern part of New Jersey. The total land area of New York City is 785.6 km^2 with a housing density of 4,074.6 per km^2. Water area covers 428.8 km^2, which corresponds to 35.1% of the overall New York City area (United States Census 2000).

The study area in New Jersey included parts of Bergen, Passaic, Essex, Union, Middlesex County and the entire Hudson County. Bergen county is noticeable by a well-developed road network, including the northern termini of the New Jersey Turnpike and the Garden State Parkway, the eastern terminus of Interstate 80 and a portion of Interstate 287, US Highways 46, 202, 9, 9W, and New Jersey State highways 4, 17, 3, 120, 208, and the Palisades Interstate Parkway. Referring to the census data 2000, the county has a total area of 162 km² that is composed of 121 km² land and 41 km² of water. Hudson County has an extensive road and freeway network, connecting the county's communities to the rest of New Jersey and the New York metropolitan area. An estimated one million commuters travel through Hudson County daily. Essex County has a total area of 336

km², which is composed of 327 km² of land and 9 km² of water. Union County has a total area of 273 km², 268 km² of it is land and 6 km² of it is water. Middlesex County has a total area of 835 km² of which 802 km² is land and 33 km² is water (United States Census 2000).

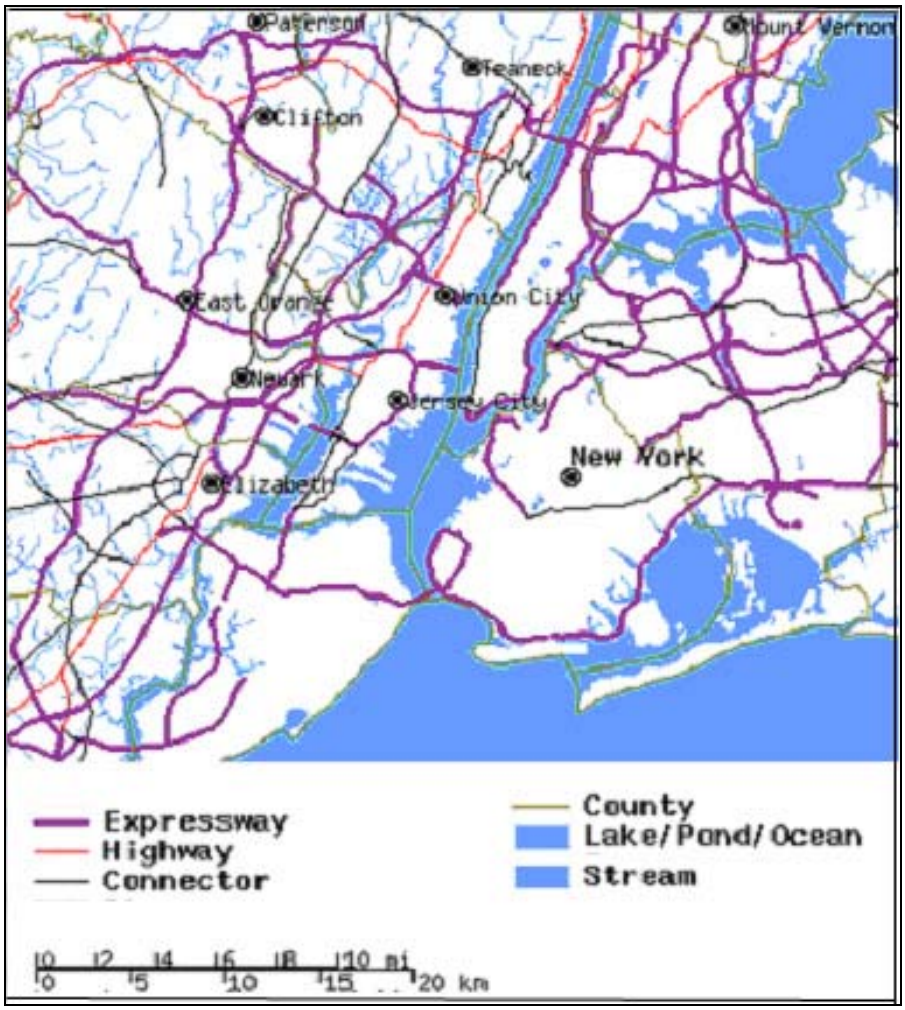

Figure 3. The base map in the study area, Source: The United States Census 2000 Tiger file.

In this study, Landsat 7 ETM+, ASTER, and MODIS images were analyzed. One of the most critical factors in the selection of satellite data for this study was the search for images that overlap with the closest acquisition time at the same date. In addition, cloud free condition was another defining factor in data selection. Based on the above two restrictions, the following satellite image data that were identified and analyzed are shown in Table 3.1. In addition to the satellite images, several ancillary data sets were used for detailed urban surface type identification and as ground truth data for the accuracy tests of surface classification results. The ancillary data applied for this study are summarized in Table 3.2.

Table 3.1. Major data sources.

DATA TYPE	Acquisition time(GMT),date	Sun elevation angle (degree)	Sun azimuth angle (degree)
Landsat 7 ETM+	15:21, Sept 8, 2002	49.839	143.891
ASTER 05 LSE, 08 LST, 07 Reflectance, 09 Radiance	15:52, Sept 8, 2002	52.258	154.148
MODIS 11 L2 LSE, L3 LST, 09 Reflectance	15:52, Sept 8, 2002		

Table 3.2. Ancillary data.

DATA TYPE	ACQUISITION DATE
QuickBird satellite image: 0.7 m panchromatic band and 2.8 m multispectral bands	August 02, 2002
IKONOS satellite image :1 m panchromatic band and 4 m of visible and near infrared bands	July 03, 2001
GER airborne image: 10 m pixel resolution of 52 bands	May 21, 1994
Aerial ortho-imagery: 30.5 cm ground pixel resolution	February-April, 2002
1 m pixel resolution	April-May, 1994-1999
Spectral Library Data	
GIS Vector Data	2000

4. Methodology

4.1. Data Processing Tools

The image processing, plotting, and statistical analyses were accomplished with the software programs Environment for Visualizing Images (ENVI) and Interactive Data Language (IDL), the Environmental Systems Research Institute (ESRI) ArcView, ArcGIS, Microsoft Excel, and Table Curve 2D. The ENVI and IDL software programs were used for opening downloaded satellite image data in HDF format, preprocessing, image mosaicking, transformation, classifications, spectral profile and spectral library data analysis, construction of regions of interests, scatter plot diagram analysis, histogram analysis and other statistical analyses and image mapping. ArcView and ArcGIS software programs were used for retrieving GIS vector information and overlaying multi-layers, opening and quick overview of Mr.SID file. The Microsoft Excel program was used for data conversion and the generation of graphs from satellite data as well as ancillary data sets. The Table Curve 2D program was used for regression analysis.

4.2. Image Fusion Techniques

4.2.1. Background

Image fusion combines information provided from several sensors, or by the same sensor in different spatial, spectral and temporal scenes (Lillo-Saavedra and Gonzalo, 2007). It aims at the integration of disparate and complementary data to enhance the information apparent in the images as well as to increase reliability of the interpretation (Pohl and Van Genderen, 1998). In the following a review will be given on image

sharpening that applied image fusion of digital imagery for increasing the spatial resolution.

Considerable efforts have been made to improve low or moderate spatial resolution satellite observation data to extract spatial details by fusion techniques. The main aim of the fusion technique is to extract high quality information about the imaged object via improved image interpretation and/or automatic image classification. All data fusion techniques and algorithms require a very high precision of geometric coregistration of the images to fuse (Mroz 2000).

The direct fusion technique is classified into two groups, depending on whether it uses all panchromatic band spatial information that include also spectral information components related to the lower resolution multispectral image, or selected panchromatic band spatial information that include only the additional high resolution spatial information. Another fusion procedure is using the panchromatic band information indirectly. This approach was focused on overcoming the unsuitable spectral domain between the panchromatic and mutispectral band and incompatibility of the near infrared or short wave infrared multispectral bands (Hill *et al.* 1999).

The category of fusion using all panchromatic band spatial information includes simple band arithmetic procedures such as addition and multiplication and component substitution techniques. The Intensity, Hue, and Saturation (IHS) or Hue, Saturation, and Value (HSV) transformation, Principal Component Substitution (PCS), and Color Normalization transformation, also known as Brovey transformation, belong to this category.

The IHS transformation technique separates a Red, Green, and Blue (RGB) color composite image to spatial I and spectral HS information by replacing the intensity component of a lower resolution color composite image with a coregistered higher resolution image, and resampling the hue and saturation bands to the high resolution pixel size. Then the image is transformed back to RGB color space (Liu 2000). Intensity (I) or Value (V) refers to the total brightness of the color, Hue (H) to the dominant or average wavelength of the light contributing to the color and Saturation (S) to the purity of color (Vani and Sanjeevi 2001). HIS provides an identifiable visual presentation of the data, but quantitative interpretation with this product is not possible because the statistical properties have been manipulated and the original integrity of the data is disturbed (Pohl and Van Genderen, 1998).

The Color Normalized (CN) sharpening method uses a mathematical combination of the digital data in different spectral bands and high resolution data to sharpen the final image display. Each spectral band is multiplied by a ratio of the high resolution data divided by the sum of the spectral bands. The function automatically resamples the three color bands to the high-resolution pixel size using a nearest neighbor, bilinear, or cubic convolution technique. The resulting output RGB images have the same pixel size as the input high resolution data. Evaluation of the Landsat 7 ETM+ panchromatic band for image fusion with multispectral bands includes the following formulae to carry out the color normalization transformation (Liu 2000):

$R_b = R \times P/I$

$G_b = G \times P/I$

$B_b = B \times P/I$

$$I = (R + G + B)/3$$

where R, G, and B are the spectral band image values displayed in red, green and blue. P is a higher spatial resolution image value for intensity modulation. I is the intensity calculated by the average of R, G, and B. The resulting image is not quite as sharp as the one produced from multiplication only while introducing the texture from higher resolution of panchromatic band (Pohl and Van Genderen, 1998).

The PCS method, which is one of the Principal Component Analysis (PCA) technique, is similar to the IHS method and uses the Principal Components (PCs) as input to the lower resolution multispectral bands. The PC band 1 is replaced with the high resolution band, which is scaled to match the PC band 1 to prevent distortion of the spectral information. Then, an inverse transform is performed. The multispectral data are automatically resampled to the high resolution pixel size using a nearest neighbor (Chavez *et al*., 1991). Pohl and Van Genderen (1998) states that the PCA approach is sensitive to the choice of area to be analyzed.

A comparison between the outputs of the PCS fusion with the IHS and Brovey transformation indicates that the PCS method is superior to the Color Normalization and IHS technique (Vani and Sanjeevi 2001).

To overcome the limitation of the above direct fusion techniques, various filtering techniques have been developed and often used together. Convolution filtering works in a spatial domain and produces an output image in which the brightness value of a given pixel is a function of some weighted average of the brightness of the surrounding pixels. Texture filtering is used to extract information about the textures in the image, and works for the spatial variation of image tone as a function of scale. To be defined as a distinct

textural area, the reflectance within the area must be more homogeneous as a unit than areas having a different texture and detail while suppressing noise (ENVI 2005).

Adaptive filtering uses the standard deviation of those pixels within a local box surrounding each pixel to calculate a new pixel value. Typically, the original pixel value is replaced with a new calculated value based on the surrounding valid pixels that satisfy the standard deviation criteria. Unlike a typical low-pass smoothing filter, the adaptive filters preserve image sharpness and at the same time reduce speckles locally.

Fourier Filtering is an image enhancing technique focused on the frequency domain in the image. Fourier filtering is a mathematical means of separating an image into its various spatial frequency domain. For example, a low-pass-filtered version of the panchromatic band is created by extracting high resolution spatial information. Subsequently, the high frequency addition method extracts the high resolution spatial information using a subtraction procedure and adds them to the multispectral bands via addition (Hill *et al.* 1999). The alternative high frequency modulation method (HFM) extracts the high frequencies via division and adds them to each multispectral band via multiplication (Hill *et al.* 1999). Following Hill *et al.* (1999), the filtering technique reduces distortion of the original spectral information of the low resolution multispectral image, but the panchromatic high resolution spatial information is not necessary suitable for the specific spectral domain in which they are introduced. The edges or boundaries of the near infrared or shortwave infrared bands often exhibit a contrast compared to that of the panchromatic band.

To adjust the panchromatic band information to the uncorrelated longer wavelength bands, the Local Correlation Modeling (LCM) was introduced by Tom *et al*.

(1984). The concept of LCM assumes that there is a local correlation between different spectral bands even if no significant correlation exists between the overview of panchromatic image and multispectral image. This is based on the fact that edges in an image are manifestations of object or material boundaries that vary only in strength. Once a local correlation is identified between a multispectral band and the low pass panchromatic band, it is applied to the higher resolution level. Consequently, the calculated local regression coefficients and residuals are applied to the corresponding area of the high resolution panchromatic band.

Most fusion techniques developed so far merge high spatial resolution panchromatic bands or Synthetic Aperture Radar (SAR) data with low spatial resolution multispectral visible bands. Using other subsets such as near infrared, shortwave infrared or thermal infrared bands for fusion with high spatial resolution panchromatic band, has not been justified for their radiometric composition. A special case forms the fusion of multispectral bands from a single thermal sensor for resolution enhancement (Moran, 1990).

4.2.2. Assessment

Commonly used fusion methods such as CN, HSV, PCS, and GS spectral transform were tested in order to identify an optimal technique for enhancing spatial details of thermal infrared bands by panchromatic band information. The concept of image fusion is demonstrated in Figure 4.2.2. It shows the two original images before merged in the left side of Figure 4.2.2, a 15 m pixel resolution panchromatic band image in the upper left and a 30 m resolution multispectral bands color composite image based on the thermal band, the near infrared, and the visible band as RGB in the lower left. The

merged image shows a product of HSV in the upper right and a CN product in the lower right.

For the HSV technique, first, a brightness intensity band of a RGB color composite image was replaced with a coregistered high resolution panchromatic image, and the hue and saturation bands were resampled to the high resolution pixel size using the nearest neighbor technique. The image transformed finally back to RGB color space, and the output color image was displayed at the 15 m pixel size. The example in the upper right part of Figure 4.2.2 shows the input color composite that was prepared from the thermal, near infrared, and green bands and are presented as hue, saturation, and value or intensity. The brightness of the value band was replaced with the panchromatic data and the thermal and near infrared band data were resampled by a nearest neighbor method. The output RGB image product was transformed into a 255 color scale.

For the CN transform, each band in the color image was multiplied by a ratio of the high resolution data divided by the sum of the color bands. The function resampled the three color bands to the high-resolution pixel size using a nearest neighbor technique. The result of a multiplication with the ratio of the panchromatic band value to the average of three low resolution band values in the normalization process reduced some extreme distortion associated with the dominant panchromatic value. The product from the CN technique showed similar patterns in the three bands' histogram distribution, however, this technique also presented some level of distortion in each output band generated from normalization.

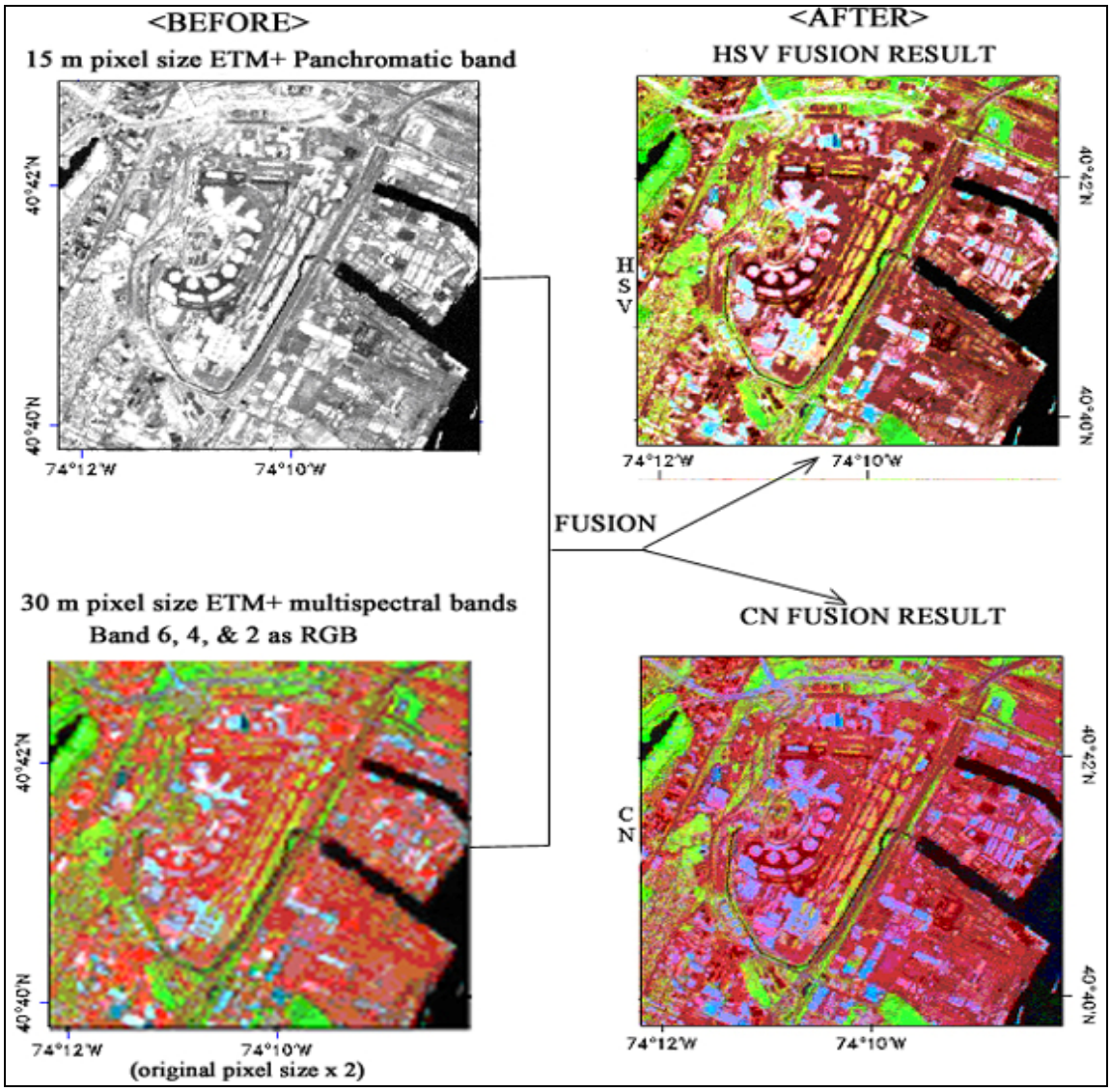

Figure 4. 2 .2. The conceptual diagram for image fusion applied over Newark Airport in New Jersey with Landsat 7 ETM+ data. Upper left (original) image displayed as gray scale with a 15 m pixel size ETM+ panchromatic band. Lower left image shows the same area coverage as the upper left panchromatic image, but has a 30 m pixel size, which was enlarged by twice and is displayed as a color composite with the thermal band (10.40-12.50 μm), near infrared band (0.75-0.90 μm), and green band (0.525-0.605 μm). Upper right image is the result of the HSV transformation with a pixel size of 15 m. Lower right image is the result of the CN transformation with a 15 m pixel resolution.

4.2.3. Evaluation Result

To find a best fit fusion method for classification, including previously mentioned spectral sharpening CN, HSV, PCS and the GS sharpening which is recently available by the ENVI function were tested. Among the fusion methods tested, CN, HSV, PCS and GS spectral sharpening, PCS and GS showed improvement in image visualization by enhancing spatial resolution. The PCS and GS method appeared to be superior to CN or HSV by processing the transform based on the simulated panchromatic band and the spectral bands. Both the PCS and GS sharpening showed very similar levels of visual enhancement, and marginal distortion of the original data values were observed as shown in Figure 4.2.3.1 (eg. the vicinity of the Newark Airport).

(A) PRINCIPAL COMPONENT (B) GRAM-SCHMIDT

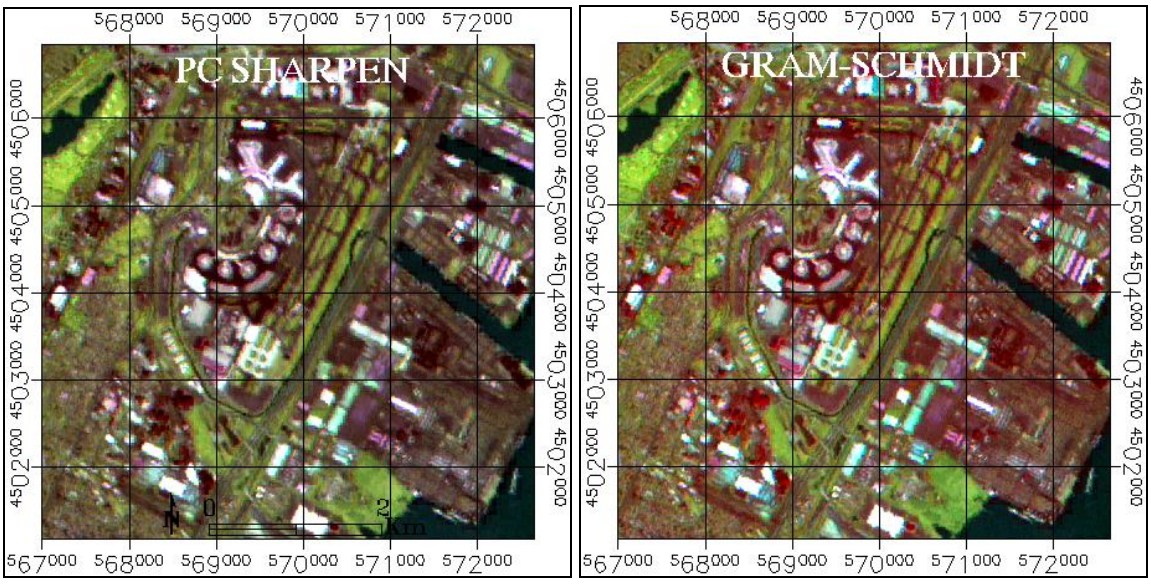

Figure 4.2.3.1. Image fusion product of PCS (A) and GS (B) as a color composite of bands 6, 5, and 2 as RGB: the area over Newark Airport in New Jersey in September 8, 2002.

Further correlation and covariance tests based on comparison of the ETM+ original data with the product of the PCS sharpening and the GS sharpening by 2-dimensional scatter plot analysis show not significant difference between two transformed products (Table 4.2.3.1). A little higher correlation was noticed from the GS sharpened image, but the covariance appears a little higher in the PCS result. A comparison with the original radiance distribution of multispectral bands of the ETM+, the distribution pattern showed more closeness to the original data by the PCS fusion than by the GS fusion.

Table 4.2.3.1. Correlation and Covariance of the PCS and GS results over Newark Airport region.

COVARIANCE		ETM+ Band					
		1	2	3	4	5	7
PC Band	1	0.0013					
	2		0.0019				
	3			0.0027			
	4				0.0066		
	5					0.0048	
	6						0.0024
GS Band	1	0.0012					
	2		0.0018				
	3			0.0025			
	4				0.0064		
	5					0.0045	
	6						0.0022
CORRELATION		ETM+ Band					
		1	2	3	4	5	7
PC Band	1	0.7911					
	2		0.8001				
	3			0.7945			
	4				0.8309		
	5					0.7814	
	6						0.7381
GS Band	1	0.8077					
	2		0.8166				
	3			0.8133			
	4				0.8434		
	5					0.7919	
	6						0.7518

Among the various filtering techniques applied with the above transform tools, the local sigma filter, that is one of the adaptive filters, showed an image improvement by reduction of speckle. An advantage of using the local sigma filter is that it preserves fine details even in low contrast areas by using the local standard deviation computed for the local filter box. However, the replacement from these local filter computations adds an additional distortion of the original data information. Therefore, the PCS fusion tool without further application of filtering was chosen for further image classification.

A high spatial resolution remote sensing data QuickBird image was added to the collection of ground survey information. As the QuickBird panchromatic band has a 0.7 m spatial resolution, the image displayed in Figure 4.2.3.2.A shows a good separation among small objects that have unique shapes. In addition, some of features possessing distinguishable reflectance levels such as high-albedo or low-albedo objects reveal in a separated manner. However, the panchromatic image has a limited capability to discern surface types by tonal variations or texture differences.

The false color image generated with 2.8 m pixel resolution of the QuickBird multispectral bands in the near infrared, red, and green band as RGB (Figure 4.2.3.2.B) demonstrates relatively easy site identification based on color difference as well as texture differences. For instance, it shows distinct color differences between dry grass lawns and cement concrete or asphalt concrete paved area, which appeared to be very similar in the panchromatic image. However, there are mixed pixels with unclear boundaries between neighbor objects due to the lower pixel size of this color composite.

A. The QuickBird panchromatic band image

B. The QuickBird multispectral band image

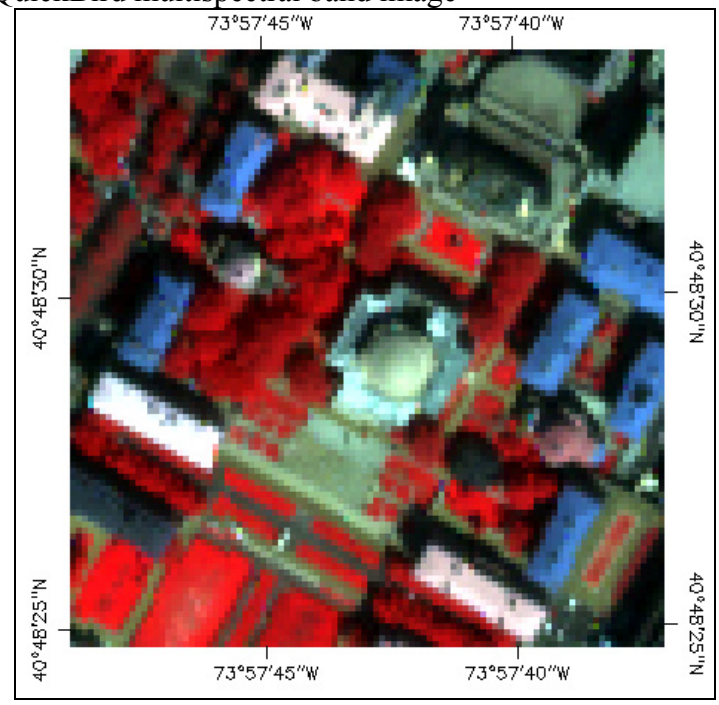

Figure 4.2.3.2. The QuickBird panchromatic band image in a 0.7 m spatial resolution (A) and multispectral band image in a 2.8 m spatial resolution with a false color composite (B) acquired in August 2, 2002.

The higher resolution panchromatic band image and the multispectral color composite image were fused by the PCS and showed a significant improvement in tones and objects (Figure 4.2.3.3).

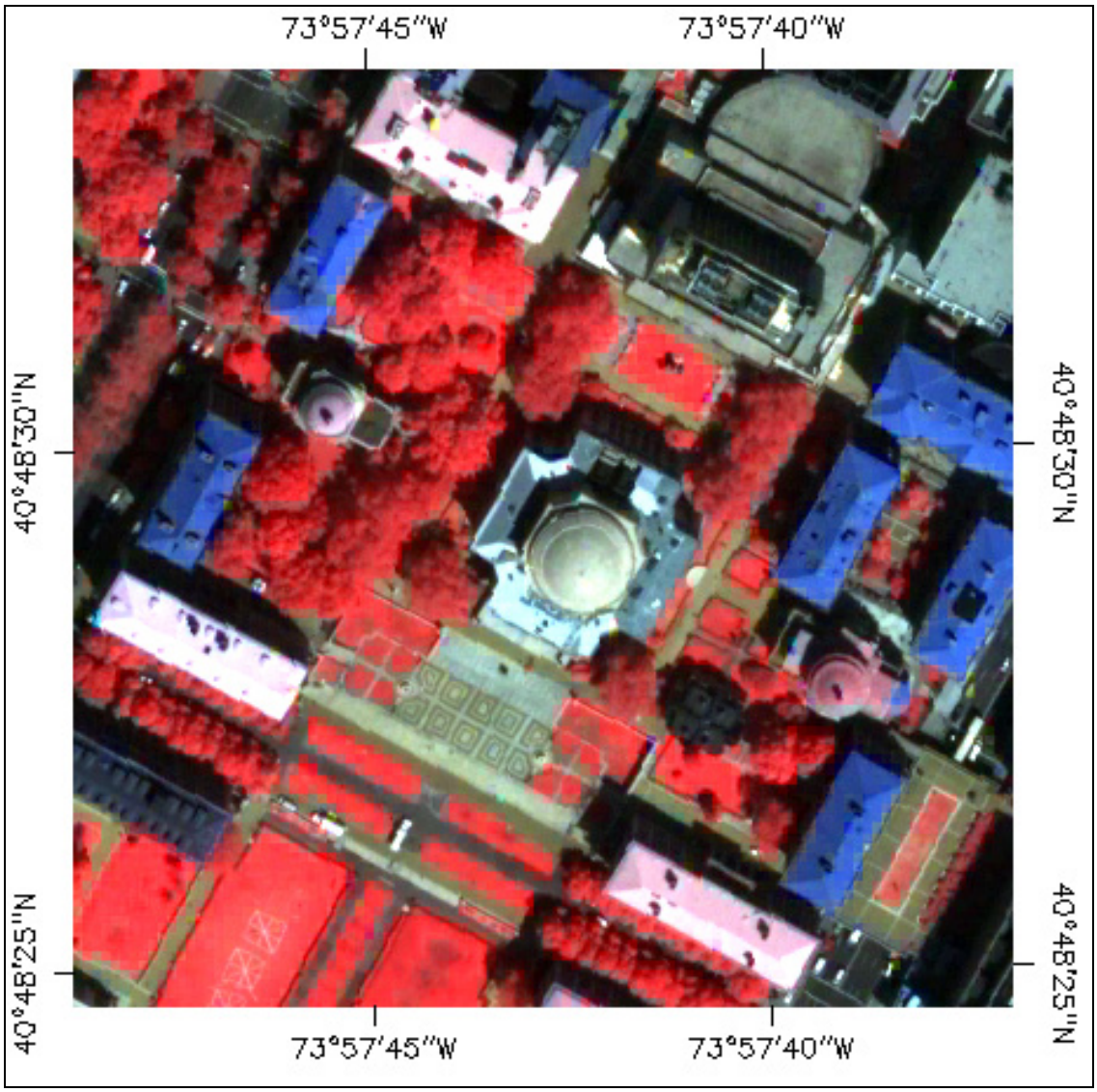

Figure 4.2.3.3. The QuickBird fusion image by merging the 0.7 m spatial resolution panchromatic band with 2.8 m spatial resolution multispectral bands (4, 3, and 2 as RGB).

The evaluation of results on the image fusion methodology can be summarized in the following:

1) Urban surface classification using image fusion by either Principal Component or Gram-Schmidt transformation delivers, compared to Color Normalization and Hue Saturation Value, a superior image fusion product with a minimum distortion of the original spectral properties. The Principal Component Substitute product shows a little higher covariance than the Gram-Schmidt product.

2) For identifying surface cover types with high resolution data from QuickBird or IKONOS, both Principal Component Substitute and Gram-Schmidt fusions are superior to any other fusion products.

4.3. Selection of Training Sites

In the selection of representative training sites for urban surface classification, the QuickBird image acquired on August 2, 2002 was used. This image was pre-processed to generate the top-of-atmosphere (TOA) band-integrated spectral radiance followed by the conversion steps attached in Appendix 4.3. The selection of ground points was based on a surface of about 90 m by 60 m with homogeneous cover types that were represented by 30 pixels by 15 pixels in the QuickBird multispectral radiance image.

Using radiance data over Manhattan and part of Queens in the New York City, density slicing and color coding for each level were applied to the map with differentiated radiance levels in order to select the ground survey sites. The radiance distribution of the QuickBrid panchromatic image is shown in Figure 4.3.1. The ground survey areas dimension were approximately 7 km by 9.6 km.

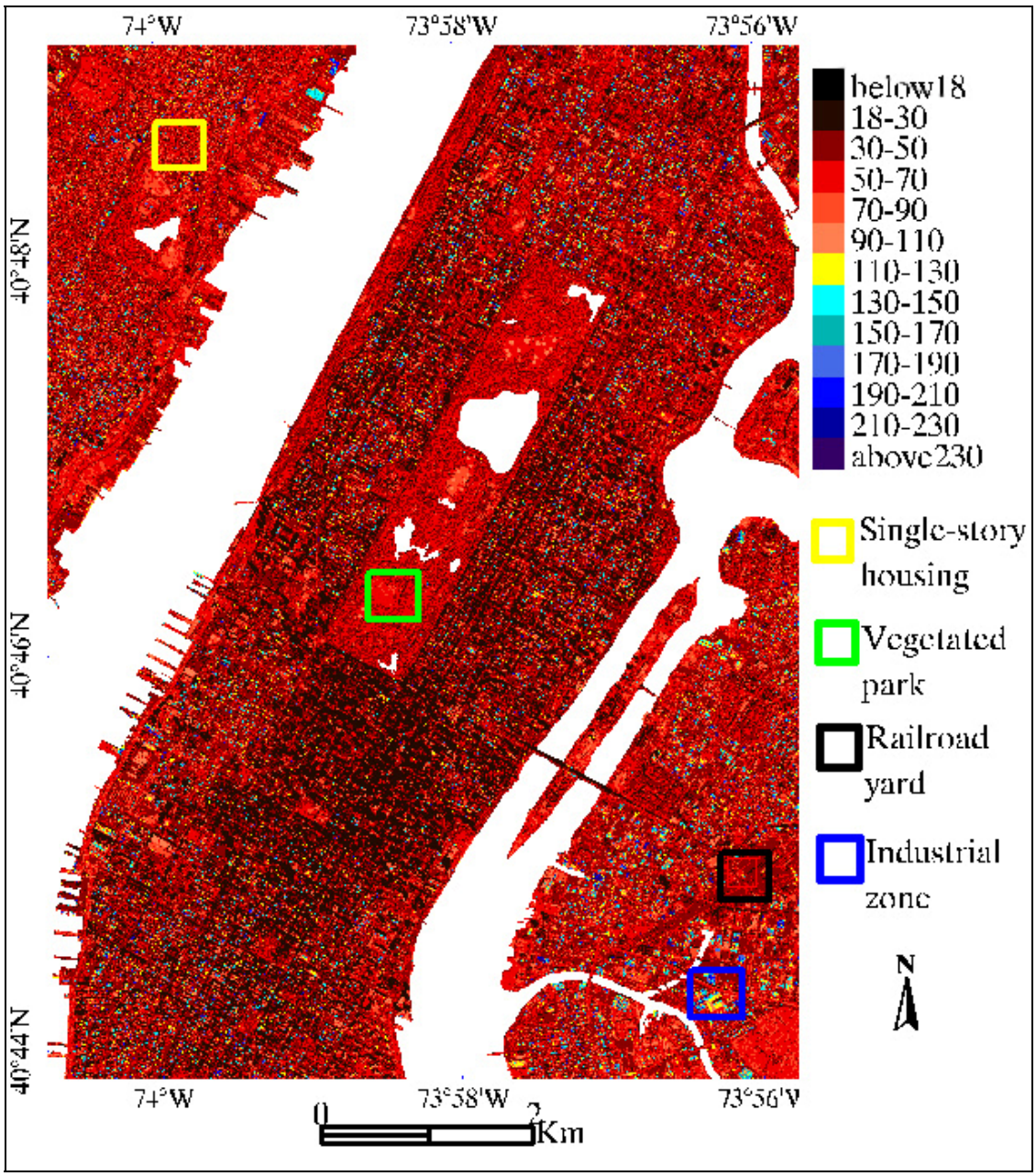

Figure 4.3.1: Radiance distribution (W m^{-2} sr^{-1} μm^{-1}) generated from the QuickBird image acquired in 2 August 2002,. Water bodies were masked in white.

Tree standing vegetation areas have a high frequency of radiance at 54 W m^{-2} sr^{-1} μm^{-1} and grasslands are between 66 and 67 W m^{-2} sr^{-1} μm^{-1} (see the green box area in Figure 4.3.1 and Appendix Figure 4.3.1.A), whereas dry bare soils can be recognized between 70 and 80 W m^{-2} sr^{-1} μm^{-1}. Railroad yards appeared at a relatively low radiance level from 35 to 40 W m^{-2} sr^{-1} μm^{-1} (see the black box area in Figure 4.3.1 and Appendix Figure 4.3.1.B). Water bodies had radiance levels below 30 W m^{-2} sr^{-1} μm^{-1} and were masked as white. Among the regions covered with manmade materials, single housing areas have mostly asphalt or concrete shingles, and wood shingles appeared at radiance around 64 W m^{-2} sr^{-1} μm^{-1} (see the yellow box area in Figure 4.3.1. and Appendix Figure 4.3.1.C). Paved roads and highways have a radiance range 40 to 70 W m^{-2} sr^{-1} μm^{-1} and their radiance levels seem to relate to the age of pavements.

Most industrial zones and multi-housing areas showed significant bimodal types of radiance patterns i.e., radiance values were either below 40 or above hundreds W m^{-2} sr^{-1} μm^{-1} (see the blue box area in Figure 4.3.1. and Appendix Figure 4.3.1.D).

Radiance distribution of the QuickBird image over land surfaces in Table 4.3.1, shows the highest frequency between 30 and 50 W m^{-2} sr^{-1} μm^{-1} while the second major range is between 50 and 70 W m^{-2} sr^{-1} μm^{-1}. The third highest frequency marked as the radiance range between 18 and 30 W m^{-2} sr^{-1} μm^{-1} is dominated by shadowed streets between high rise buildings in mid Manhattan.

Table 4.3.1. Radiance distribution from the QuickBird image over the land surface area of Manhattan and part of Queens county in the New York City.

Radiance Range (W m^{-2} μm^{-1} sr^{-1})	**Percentage (%) of Land Surface Cover**
below 18	less than 1
18-30	19
30-50	39
50-70	27
70-90	8
90-110	3
110-130	1
130-150	1
150-170	1
170-190	1
above 190	less than 1

Based on the radiance analysis of the QuickBird image, a selection of ground truth survey site was established. The selected areas were matched with an area of 6 pixels by 4 pixels in the ASTER image, and 1 or 2 pixels by 1 pixel in the Landsat 7 ETM+ thermal image. Figure 4.3.2 shows the subsets of representative training sites that were collected from the 0.7 m pixel size panchromatic QuickBird image and were generated by image fusion followed by density slicing of the radiance image and are shown in the left column. The corresponding color photo taken during the ground survey or from the QuickBird natural color composite image are presented in the right column.

Density Sliced QuickBird Radiance Image	Handheld Camera Photo	Density Sliced QuickBird Radiance Image	Handheld Camera Photo
1. White emulsion coated sheet		2. Zinc synthetic layer (gray)	
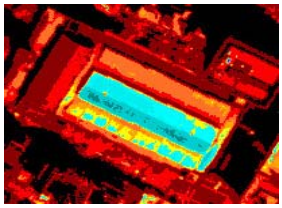		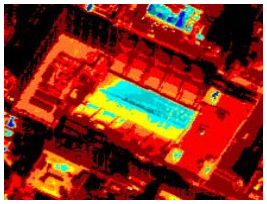	
3. Aluminum /Glass		4. Ivory & red color painting on metal	
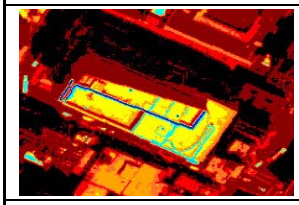		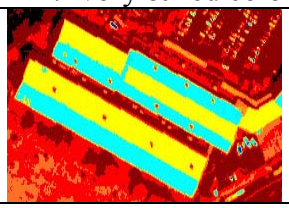	
5. White synthetic membrane(blue)		6. Ivory color polysynthetic membrane	
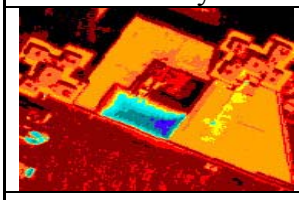		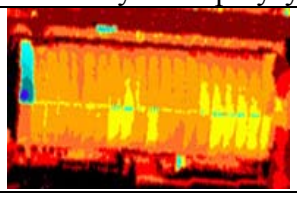	
7. Zn illuminate sheet		8. Light brown stones chips	
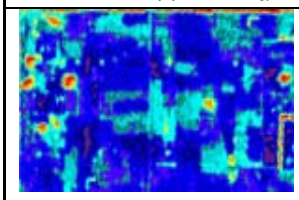		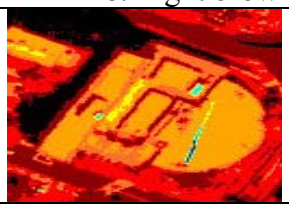	
9. Bright granulated cement concrete		10. Tint colored concrete	
		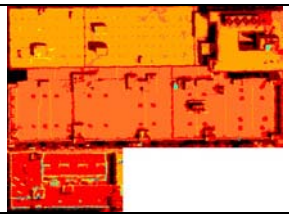	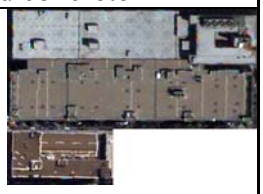
11. Light-tone cement concrete		12. Gravels (mixed various colors)	
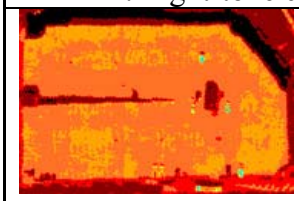			

Figure 4.3.2. The radiance image obtained by QuickBird and handheld camera photos of selected ground survey sites.

Density Sliced QuickBird Radiance Image	Handheld Camera Photo	Density Sliced QuickBird Radiance Image	Handheld Camera Photo
13. Black synthetic sheet		14. Tar coat-rough surface	
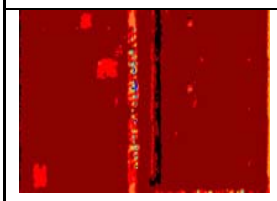	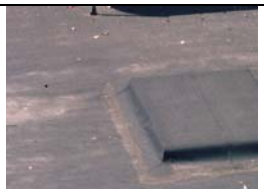	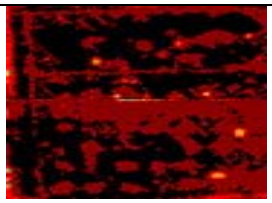	
15. Highway1:Concrete paved		16. Highway2:Asphalt tar paved	
		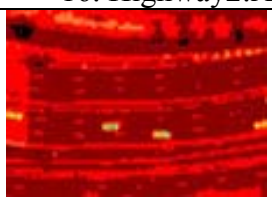	
17. Street 1–gray concrete Tiles		18. Street 2-bright red concrete Tiles	
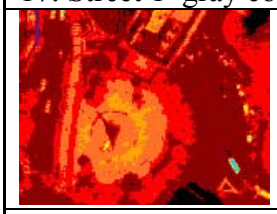			
19. Tint colored concrete, glass, metal		20. Single houses (shingle roofs)	
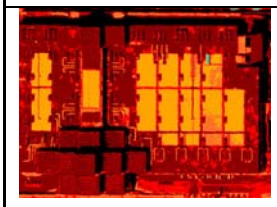		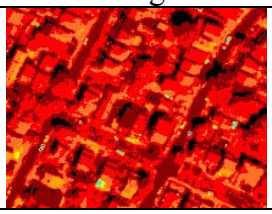	
21. Warehouses (Industrial zone)		22. Mid-height multiple housing	
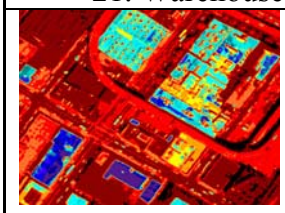		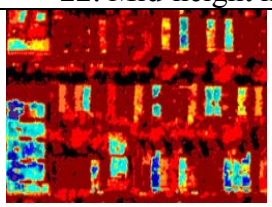	
23. High-rise Apartment rooftop		24. Shadows and high-rise building	
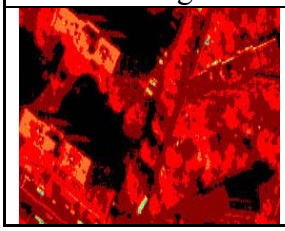			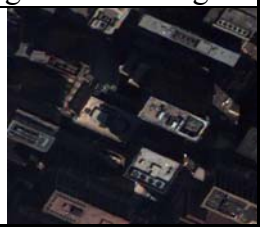

Figure 4.3.2. Continued.

Spectral profiles of the selected ground observation sites were extracted from the multispectral ASTER radiance data. The collection of spectral profiles (Figure 4.3.3.A and B) were carried out in two separated wavelength regions, between 0.52 μm and 0.86 μm and between 2.145 μm and 2.430 μm respectively.

A.

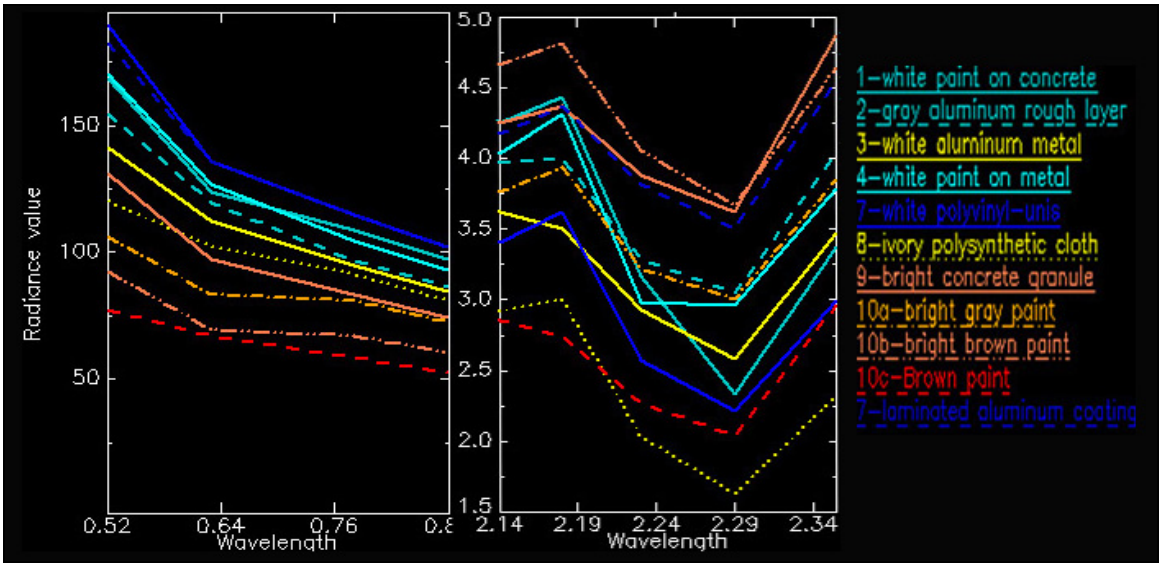

B.

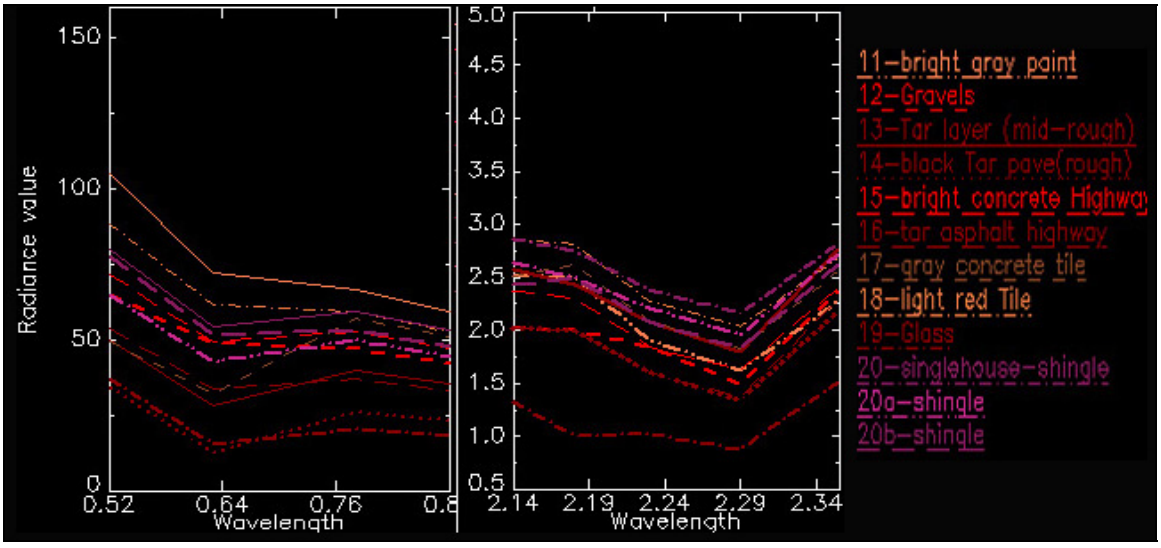

Figure 4.3.3. The spectral profiles of high reflection sites (A), and the spectral profiles of low reflection sites (B).

The bright or tint tone areas in the radiance image which refer to number 1, 2, 3, 4, 7, 8, 9, and 10 showed high reflection (Figure 4.3.3.A), and dark tone or black areas appeared as relatively low reflection and emission as shown in Figure 4.3.3 B. Geographic referencing for each ground surface cover type, roughness and longitudinal and latitudinal location were recorded with a handheld Global Positioning System (GPS) and are shown in Appendix Table 4.3.2.

4.4. Assessment of Classification Methods for Urban Surfaces

To find an optimal classification method for urban surfaces, supervised classifiers Maximum Likelihood (ML), Spectral Angle Mapper (SAM), Neural Network (NN), and Decision Tree (DT) classifier were tested with various numbers of training sites (Appendix 4). For a screening test, the eleven training sites and the seven input bands included four bands converting the visible to near infrared (0.45-0.90 μm), two bands located in the mid-infrared (1.55-2.35 μm) and one thermal infrared (10.40-12.5 μm). They were used for the classification of data with ML, SAM, and NN. For the DT classification, five band ratios namely the ratio of 0.57 μm/0.66 μm, 0.83 μm/0.66 μm, 1.65 μm/0.83 μm, 1.65 μm/2.22 μm, 2.22 μm/0.48 μm, and a mean value between 0.48 μm and 0.83 μm were used in addition to seven ETM+ bands.

The basic statistics representing from this preliminary classification tests with eleven training sites are summarized in Appendix Table 4.4 and the classified maps resulting from different classifiers are documented in Appendix Figure 4.4.1. The classified results were tested by confusion matrix calculations using the ground reference as regions of interest. The overall accuracy and Kappa coefficient for each classification

were computed and are shown in Table 4.4.1. The overall accuracy was computed by dividing the sum of correct pixels classified in each class by the total number of pixels in the error matrix, i.e., it represents a measure of how many ground truth pixels in the reference data set were classified correctly. The overall accuracy only incorporated the major diagonal and excluded the omission and commission errors.

Table 4.4.1. Overall accuracy and Kappa coefficient of classification results: ML = Maximum Likelihood, SAM=spectral Angle Mapper, DT=Decision Tree, and NN=Neural Net Classification.

CLASSIFIER	ML	SAM	DT	NN
Overall Accuracy	96.90%	88.46%	88.26%	39.24%
Kappa Coefficient	0.96	0.86	0.86	0.35

Unlike the overall accuracy, the Kappa analysis incorporated the off-diagonal elements as a product of the row and column marginal. The Kappa analysis demonstrates whether the results presented in a supervised classification map are significantly better than a random result and compares two similar classification to determine if they are significantly different (Congalton 1991; Jensen 1996). The advantage of Kappa analysis is that all elements in the classification error matrix contribute to its calculation and because it compensates for change agreement (Rosenfield and Fitzpatrick-Lins 1986). The Kappa coefficient represents the proportion of agreement obtained after removing the proportion of agreement that could be expected to occur by chance (Foody 1992).

The Kappa value of 0.96 in Table 4.4.1 have a probable 96% better accuracy than the classification resulted from random, unsupervised, assignment instead of the employed ML classification. Following the category of Congalton (1991), Kappa values can be grouped in three categories, those that have values:

1. greater than 0.8 representing strong agreement,

2. values between 0.4 and 0.8 that represent moderate agreement, and

3. values below 0.4 that represent poor agreement.

The results from ML, SAM, and DT classification showed strong agreement whereas the results of NN classification represented very poor agreement. Among the three classification results, the highest accuracy was found in the ML classification. Therefore, the further detailed classification over the study area, the ML classification was selected.

To find a best fit classification result, different numbers of input bands from ETM+ data were used for the ML classification with 20 training sites, and their overall accuracy and Kappa coefficient were examined. With increasing training sites, more input sources are required to improve the accuracy of ML classification result. Since ETM+ data provide six reflectance bands and one thermal band, four additional different input sources were generated through ratios, principal component bands and averaged ratios. The selection of these additional input bands was based on a correlation analysis between the six ETM+ bands. The bands with high correlations were excluded in generation of band ratios.

The band ratio 0.66 μm/0.57 μm assisted to separate iron based roofing covers from adjacent trees, and beach soils from brown organic soils whereas the ratios 0.83

μm/1.65 μm and 0.83 μm/2.22 μm showed good discrimination between white pigment coated metal roofs from white paint concrete roofs. The ratio 1.65 μm/2.22 μm emphasized soil covers and the ratio 1.65 μm/0.66 μm or 1.65 μm/2.22 μm was useful to identify spectrally cement or concrete covers. Also the ratio 0.66 μm/0.48 μm is a parameter to identify concrete rooftops that were coated with white pigments. Additional input bands were the ratios 0.57 μm/0.48 μm, 0.83 μm/0.66 μm, 1.65 μm/0.66 μm, 1.65 μm/0.83 μm, 2.22 μm/0.48 μm, 2.22 μm/0.66 μm, the average of 0.83 μm and 2.22 μm, and the sum of 0.48 μm, 0.57 μm and 0.66 μm. These additional input bands were applied for ML classifications, and results were examined against the overall accuracy and Kappa coefficients from confusion matrix analyses.

The results from five sets of different input sources in the classification of the ML classifier for the twenty training sites are presented in Table 4.4.2. The accuracy of the ML classification with a total of nineteen input bands that consisted of twelve ratios and seven original ETM+ bands shows an increase of 0.84% in the overall accuracy and 0.04 in Kappa coefficient. The classification with twenty two input bands that were generated for two different combinations show different results: adding three bands which were based on three sets of the mean values resulted in slight improvement in the Kappa coefficient by 0.004, but decreasing in the overall accuracy by 0.7%. Using nineteen input sources as before but adding three principal component bands shows improvement in both accuracies (Table 4.4.2). It indicates that including principal component bands improve the overall accuracy. The classification with twenty-five input bands showed decline in both overall accuracy and the Kappa coefficient. It suggests that using those

input bands generated by mean of two or three visible or near infrared bands may have a negative effect on the classification process.

Table 4.4.2. ML classification of ETM+ image results with five different input sources for 20 training sites.

	7 Input*1	**19 Input *2**	**22 Input *3a**	**22 Input*3b**	**25 Input*4**
Overall Accuracy	95.95%	96.79%	96.09%	96.90%	96.48%
Kappa Coefficient	0.774	0.813	0.817	0.818	0.796

*1: original 6 reflectance bands and 1 thermal radiance band of ETM+.
*2.19 input bands: 7 original ETM+ bands plus 12 ratios (band ratios 2/1, 3/1, 3/2, 4/2, 4/3, NDVI, 4/5, 5/1, 5/3, 5/7, 7/1, and 7/3).
*3a. 22 input bands: 19 bands (*2) plus 3 additional averages (the mean of band 2, 3 & 4, the mean of band 4, 5, & 7, and the mean of band 4 & 5).
*3b. 22 input bands: 19 inputs (*2) plus 3 principal component bands 1, 2, and 3.
*4. 25 inputs: 7 original bands, 12 ratios, 3 averages, and 3 pc bands.

An additional accuracy test was carried out in applying the developed classification method for vegetation coverage. The estimation of vegetation coverage used for a comparison is the scaled difference vegetation index method, which was developed to resolve difficulties and uncertainties in vegetation fraction estimation by the NDVI measurement (Jiang *et al*. (2006). A 2.8 m pixel resolution of QuickBird multispectral image (size: 7 km x 9.7 km, acquired on August 2, 2002) was used as ground reference. This high resolution reference image covers about 3.8% of the total study area (42 km x

42 km). The vegetation coverage estimated by the SDVI in the reference image was 10.6% shown in the summary Table 4.4.3.

Table 4.4.3. Summary of SDVI analysis.

SDVI	Percent (%) per Reference Area (7 km x 9.7 km)			Percent (%) per Total Study Area (42 km x 42 km)	
	QuickBird	ETM+	ASTER	ETM+	ASTER
Vegetation Coverage	10.6	10.6	10.2	24.5	24.3

To match with this estimation in the same area of the 15 m pixel resolution of ETM+ and ASTER images, the SDVI analyses optimized for each image condition was processed. The results showed vegetation coverage of 10.6% for ETM+ and 10.2% for ASTER, respectively. The same procedure was further applied to the whole study area for the ETM+ and ASTER images. The vegetation coverage in the total study area was estimated to be 24.5% in the ETM+ image, and 24.3% in the ASTER image.

Based on the vegetation coverage estimated by the SDVI analysis, further ML classification was extended to twenty surface training sites in the study area. The ML classification result of the 15 m ETM+ image is based on twenty training sites and used twenty two input bands generated by six reflectance bands, one thermal radiance band, twelve ratio bands, and three principal component bands (Appendix Figure 4.4.2) presented 25.1% of vegetation coverage, and the 15 m ASTER image showed 25.3% of vegetation coverage (Table 4.4.4). The estimated total vegetation coverage is the sum of tree, grass, and marsh area.

Table 4.4.4. Summary of vegetation coverage classified by ML classifier over the total study area.

CLASSIFIED VEGETATIONS	% by ETM+	% by ASTER
Tree	20.91	19.94
Grass	3.52	4.47
Marsh	0.69	0.89
Total vegetation coverage	25.12	25.30

In summary, the classification method derived from this study was as follows:

1) Improving the accuracy of urban surface classification with twenty differentiated classes was possible by using twenty two input bands generated by additional band ratios, including thermal band and three principal component bands,

2) Among the tested supervised classifiers, the maximum likelihood classifier is superior to the others with its overall accuracy above 96% and Kappa coefficient 0.96, and

3) As a partial accuracy test focused on only urban vegetation coverage, using Scaled Difference Vegetation Index showed efficient way to assess classification result.

4.5. Estimation of Urban Surface Emissivity from ASTER and ETM+

In order to retrieve absolute surface leaving temperature from remotely sensed radiance measurement, it is necessary to know the emissivity of a target. Surface emissivities published from the MODIS Emissivity Library of Institute for Computational Earth Science System (ICESS), Lawrence Berkeley National Laboratory (LBNL) and some private industries are based on the measurements of laboratory conditions at a

specific temperature and at the wavelength ranging from 8 μm to 14 μm (Appendix Table 4.5.1).

Since surface emissivity depends on the composition, roughness, and moisture content of the surface and on the observation conditions i.e., wavelength, observation angle, and pixel resolution (Sobrino *et al*. 2001), direct application of laboratory emissivity measurements to derive remotely sensed surface temperature may lead to errors. Concerning the importance of the knowledge of LSE in the LST retrieval, Sobrino *et al*. (2005) states that an uncertainty on the LSE of 0.01 leads to an error on the LST of around 0.5 ºK.

Satellite observations of surface emissivity based on radiance are currently available from ASTER data at 90 m resolution and from MODIS data at 1 km resolution. For this study, the emissivity information over urban land surfaces was estimated from emissivity that was derived from ASTER data.

To define emissivity from ETM+ thermal radiance measurements, the ASTER LSE measurements from 8.13–8.48 μm, 8.48–8.83 μm, 8.93–9.28 μm, 10.25-10.95 μm, and 10.95-11.65 μm were coregistered with ETM+ and scaled to 15 m and 28.5 m pixel resolution. The ASTER emissivity values corresponding to the surface classification map were collected through three different approaches. One was based on mean values from the ASTER emissivity band 13 (10.25-10.95 μm). Another approach was based on the average from the ASTER emissivity band 14 (10.95-11.65 μm). The other was the average of both ASTER emissivity band 13 and 14 values. The results of the three collections for class emissivity values are presented in Table 4.5.

Table 4.5. Satellite measured surface emissivities and percent of each coverage from the ASTER LSE image.

Classified Surfaces	ASTER Emissivity Wavelength Range			Percent (%)
	10.25-10.95 µm	10.95-11.65 µm	Mean 10.25-10.95 & 10.95-11.65 µm	
Black glossy tar pavement	0.935	0.930	0.933	1.12
Gray synthetic membrane roof	0.931	0.925	0.928	0.75
Black granule sheet roof	0.932	0.924	0.928	0.70
Asphalt pavement	0.937	0.930	0.934	24.61
Cement concrete pave	0.941	0.934	0.938	15.38
Tint colored concrete roofs	0.937	0.930	0.934	0.78
White paint roof	0.936	0.929	0.933	0.63
White emulsion metallic coating (white pigment coating)	0.941	0.935	0.938	0.10
Color paint metal	0.938	0.931	0.935	2.45
White synthetic membrane	0.927	0.917	0.922	0.10
Thin zinc coating	0.913	0.900	0.907	0.12
Zinc coat w/exposed metal surfaces	0.910	0.897	0.904	0.07
Gray slate roof	0.922	0.910	0.916	0.34
Shadow	0.947	0.941	0.944	1.10
Soil	0.945	0.940	0.943	2.36
Sand	0.954	0.949	0.952	0.23
Grass	0.947	0.942	0.945	3.52
Tree	0.945	0.940	0.943	20.91
Marsh	0.953	0.948	0.951	0.69
Water	0.967	0.961	0.964	24.04

Only a few studies to retrieve emissivity based on remote sensing data in urban environment have been published. Utilizing ASTER LSE measurements to describe urban biophysical and thermal conditions, Lu and Weng (2006) used band 13 (10.25-10.95 μm) of the ASTER LSE to compute LSTs based on the band characteristic that shows the peak radiation of the black-body spectrum given off by the urban surface. The investigation of urban feature emissivity variability using aerial thermogram images by Artis and Carnahan (1982) revealed that most roofing materials have a mean emissivity of 0.92 and less than 1% of roofing materials show an emissivity below 0.85, which were likely to consist of metal sheeting or low-emissivity slate roofs. The emissivity collections over our study area show that most roofing materials have emissivities between 0.929 (mean of the10.25-10.95 μm band) and 0.921 (mean of the 10.95-11.65 μm band). The emissivities of most pavements are between 0.939 (mean of the10.25-10.95 μm band) and 0.932 (mean of the 10.95-11.65 μm band). The classes with emissivities below 0.915 are zinc or aluminum illuminate coated metal or tin roofs, which might also be associated with exposed surface underneath. One of the emissivity maps generated from ASTER LSE band 14 (10.95–11.65 μm) is shown in Figure 4.5.

To find the appropriate surface emissivities to derive surface temperature from the ETM+ thermal data, ASTER LST and three ETM+ surface temperature maps derived from three different emissivity collections were examined. In the process of generating surface temperature maps from ETM+ thermal data, the atmospheric correction effects considered in chapter 4.6 were applied as well as the emissivities collected at three different sources.

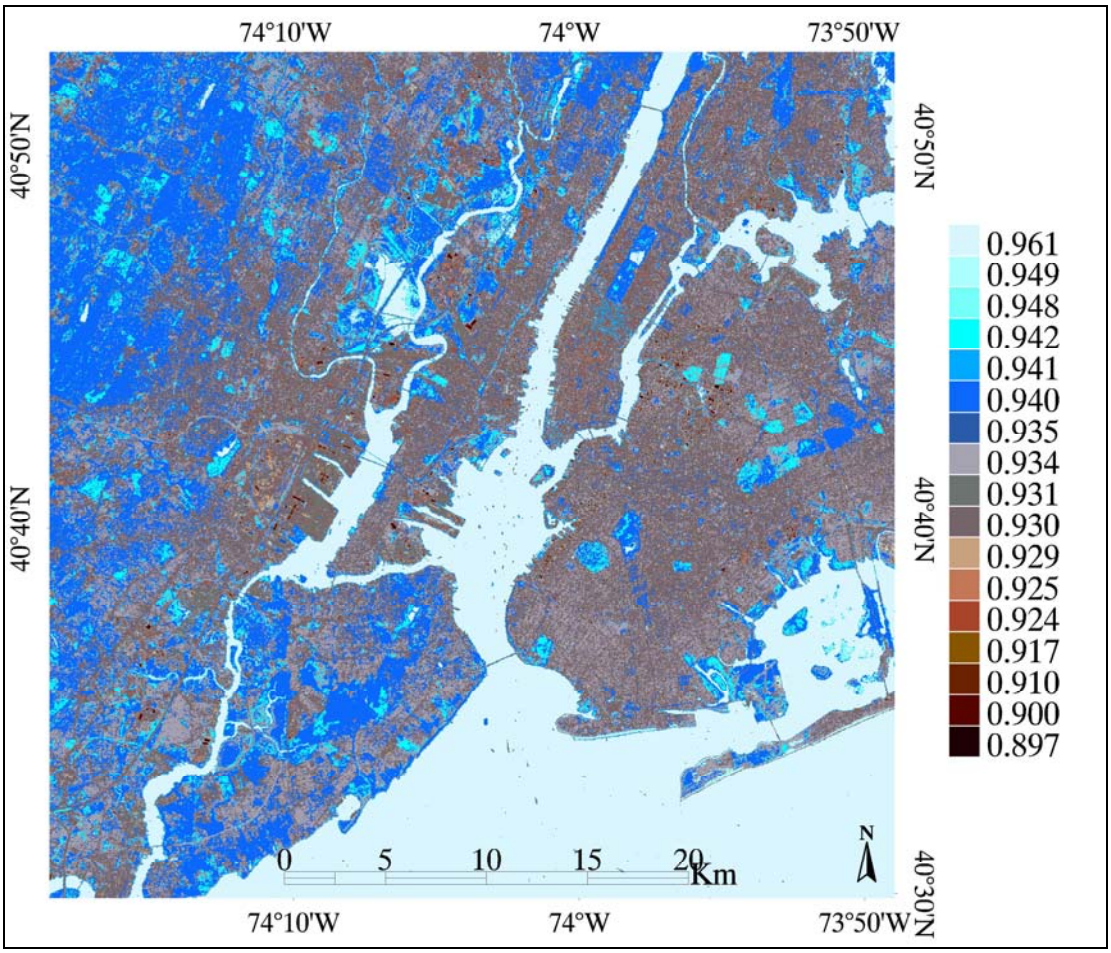

Figure 4.5. A classified emissivity map of the study area: the assigned emissivities are from the mean of band 14 (10.95–11.65 µm) of the ASTER LSE (Landsat ETM+ image acquired in September 8, 2002).

4.6. Application of Atmospheric Corrections for Surface Temperature Retrieval from ETM+

Removing the effects of the atmosphere in the thermal region is an essential step prior to conversion of the thermal band to absolute temperature (Barsi *et al* 2005). Without atmospheric correction, the surface temperatures are usually 5-10 ºK lower than predicted. They are 0-3 ºK higher than the National Centers for Environmental

Prediction (NCEP) temperatures when the data are corrected by using a standard atmosphere (Basri *et al* 2005).

To correct the atmospheric effects, it is necessary to derive the information of the site-specific atmospheric transmission, the upwelling or atmospheric path radiance, and the downwelling or sky radiance on a particular date, time and location as input. The Atmospheric Correction Parameter Calculator (ACPC) can be accessed at the web site that was developed by the National Aeronautics and Space Administration/Goddard Space Flight Center (NASA/GSFC) Land Cover Satellite Project Science Office. However, making proper use of this tool in the ETM+ image analysis requires careful consideration of interpolations and the spatial resolution of the original input data. The original NCEP input source for the atmospheric profile is sampled at 1º x 1º. That corresponds roughly to the size of an ETM+ full scene. When a study area is a subset of the full scene, using one representative atmospheric parameters generated by the ACPC may not be an appropriate approach. Therefore, different numbers of application for the atmospheric corrections were tested. First, the atmospheric parameters representing 18 different sites over the study area were achieved by using the ACPC (Appendix Table 4.6). Based on these atmospheric corrections, five different applications were tested:

(1) a single set of atmospheric correction parameters from the average of 20 collected sites was applied,

(2) two sets- land surfaces and water bodies,

(3) three sets- low albedo surfaces, high albedo surfaces, and water bodies,

(4) four sets-high albedo, low albedo, vegetation/shadow/soils, and water bodies, and

(5) five sets-low albedo surfaces, high albedo surfaces, forest and soil, grass lands, and water bodies. Applied atmospheric correction parameter values for each test case are presented in Table 4.6.

Table 4.6. Atmospheric correction parameters for five different tests.

Test set		Transmission (τ)	Upwelling radiance (L_u)	Downwelling radiance (L_d)
1	Single parameter for the whole study area	0.696	2.36	3.73
2	Land surfaces	0.68	2.45	3.86
	Water bodies	0.70	2.37	3.73
3	High albedo land surfaces	0.68	2.45	3.86
	Low albedo land surfaces	0.68	2.40	3.76
	Water bodies	0.70	2.37	3.73
4	High albedo land surfaces	0.67	2.49	3.90
	Low albedo land surfaces	0.67	2.40	3.80
	Vegetation/shadow/soil	0.68	2.45	3.86
	Water bodies	0.70	2.37	3.73
5	High albedo land surfaces	0.68	2.45	3.86
	Low albedo land surfaces	0.68	2.40	3.76
	Grass lands	0.68	2.41	3.83
	Forest/tree/soil	0.70	2.31	3.65
	Water bodies	0.70	2.37	3.73

Based on the atmospheric correction parameters shown in Table 4.6, and the emissivity given in Table 4.5, the space-reaching radiance (L_{TOA}) of the ETM+ thermal band was converted to a surface-leaving radiance according to Barsi *et al*. (2005):

$$L_T = \frac{L_{TOA} - L_u - (1-\varepsilon)L_d}{\varepsilon * \tau}$$

where

τ = atmospheric transmission,

ε = emissivity of the surface,

L_T = radiance of a target surface,

L_u = upwelling or atmospheric path radiance,

L_d = downwelling or sky radiance, and

L_{TOA} is the space-reaching or top of atmosphere radiance measured by the instrument.

The emissimity derived from the emissivity classification result developed in chapter 4.5 was applied to compute L_T. The results of each class containing surface leaving radiances was merged with the mosaic method in ENVI.

To generate surface temperatures, the surface leaving radiance (L_T) needs to be converted to the surface leaving temperature. Radiance to temperature conversions are available using the Landsat specific estimate of the Planck curve equation:

$$T = K_2 / \ln [(K_1/L_\lambda)+1],$$

where

T = Temperature in Kelvin

K_2 = Calibration constant 2, 1282.71 Kelvin

K_1 = Calibration constant 1, 666.09 watts m^{-2} $ster^{-1}$ μm^{-1}

L_λ = Spectral radiance in watts $meter^{-2}$ $ster^{-1}$ μm^{-1}.

4.7. Coarse to Moderate Resolution of Surface Temperature Data and Related Thermal Properties from MODIS and ASTER

To compare surface temperatures retrieved using the technique(s) derived from this study, other thermal properties available from the MODIS and ASTER data in addition to surface temperature information were explored. Among current operational satellite sensors, MODIS provides a 1 km coarse spatial resolution for surface temperature, and ASTER has a 90 m moderate resolution for surface temperature data. Both satellite measurements also provide emissivity data. Detailed spectral and spatial information of these three satellite sensors are attached in Appendix Table 4.7.

4.7.1. MODIS Thermal Data

A land surface temperature map was generated from the MODIS data, which were acquired on September 8, 2002. Figure 4.7.1.1 depicts the analyzed subset that covers approximately 500 km by 360 km in the northeastern region of America.

Urban regions associated with the urban heat island effects were clearly noticeable such as the areas around Boston in Massachusetts, Providence in Road Island, Hartford in Connecticut, Philadelphia in Pennsylvania, New York City, and part of New Jersey. Especially the surface temperatures of most urban areas appeared to be above 33 °C (Figure 4.7.1.1.A.), whereas the surfaces over non-urban areas have temperature mostly less than 30 °C. The enlarged image in Figure 4.7.1.1.B presents the study area of New York City and northeastern New Jersey.

A.

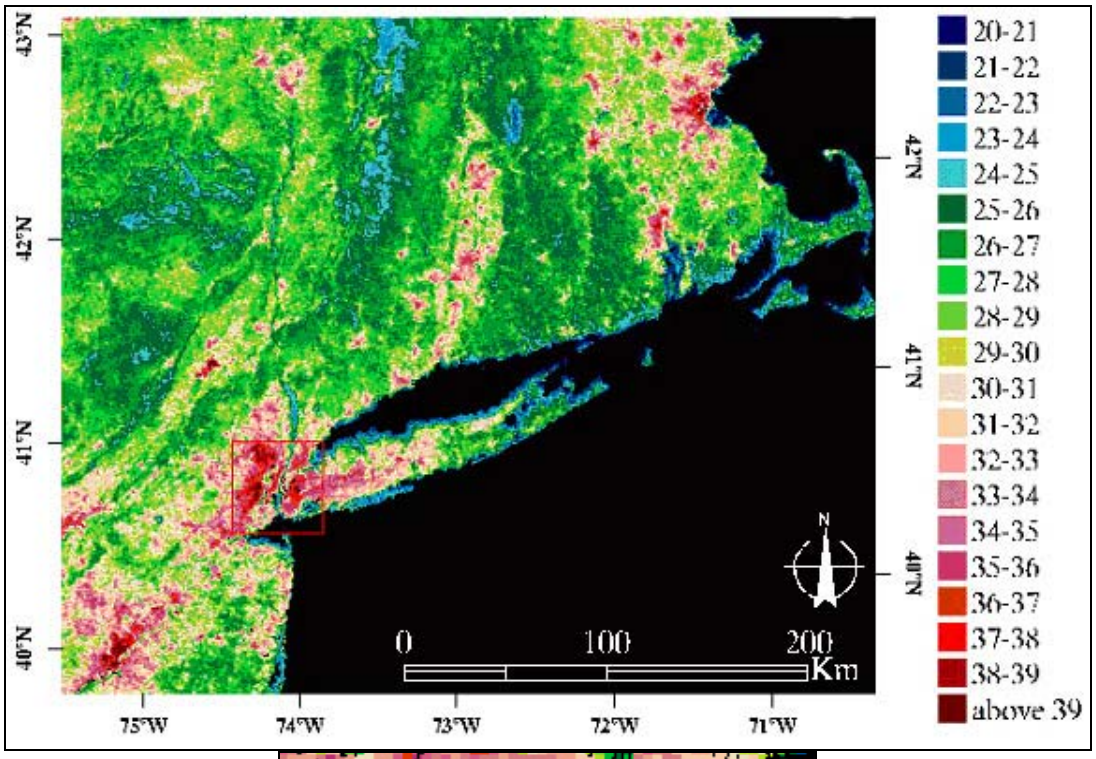

B

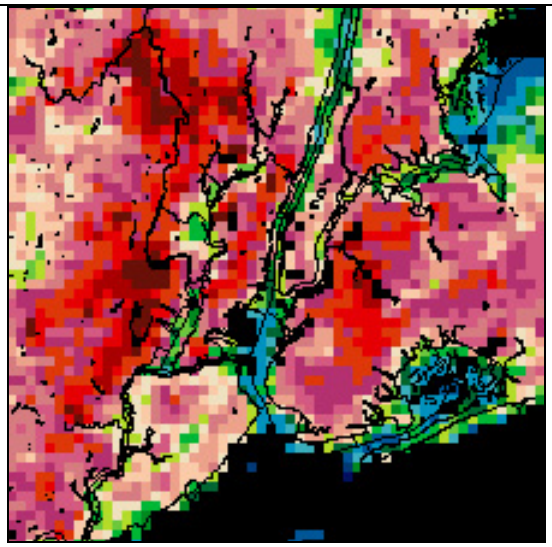

Figure 4.7.1.1.A &B. Land surface temperature (LST) generated from MODIS L2 image with the pixel resolution of 926.6 m, acquired at 15:52 (GMT) in September 8, 2002: A: Regional scale of the LST; B: Details of the study area, New York City and part of New Jersey as shown in A.

The distribution statistics of MODIS surface temperature over the study area (Appendix Table 4.7.1) showed that New Jersey counties cover 16.8% of surface with temperatures above 36 °C. In New York City, 7.3% of the surface showed temperature above 36 °C, which is 50% less compared to the New Jersey area. The distribution histogram in Figure 4.7.1.2 shows the comparison between New York City and New Jersey.

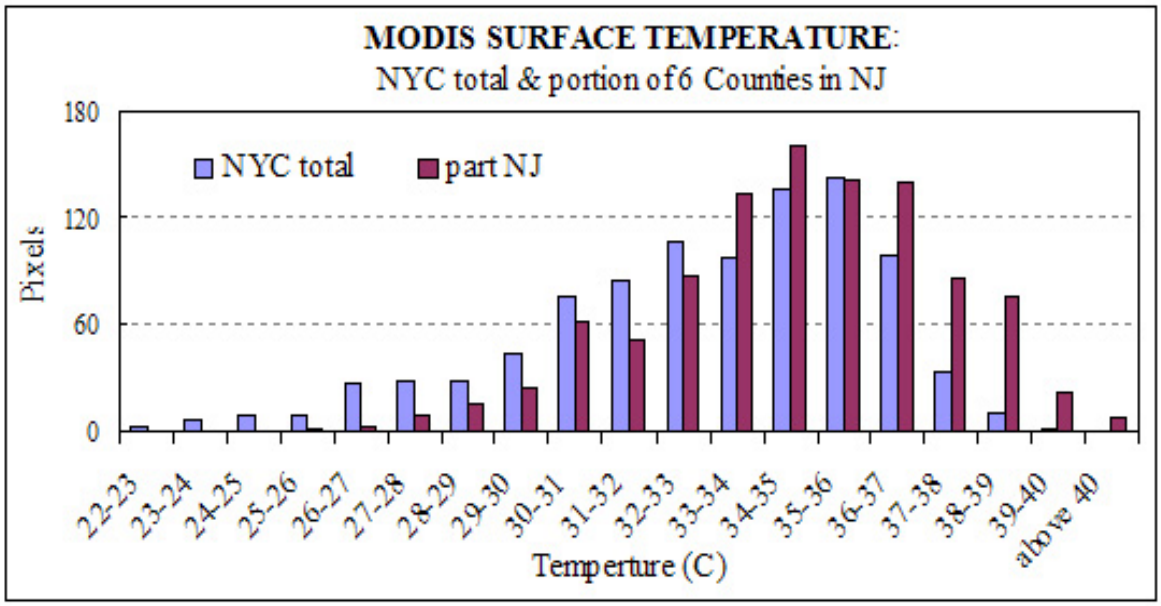

Figure 4.7.1.2. MODIS surface temperature distribution histogram of five counties in New York City and part of six counties in northeastern New Jersey (image acquired at 15:52 (GMT) in September 8, 2002.

The wavelength regions used for MODIS emissivity measurements are similar to the Landsat ETM+ thermal band and the two ASTER emissivity bands 14 and 15. The emissivity maps generated from MODIS data for September 8, 2002, showed in Figure 4.7.1.3.A & B.

The average emissivity of most urbanized areas appeared to be 0.970 in the 10.78-11.28 μm waveband, and 0.976 in the 11.77-12.27 μm waveband (Figure 4.7.1.3.A & B). The emissivities over highly urbanized areas appeared to be relatively lower than those observed in non-urban areas. The average emissivity of non-urban areas was 0.986 at the 10.78-11.28 μm waveband, and 0.990 at the 11.77-12.27 μm waveband. The highest frequency range in emissivity that appeared over land surfaces at the wavelength 10.78-11.28 μm and was between 0.967 and 0.972.

It is displayed in red for areas in the zoomed image in Figure 4.7.1.3.A. For the wavelength 11.77-12.27 μm in Figure 4.7.1.3.B, the highest frequency range for emissivity was between 0.973 and 0.982.

For comparing MODIS emissivity with ASTER emissivity, an averaged emissivity map was generated from the two separated emissivity bands of MODIS data and depicted with a histogram distribution of the study area (Figure 4.7.1.4). The mean emissivity of the MODIS image over the land surfaces in the study area showed 0.973, and the range was from 0.729 to 0.990. The highest frequency of mean emissivity was in the range between 0.973 and 0.974 and covered 15.4% of New Jersey counties and 11.6% of New York City counties. The surface coverage of the mean emissivity below 0.972 appeared slightly higher in New York City with 3.5% (Figure 4.7.1.4).

The detailed mean emissivity distributions and frequencies of five counties in New York City and six counties in northeastern New Jersey are summarized in Appendix Table 4.7.1.2.

A.10.78-11.28 μm

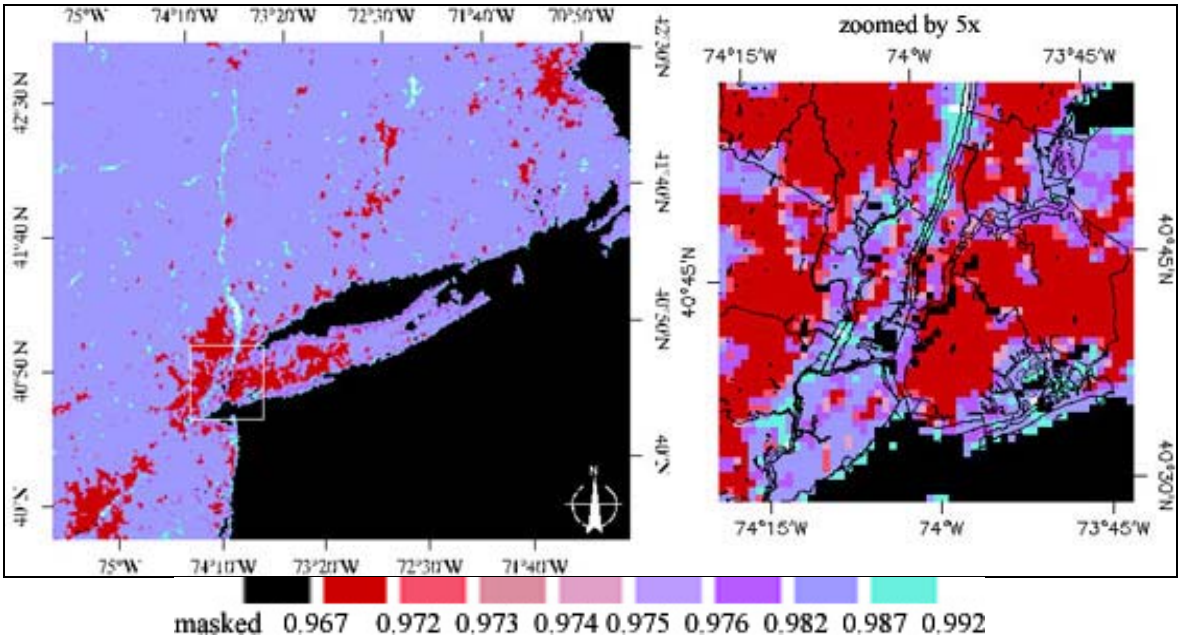

B.11.77-12.27 μm

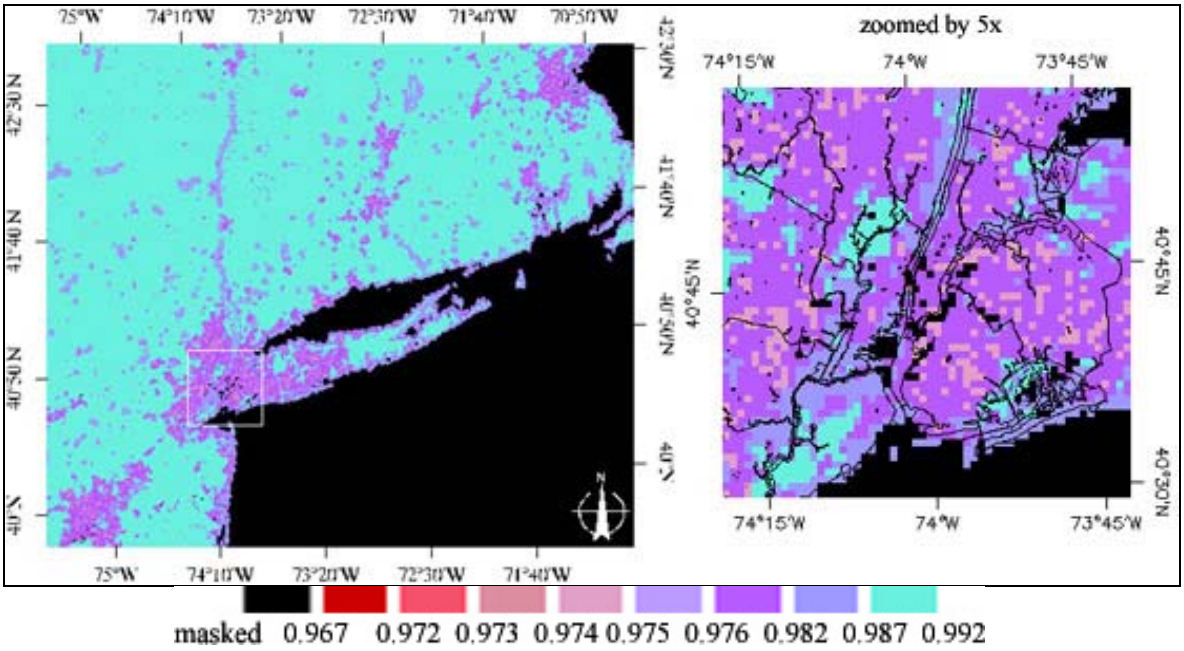

Figure 4.7.1.3. Land surface emissivity generated by MODIS L2 image acquired at 15:52 GMT in September 8, 2002 at two different wavelengths.

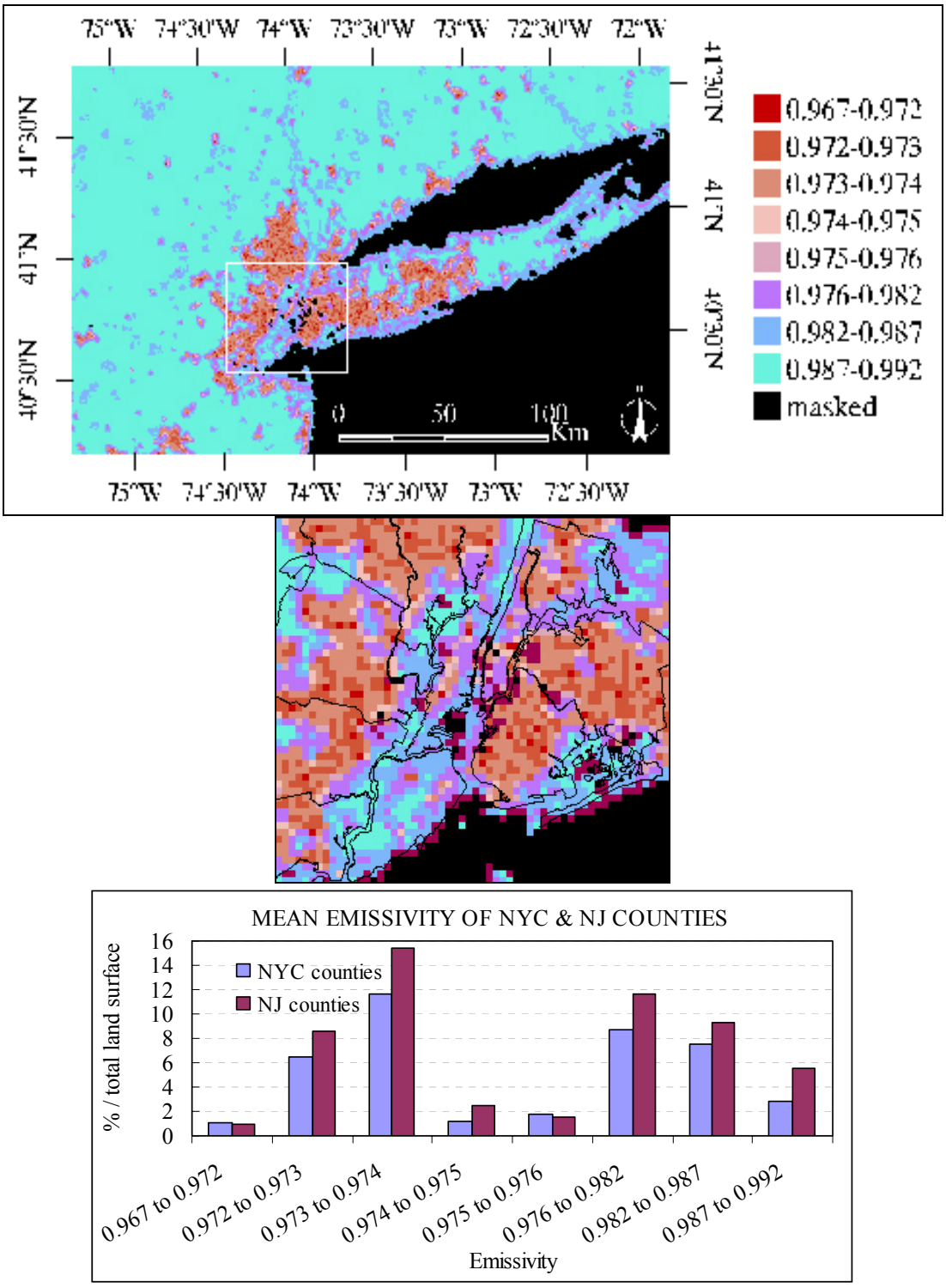

Figure 4.7.1.4. The mean emissivity of MODIS band 31 (10.78–11.28 µm) and band 32 (11.77–12.27 µm), and the histogram of five counties in New York City and part of six counties in northeastern New Jersey at 15:52 (GMT) in September 8, 2002.

To exam the emissivities in the thermal infrared region in relation to the reflectance in the visible region, a reflectance image was generated using the average surface reflectance of the MODIS bands 0.644 μm, 0.465 μm, and 0.553 μm, of which the result is displayed as a color density sliced image (Figure 4.7.1.5).

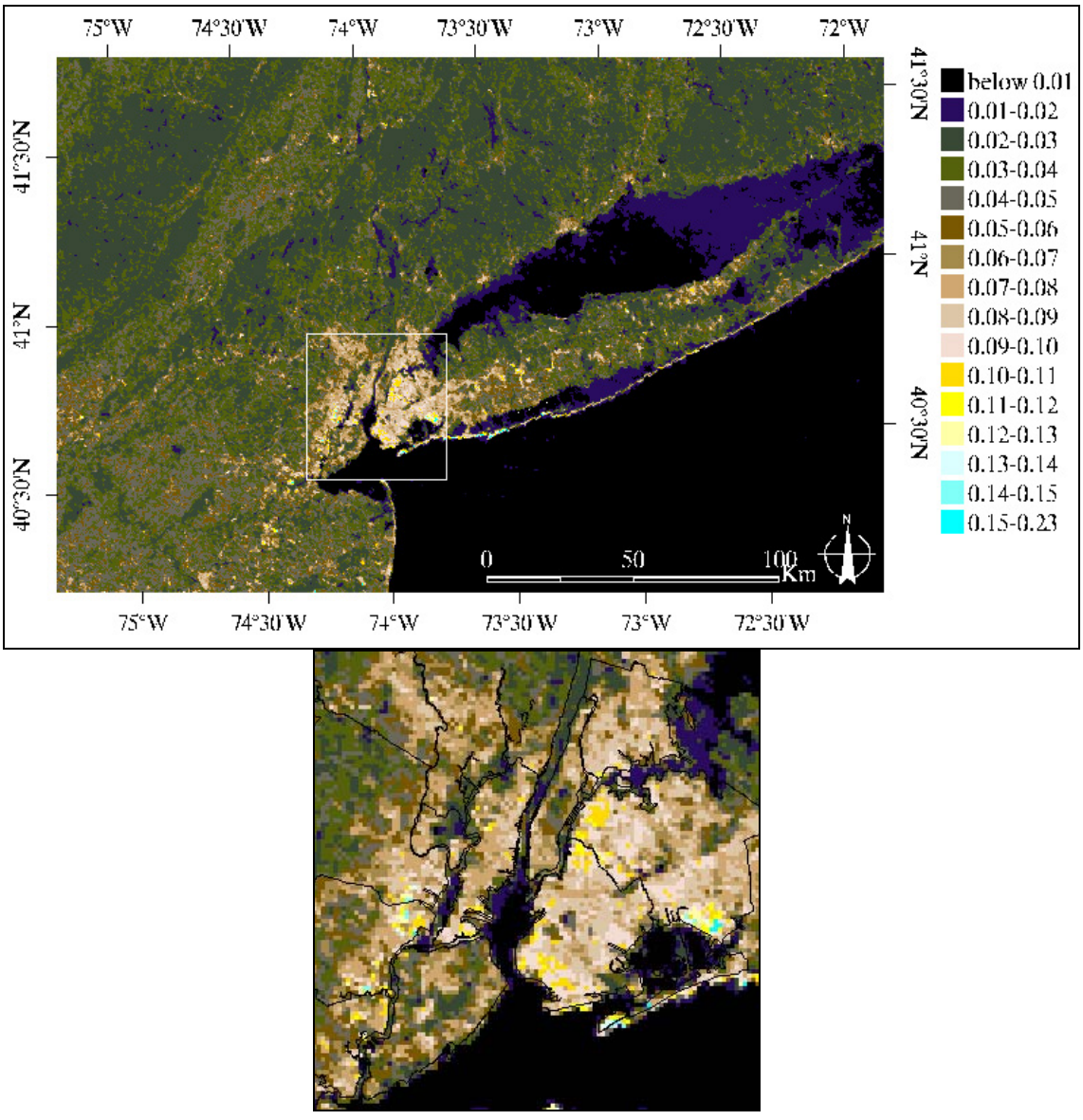

Figure 4.7.1.5. MODIS reflectance image acquired at 15:52 GMT in September 8, 2002. The pixel resolution of the top overview image was about 463 m; the zoomed image in the bottom was enlarged by a factor of three.

The average reflectance from the visible wavelength region showed values below 0.02 (at the scale of 0 to 1) for most water bodies and below 0.03 for wetlands or marshes and shadow areas in Figure 4.7.1.5. Vegetation covered regions, especially those associated with dense forests, appeared to have a reflectance range between 0.03 and 0.05, most grass lands such as meadows, and some part of shadow zones showed values between 0.04 and 0.06. The visible region reflectance distributions of the study area enlarged in the bottom image in Figure 4.7.1.5 showed that most of impervious surfaces were represented by above 0.07 reflectance levels covering about 28%. The highest frequency of 12% appeared in the reflectance level between 0.07 and 0.08. Relatively high reflectance areas above 0.11 were about 2.5% mostly located in high density of industrial zones, such as the western and southern part of Queens, the northern and southern part of Brooklyn, and the JFK and Newark airports. Some of these sites coincided with high emissivities in the daytime emissivity data. Other high reflectance targets were also distinguishable over beach areas.

One of advantages using MODIS data is the availability of day and night time temperature measurements with daily coverage. Since the thermal inertia is one of the important factors in the evaluation of urban heat island effects, the availability of both day and night time surface temperature data makes it possible to derive the thermal inertia. To exam apparent thermal inertia, a difference map of day and night time temperature was generated, and the results are presented as a map, with a zoomed image and a frequency distribution, in Figure 4.7.1.6.

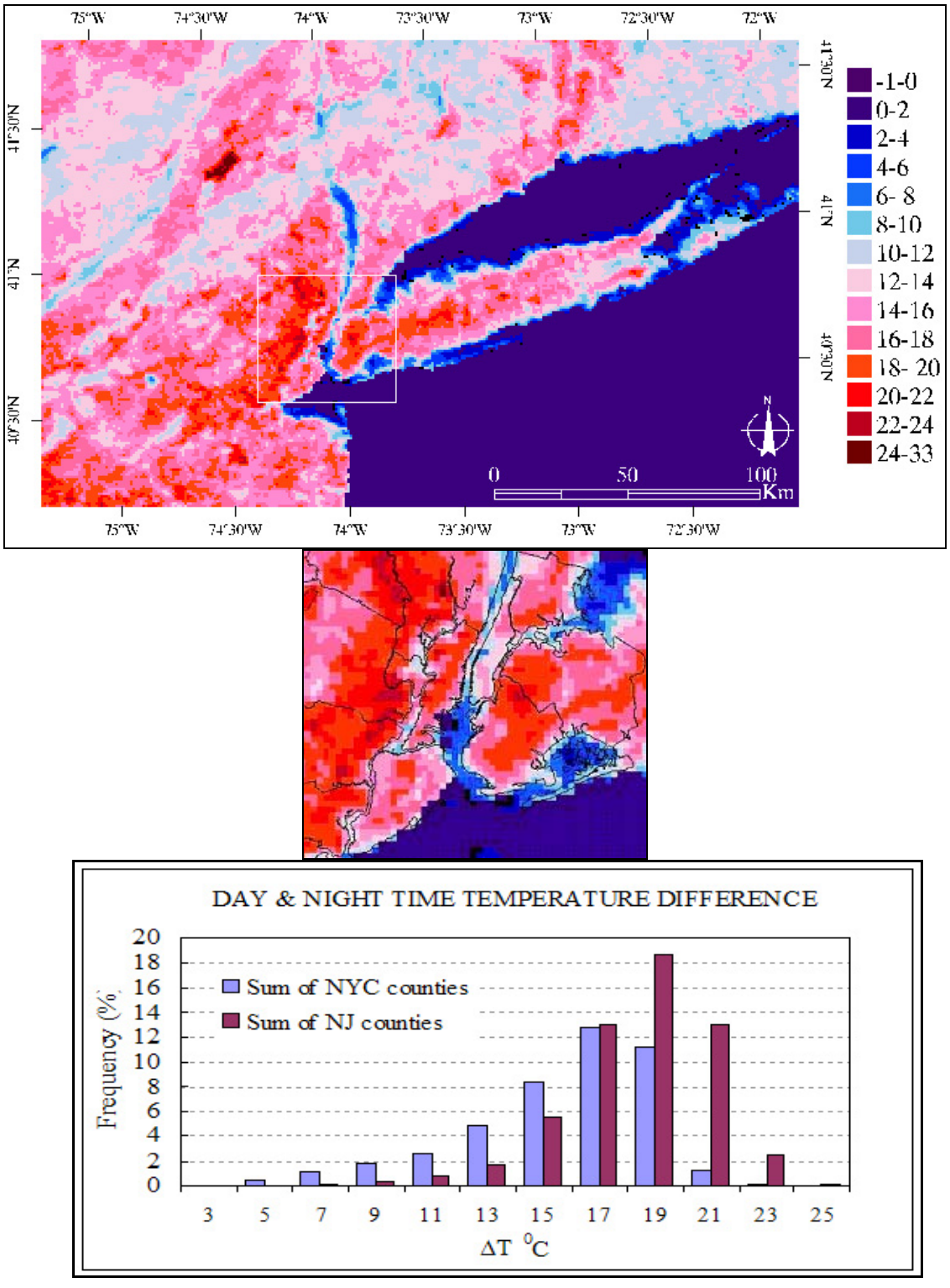

Figure 4.7.1.6. MODIS day-night time surface temperature difference and frequency distribution in New York City and New Jersey at 15:52 (GMT) in September 8, 2002. The zoomed image shows the study area.

Most highly urbanized areas showed above 18 °C day-night time temperature difference. In the histogram analysis, six counties of New Jersey depicted a higher frequency of 47% above 18 °C of day-night time temperature difference compared to 25% from five counties of New York City. The significant day-night time temperature difference above 20 °C appeared more areas in New Jersey counties where ten times higher than in New York City counties but showed an opposite trend in the temperature difference level below 10 °C.

Further analysis was carried out to estimate the relationship between the apparent thermal inertia and emissivity, reflectance, day-night time temperature differences. To generate an apparent thermal inertia map, the apparent thermal inertia for each pixel was calculated in the following equation (Jensen, 2000),

$$ATI = \frac{1 - A}{\Delta T}$$

where, *ATI* is the apparent thermal inertia with the unit of cal cm^{-2} $sec^{-1/2}$ $ºC^{-1}$, *A* is the reflectance measured in the visible during daytime (Kahle et al., 1981: Sabins, 1987), and ΔT is the change in temperature determined by subtracting the nighttime apparent temperature from the daytime apparent temperature. For this computation, the reflectance value A for each pixel was generated by the average reflectance from the visible bands of MODIS 09 GH data.

The apparent thermal inertia map in Figure 4.7.1.7 represents a range from 0.03 to 0.30. The apparent thermal inertia in highly urbanized areas with ranges below 0.045 coincides with the regions that have large temperatures difference of about 20 ºC in the day-night coverage.

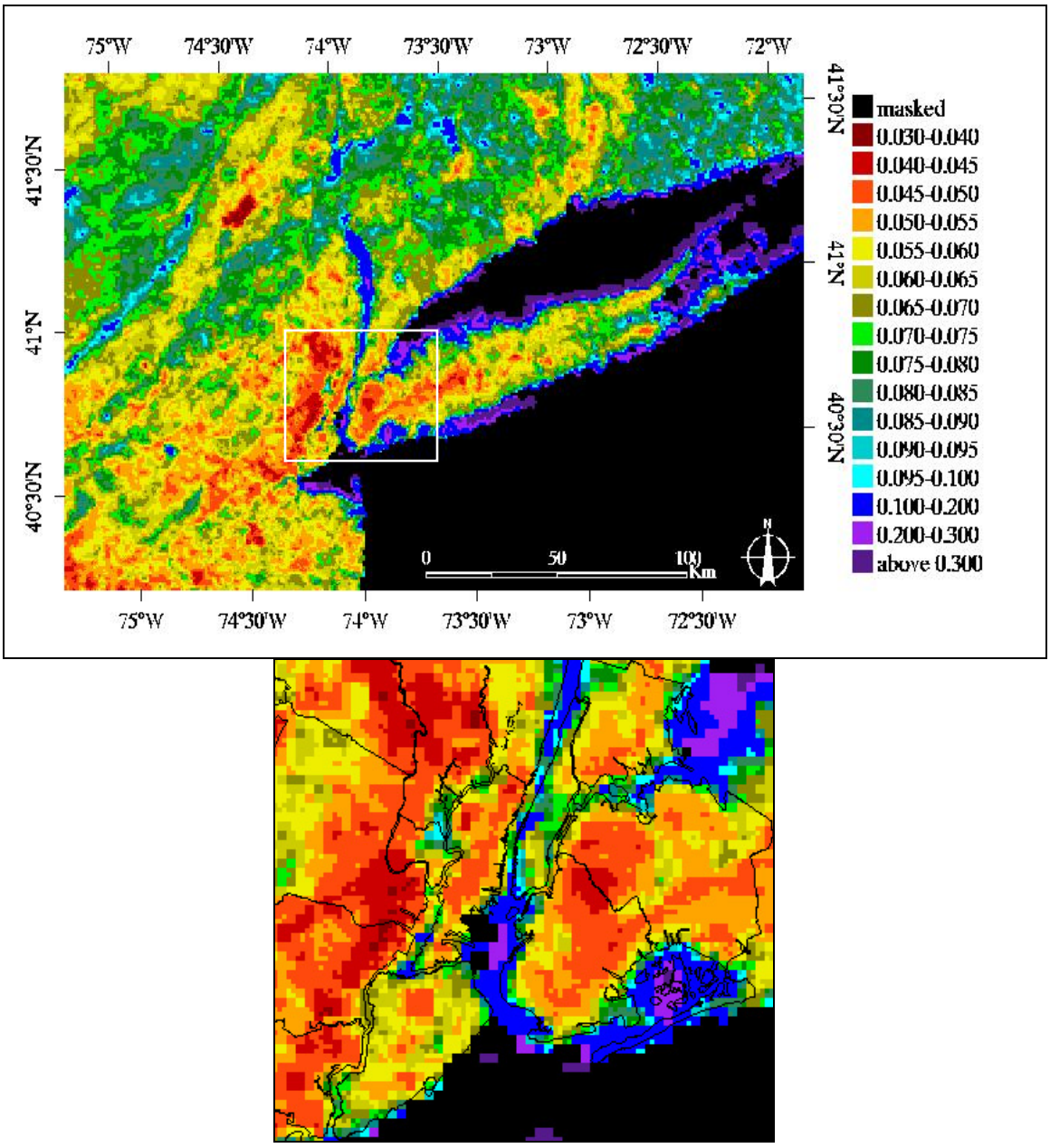

Figure 4.7.1.7. Apparent thermal inertia map derived from MODIS image observed in September 8, 2002. The zoomed image shows the study area.

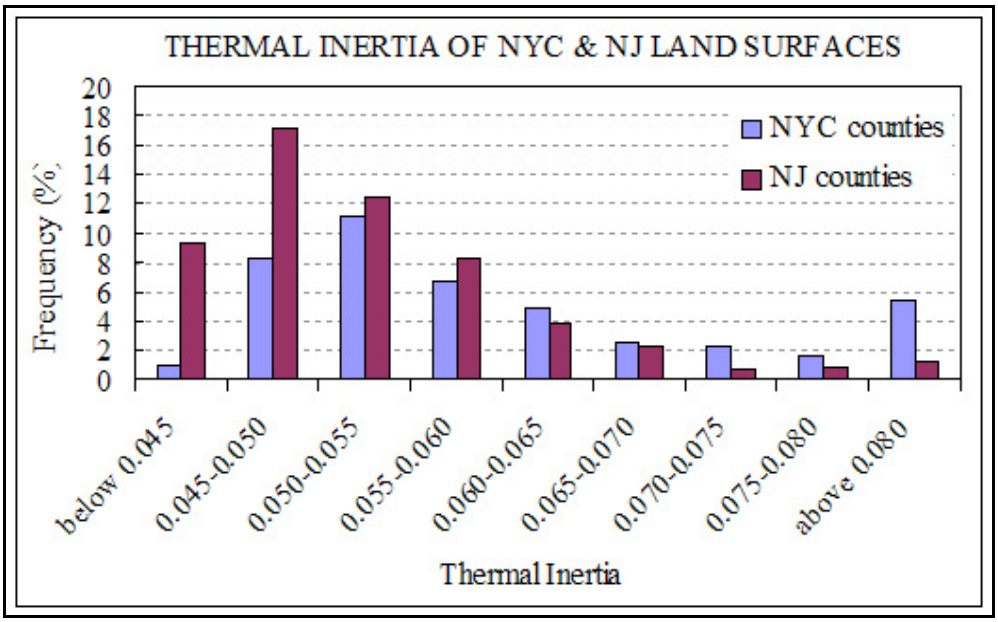

Figure 4.7.1.8. Frequency distribution of apparent thermal inertia in New York City and New Jersey at 15:52 (GMT) in September 8, 2002.

The histogram distribution in figure 4.7.1.8, depicting the apparent thermal inertia in NYC and NJ, showed an opposite pattern that was previously observed in the day-night temperature difference histogram. The apparent thermal inertia below 0.06 appears at a high frequency over the New Jersey counties. Significance was noticeable especially in the apparent thermal inertia below 0.05 level in New Jersey counties with values higher by a factor of two compared to the frequency distribution in New York City counties. As expected, the greater day-night temperature difference shows a direct link with the lower thermal inertia of land surfaces.

Correlations among the different variables (surface temperature, emissivity, reflectance, day-night temperature difference, and apparent thermal inertia) derived from MODIS data are summarized as 2-dimensional scatter plots with correlation coefficients in Figure 4.7.1.9.

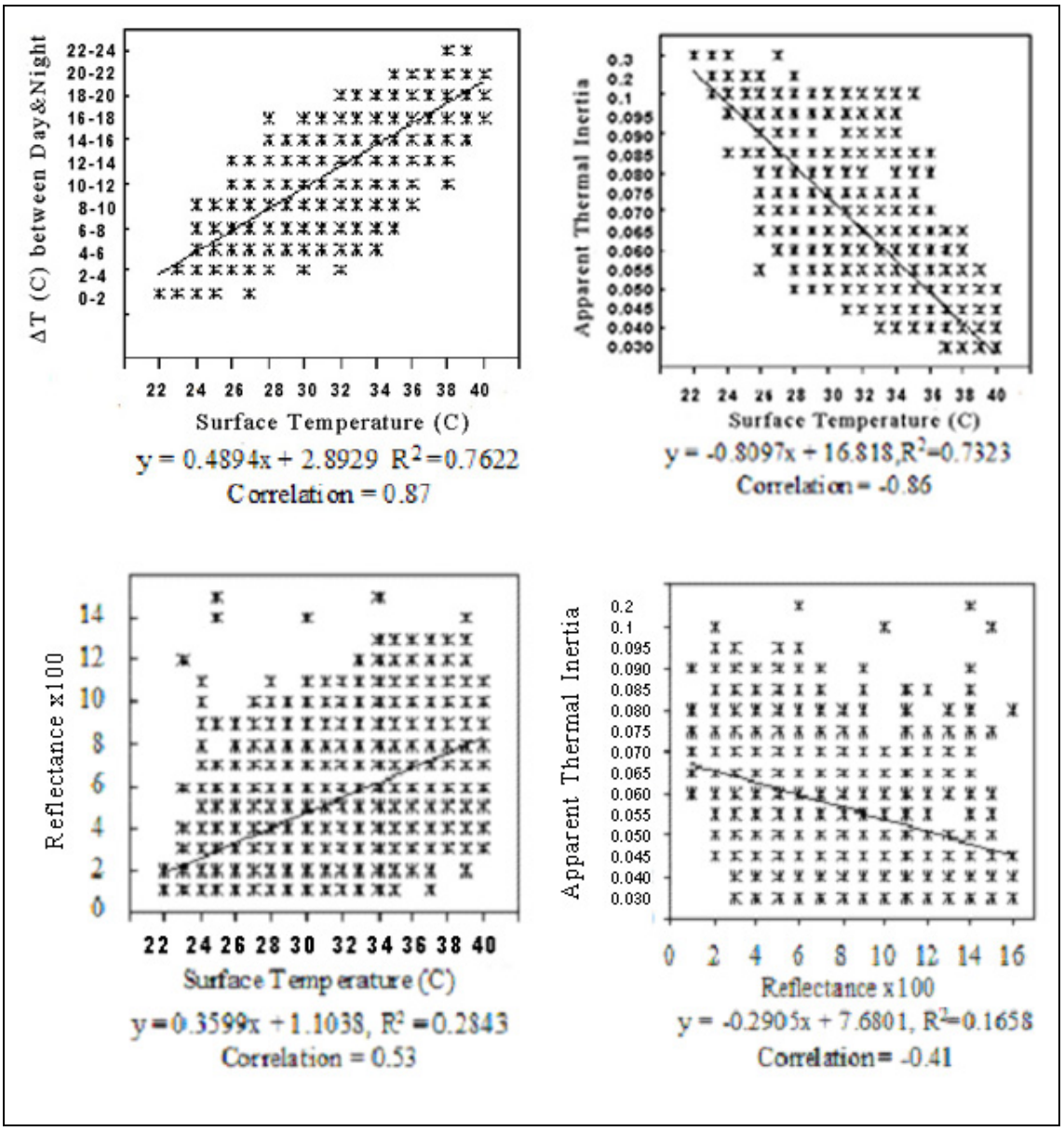

Figure 4.7.1.9. Scatter plots of surface variables derived from MODIS measurements in September 8, 2002.

Strong correlation appears between the MODIS surface temperature and the temperature difference between day and night time, and between surface temperature and apparent thermal inertia. The relationship between surface temperature and the temperature difference between day and night time shows the highest positive correlation of 0.87. The relation between surface temperature and apparent thermal inertia has the highest negative correlation of -0.86. Moderate level of correlation appears between surface temperature and reflectance with a positive correlation of 0.53, and negative correlation of -0.41 between reflectance and apparent thermal inertia, respectively. No significant correlation was noticeable between surface temperature and emissivity classes in MODIS measurements.

4.7.2. ASTER Thermal Data

A land surface temperature map over the study area was generated from ASTER LST 08 data that were acquired also on September 8, 2002 (Figure 4.7.2.1). Unlike the MODIS land surface temperature data, which were generated based on two emissivity measurements, the ASTER LST 08 data were based on five emissivity bands with a 90 m resolution.

The histogram distributions of ASTER surface temperature are displayed below the surface temperature map in Figure 4.7.2.1. The highest frequency of surface temperature in the study area appeared between 38 °C and 40 °C with a 13.1% surface coverage. Vegetation areas including forest, park trees, grasslands, and wet lands, showed a temperature range from 26 °C to 34 °C.

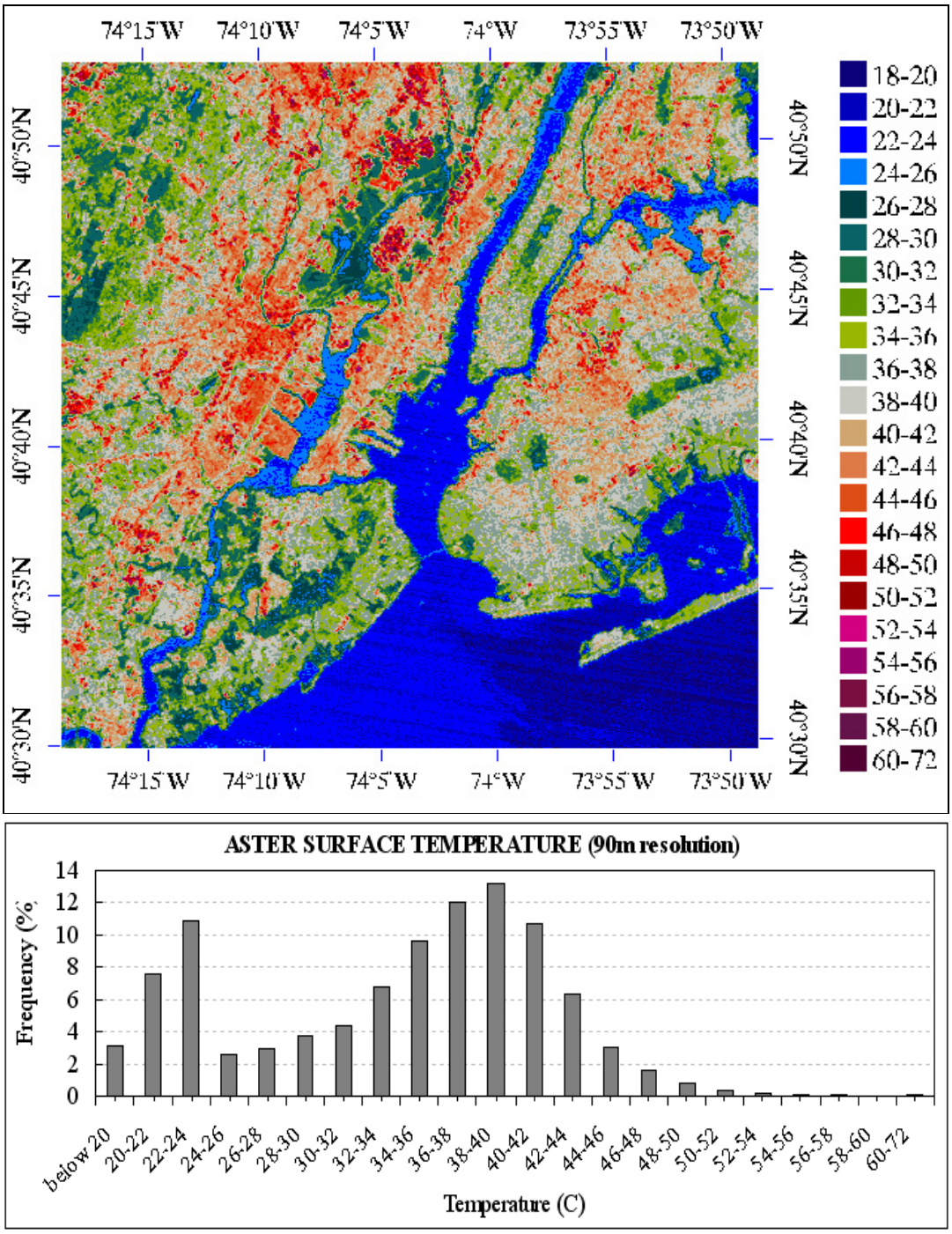

Figure 4.7.2.1. The ASTER surface temperature map and the frequency distribution histogram for the image acquired in September 8, 2002.

It was not possible to estimate precisely with the temperature data because portions of manmade impervious surfaces exerted at the same temperature levels. Part of

shadow zones over manmade structures has a temperature range of 30 ºC to 32 ºC, which are noticeable in some of the vegetated areas. Some mixed pixels combining street trees and concrete or cement paved areas, exert also similar levels of temperatures that were observed over cemeteries and dry grass covered lands. The overall percentage of the surface temperature above 36 ºC was about 50% within the study area. Surface coverage above 36 ºC with the MODIS LST image in the same study area was about 16%. This great discrepancy between MODIS and ASTER data is most probably due to the coarse pixel resolution of MODIS compared to that of ASTER LST.

4.7.3. Evaluation of MODIS LSTs and ASTER LSTs

Land surface temperatures were compared with five counties in New York City and part of six counties in New Jersey. Since a visual distinction of higher frequency above 40 °C surface temperatures was more noticeable over New Jersey relative to New York City counties, a detailed comparison was carried out by vector overlaying analysis. In addition, a comparison of the ASTER surface temperature with the MODIS land surface temperature was carried out in various counties that also showed the discrepancy between the two data sets (Table 4.7.3). As shown in Table 4.7.3, the average land surface temperature derived from ASTER was 4.4 ºC higher than the one from MODIS. The greatest difference appeared in the Bronx with 5.4 ºC, and the smallest difference in the northeastern part of Middlesex County with 1.9 º C. It indicates that the land surface temperatures generated from MODIS data provide underestimated values.

Table 4.7.3. County level comparison between the average land surface temperature obtained by ASTER and MODIS.

COUNTY	ASTER LST (average ºC)	MODIS LST (average ºC)	DIFFERENCE (ΔºC)
Bronx, NYC	38.9	33.2	5.4
Passaic, NJ	40.7	35.8	4.9
Hudson, NJ	38.9	34.5	4.4
Manhattan, NYC	36.0	31.8	4.1
Bergen, NJ	38.8	34.8	4.0
Queens, NYC	37.3	33.6	3.7
Brooklyn, NYC	37.2	33.6	3.6
Union, NJ	38.9	35.4	3.5
Essex, NJ	37.3	34.2	3.1
Staten Island, NYC	34.0	31.2	2.8
Middlesex, NJ	37.5	35.6	1.9
Mean	37.8	34.0	3.8

Frequency comparisons among counties and between New York City and New Jersey were generated by vector overlaid subsets in Figure 4.7.3.1. The surface temperature ranges between 35 ºC and 40 ºC in New York City, the highest frequency above 6% was observed in the Queens county, and above 4% in Brooklyn. These two counties and the Bronx show also a high frequency in the surface temperature ranges above 40 ºC. Among New Jersey counties, especially the Essex county showed distinct frequencies in the temperature ranges between 30 ºC and 45 ºC. The frequency above 45 ºC was relatively higher in Essex, Hudson, Union, and Bergen county in New Jersey.

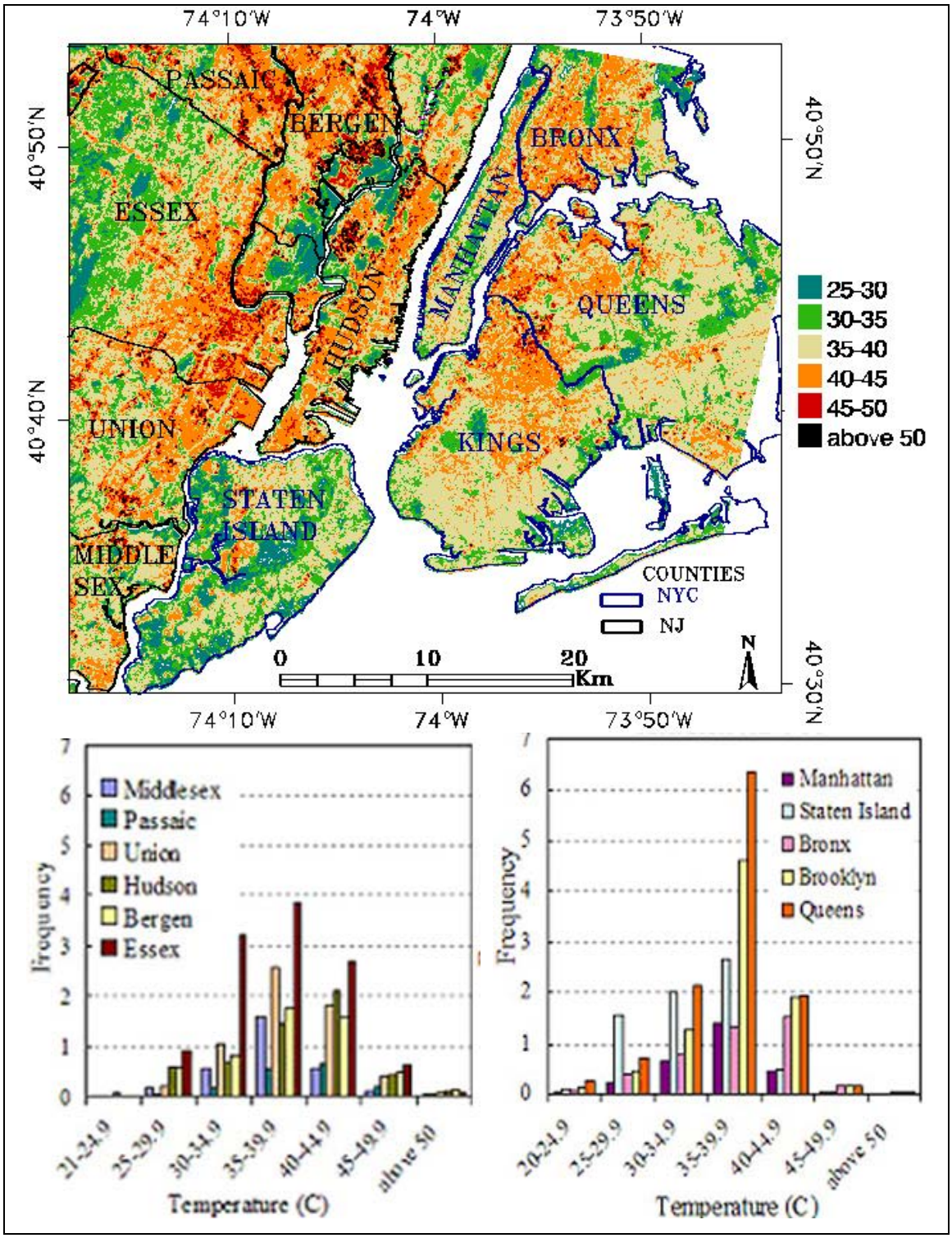

Figure 4.7.3.1. Frequency comparison of ASTER land surface temperatures of five counties in New York City and six counties in New Jersey.

The surface temperatures above 40 °C covered 6.9% of the land surface in New York City counties and 12.2% in New Jersey counties. High frequencies were observed in Essex, Hudson, Union, Bergen, Queens and Brooklyn. Several clusters of high temperature above 42 °C were noticeable over the Newark airport in Essex and Union county, the south of Secaucus in Hudson county, the south of Teterboro airport in Bergen county in New Jersey, and Maspeth in Queens and Linden Hill in Brooklyn county in New York City.

To exam the relationship between surface temperature and emissivity, the ASTER surface emissivity maps were generated using the average emissivity measured at the wavelength region between 8.13 μm and 11.65 μm (Figure 4.7.3.2.A), and the average measurements between 10.25 μm and 11.65 μm (Figure 4.7.3.2.B). The detailed distribution of five thermal bands and two thermal bands emission are presented in Appendix Table 4.7.3.

The two bands mean (10.25-11.65 μm) emissivity range between 0.95 and 0.96 and depicted the highest frequency in the study area, however, this result differed from the emissivity map that were generated by the average measurements of five emissivity bands, which depicted high frequencies in the emissivities between 0.92 and 0.94. There are also great discrepancies in the emissivity ranges between 0.90 and 0.92, and between 0.94 and 0.97. The major emissivity levels for impervious surfaces appeared to be below 0.93 in the mean of five emissivity bands shown in Figure 4.7.3.2.A. The impervious surfaces appeared in Figure 4.7.3.2.B generated by the mean of two emissivity bands showed less coverage as core urban areas with the emissivity below 0.9.

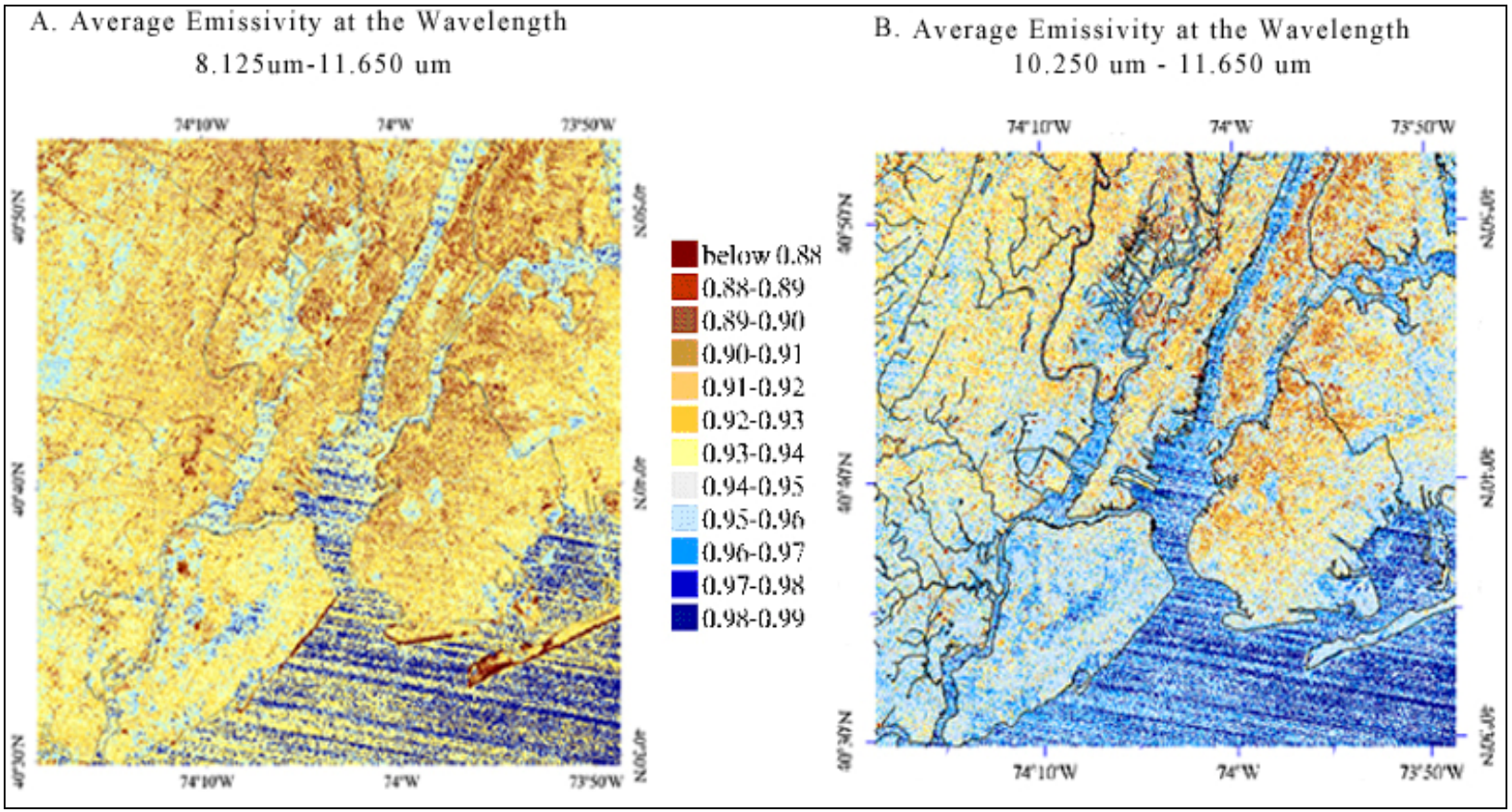

Figure 4.7.3.2. ASTER surface emissivity maps generated using the mean of the ASTER emissivity measurements at wavelength from 8.125 to 11.650 μm for A, and from10.25μm to11.65μm for B.

There are some obvious impervious areas that displayed the emissivity level between 0.95 and 0.96 in Figure 5.2.B. In spite of the great discrepancy between two emissivity maps from average measurements of five thermal bands and two thermal bands, further analysis was carried out focusing on the emissivity map from longer wavelength measurements between 10.25 μm and 11.65 μm, which coincide with a part of thermal wavelength range 10.40–12.50 μm in ETM+ measurement.

The ASTER emissivity distribution patterns in New York City and New Jersey are presented in Figure 4.7.3.3. New Jersey counties have higher frequency especially in the emissivity ranges between 0.91 and 0.95 whereas most of counties in New York City show a relatively high frequency in the emissivity ranges between 0.95 and 0.96. The emissivity ranges below 0.94 in overall land surfaces are related to low or intermediate level of reflectance by impervious surfaces.

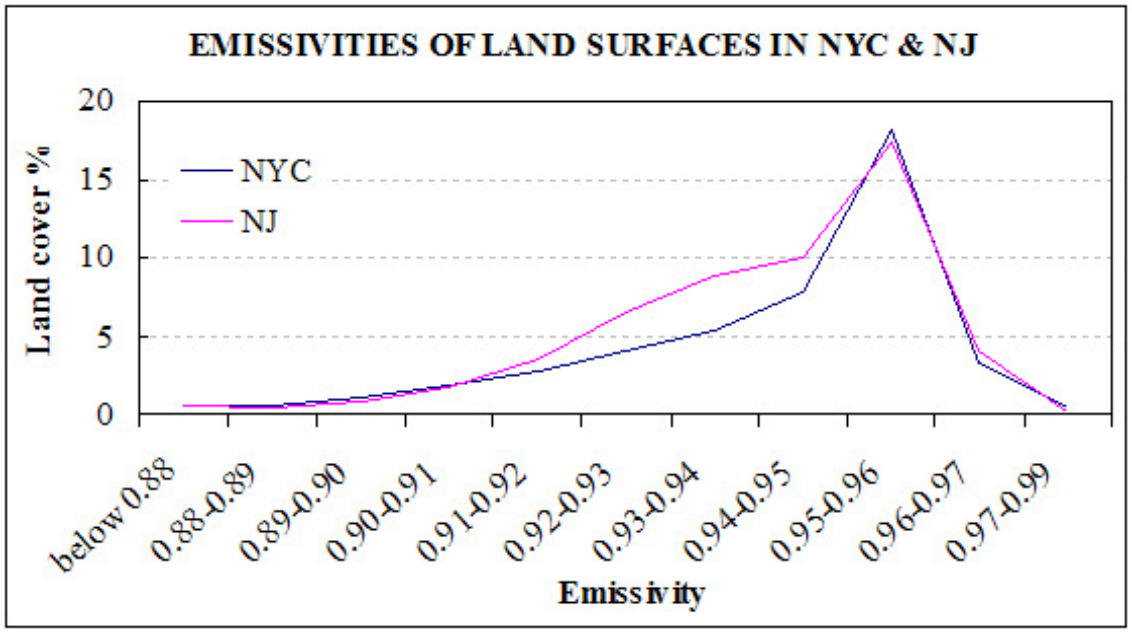

Figure 4.7.3.3. Comparison of land surface emissivities of ASTER in New York City and New Jersey.

Further identification analyses were carried out with sub-sets of several "hot zones" as shown in Figure 4.7.3.4. A & B. The images are overlaid with road (purple line) and railroad (black line) vector layers, and the 2.8 m pixel resolution QuickBird image for New York area and 1 m pixel resolution of aerial photographs for the New Jersey areas.

Figure 4.7.3.4.A represents the industrial areas in parts of Queens and Brooklyn county in New York City. The 2.8 m pixel resolution of QuickBird ortho-image over Long Island City and Maspeth in the New York City area reveals that the ASTER land surface temperatures above 48 ºC are associated with large size warehouses that have black tar rooftops. In this region, there is no significant correlation between high temperatures and the areas covered by highways and railroads.

Figure 4.7.3.4.B represents "hot zones" in New Jersey counties. Theses areas appear to be warehouse type of buildings in the south of the Teterboro airport in Bergen county and the south of Secaucus in Hudson county. These surfaces generally depict the level of emissivity below 0.90, and show surface temperature above 50 °C. The high temperature spots in these areas seem to be much related to high density of dark tar asphalt paved highways and dark metallic railways. Some pixels in the high temperature area in the ASTER surface temperature map show coincidence with low emissivities of metallic surfaces that appeared in the emissivity map generated by the average emissivity of band 13 (wavelength 10.25-10.95 μm) and band 14 (wavelength 10.95-11.65 μm). However, most of low emissivity pixels associated with metallic surfaces may present slightly higher level than the actual values since the pixel size of ASTER LST and LSE is a 90 m which usually depicts a mixed area than .a single metallic object.

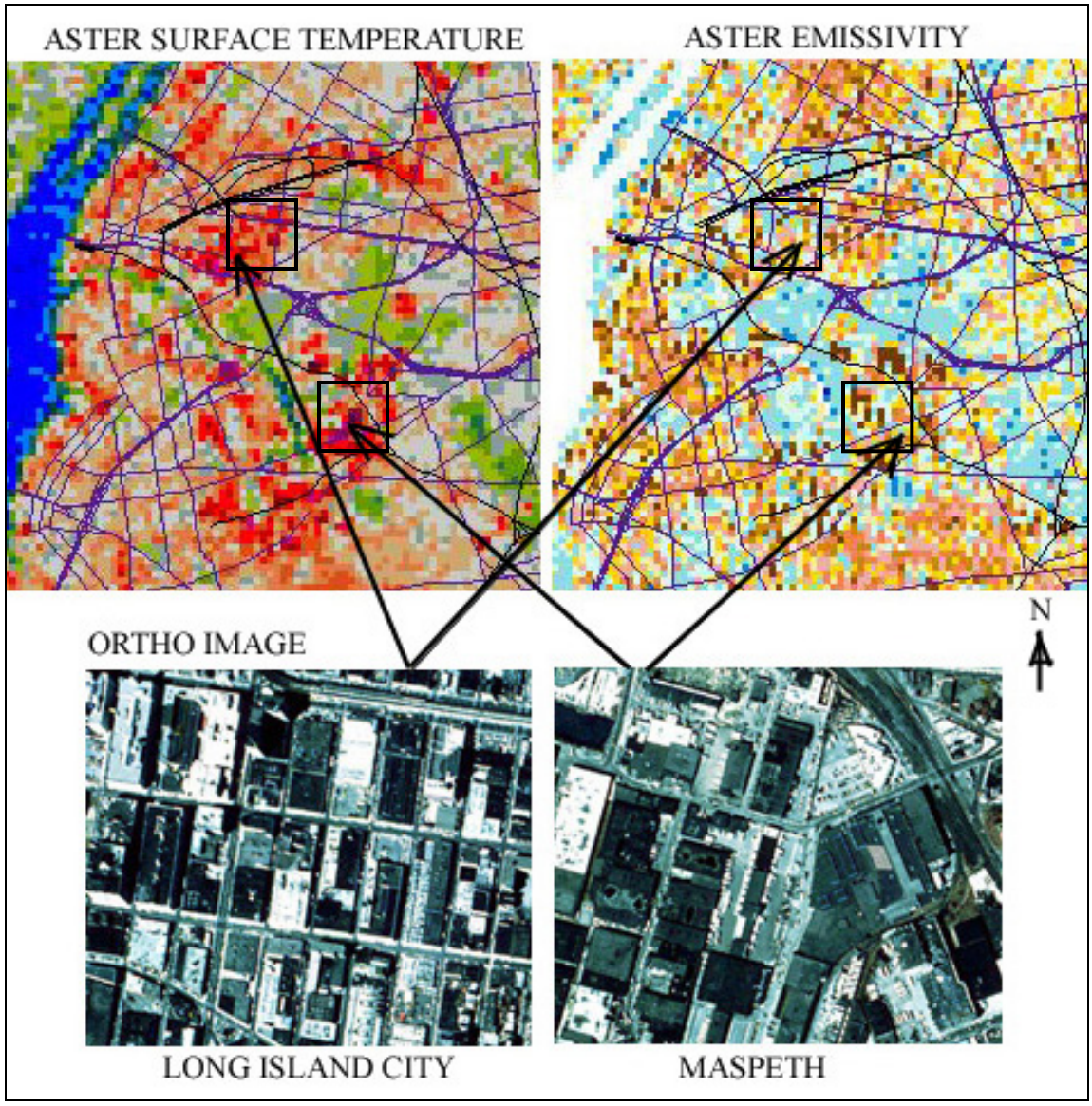

Figure 4.7.3.4. A. Subsets of representative high temperature sites over Queens county in New York City from the ASTER surface temperature and emissivity maps. The arrows pointing at the upper left in the surface temperature and emissivity maps for Long Island City in Queens county; the arrows pointing to the lower right in the surface temperature and emissivity maps indicate Linden Hill and Maspeth.

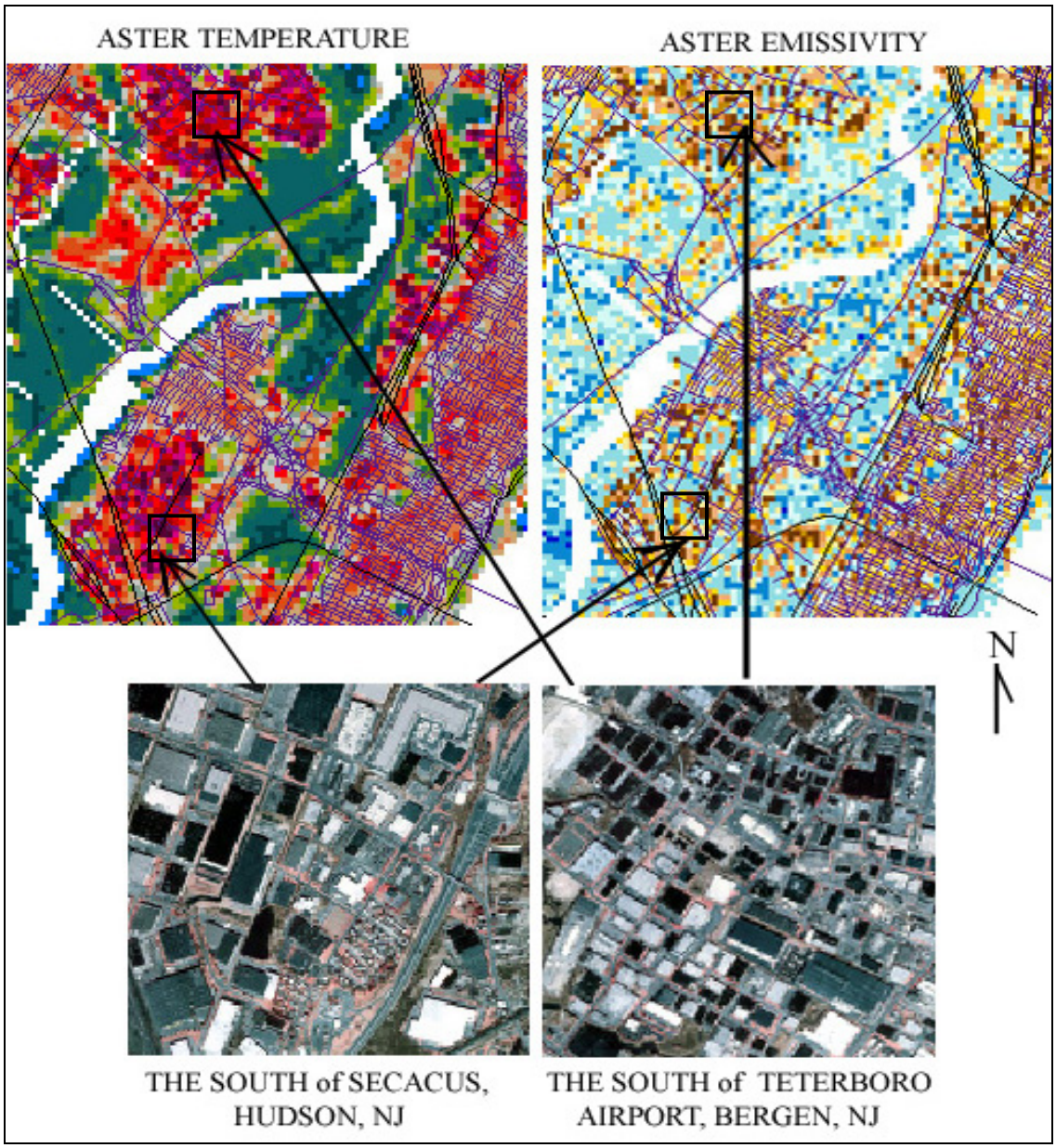

Figure 4.7.3.4.B. Subsets of representative high temperature sites over Hudson county in New Jersey from the ASTER surface temperature map and the ASTER emissivity map. The arrows pointing at the upper middle in the surface temperature and emissivity maps show the south of Teterboro airport in Bergen county, and the arrows pointing to the lower left in the surface temperature and emissivity maps indicate the south of Secaucus in Hudson county.

The comparison between MODIS and ASTER data resulted in as evaluation which can be summarized as follows:

1) MODIS data have the benefit of high temporal resolution for both day and night time thermal data although its coarse spatial resolution is not appropriate for urban or local scale thermal studies.

2) ASTER LST and LSE data are superior to other satellites that measure thermal data with higher spatial resolution and five multi-thermal channels. The disadvantage of ASTER LST and LSE are high noise levels that were found by analyzing the data over water bodies. Furthermore, poor temporal resolution may be a disadvantage if operational coverage is required.

5. Generation and Evaluation of Enhanced Resolution ETM+ Thermal Data

The previous studies have let to the primary source of data used in the retrieval method derived from this study, the ETM+ thermal data. These data are advantageous for urban scale thermal studies since it provides the highest spatial resolution among conventional satellite thermal measurements. Surface temperature retrieval is achieved from the spectral region between 10.4 and 12.5μm and conversion of radiance measured at satellite altitude to surface leaving radiance. Surface temperature derived by using a unity emissivity without atmospheric correction results in an underestimation of the true kinetic temperature of targets. In order to increase the accuracy of surface temperature retrieval from the Landsat ETM+ satellite measured radiance data, differentiated emissivities as well as proper atmospheric corrections need to be applied.

The temperatures extracted from ETM+ data used a unity emissivity in Figure 5.1. (A) and an emissivity 0.9 in (C) were compared with the surface temperature map of ASTER LST (B). Both map (A) and (C) displayed in Figure 5.1 were resampled to a 90 m pixel size. The surface temperature map (C) was generated by applying an emissivity of 0.9 and atmospheric corrections with a 90 m pixel size. The same color scale between 18°C and 72°C with two-degree interval was applied for all images to generate temperature maps.

As shown with the temperature maps in Figure 5.1 and the statistical distribution in Appendix Table 5.1, surfaces, such as water bodies and vegetation areas, are about 2 to 4 °C lower in the ETM+ image (A) compared to those obtained by ASTER LST (B). Towards higher temperature targets, the discrepancy between the two temperature data sets reached 10 °C. Above 52 °C, 0.55% of ASTER LST data were detected, but none of ETM+ data in (Figure 5.1.A). Comparing the ASTER LST with the ETM+ surface temperature map (Figure 5.1.C), the overall average of ETM+ surface temperature was about 3 ºC higher than the ASTER LST.

The highest frequency over land surface in the ETM+ surface map appeared in the temperature range between 40 ºC and 41 ºC while the ASTER LST map showed the highest frequency in 37 ºC (Figure 5.2). It indicates that the application of a single emissivity 0.9 for urban surfaces results in an overestimation of temperature.

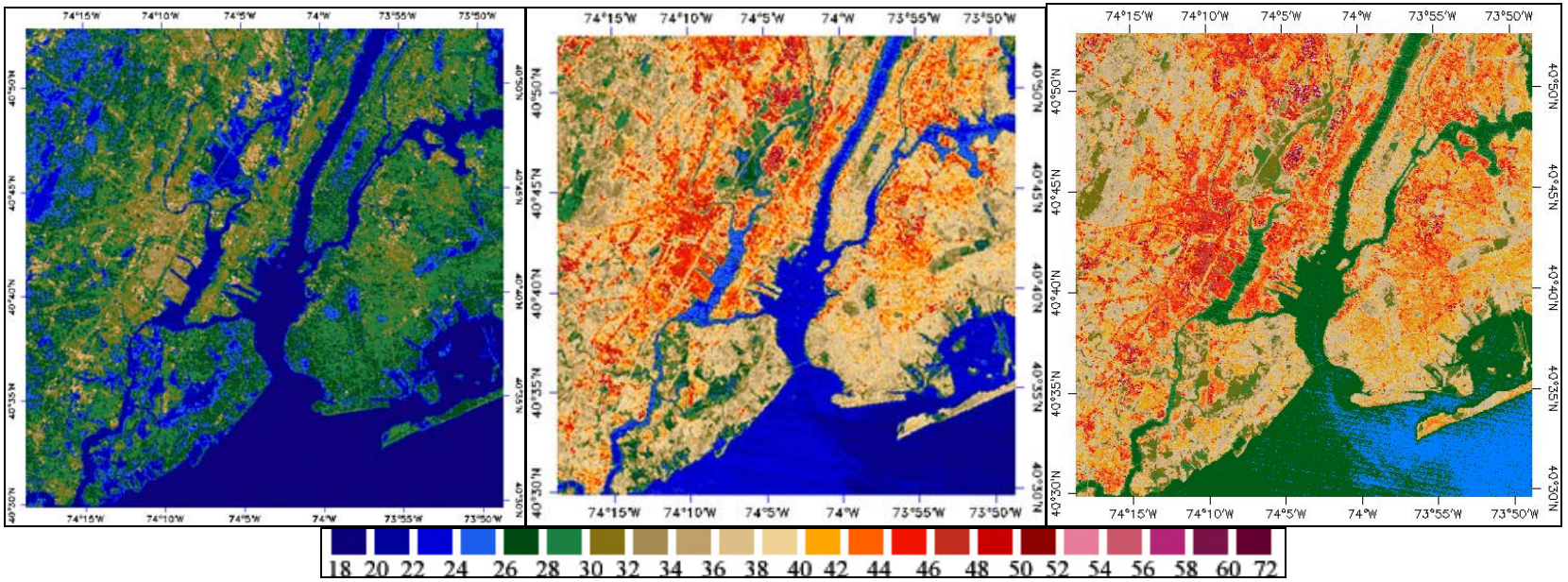

Figure 5.1. Comparison of surface temperature maps generated by (A) ETM+ surface temperature with a unity emissivity, (B) ASTER LST, and (C) ETM+ surface temperature with an emissivity 0.9 applied for the total study area. Both ETM+ and ASTER images were acquired in September 8, 2002.

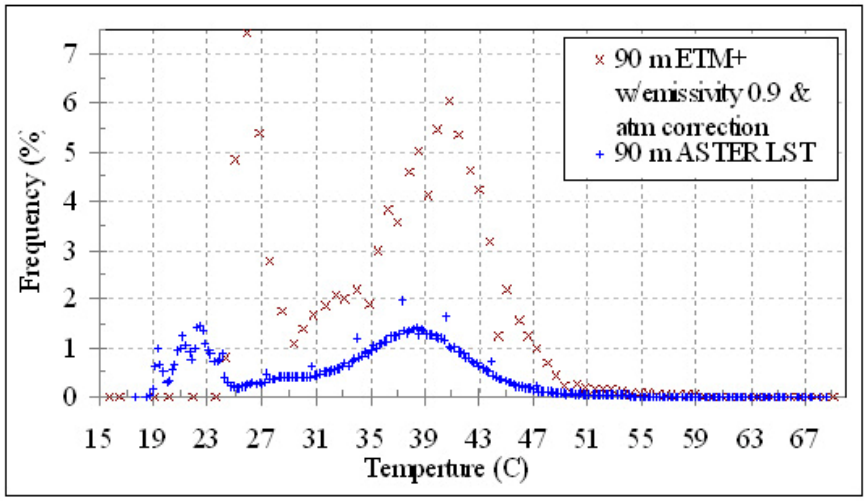

Figure 5.2. Comparison of frequency distributions between ASTER LST and ETM+ surface temperature with emissivity 0.9 and atmospheric correction.

The scatter diagram analysis of ETM+ surface temperature distribution applied with an emissivity 0.9 and the atmospheric correction in x-axis and the ASTER LST in y-axis for land surfaces over the study area shows a 0.76 of their correlation (Figure 5.3).

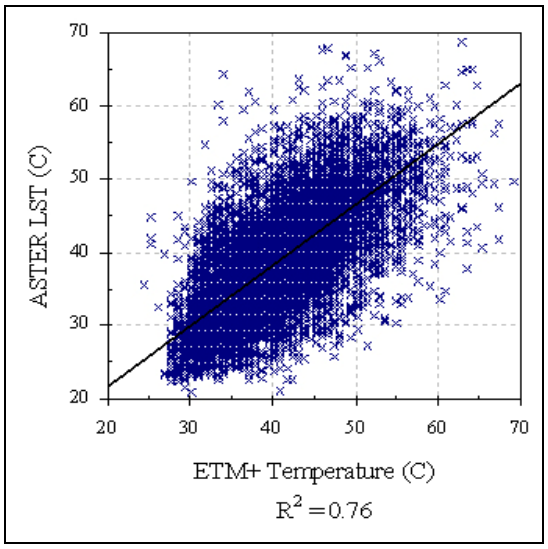

Figure 5.3. The scatter diagram distribution and its correlation between the ETM+ surface temperatures (applied with an emissivity 0.9 and the atmospheric correction) and ASTER LST surface temperature.

The generation of ETM+ surface temperature maps, based the classified emissivities and atmospheric corrections was carried out. The ETM+ image surface temperature maps based on various combinations of emissivity collection sets and the atmospheric correction parameter sets, shown in Figure 5.4, were cross examined with the ASTER LST map by correlation analyses from the twelve selected sites (each 3 x 3 km) as shown in Figure 5.5.

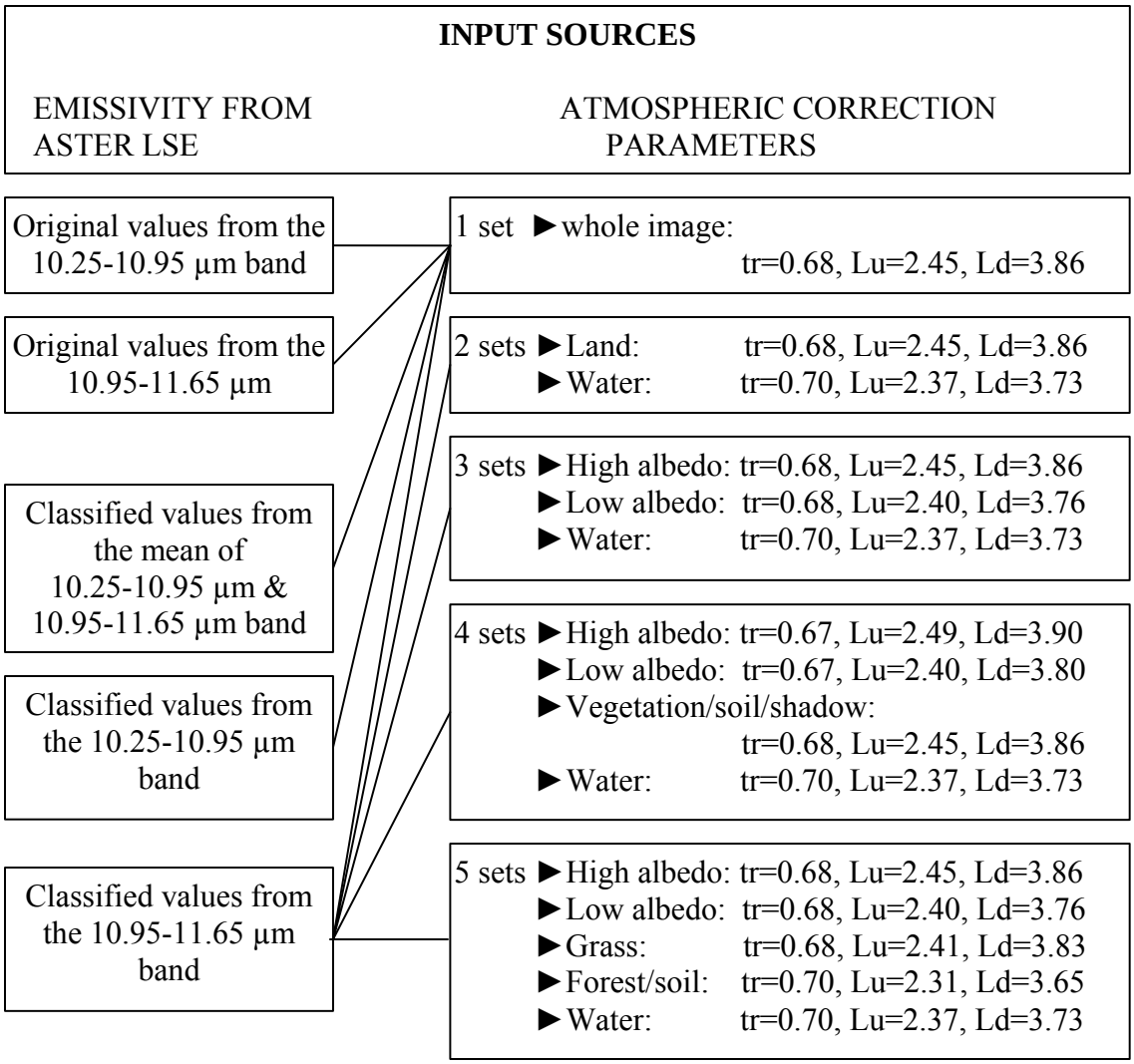

Figure 5.4. Different combinations of input sources applied for the emissivities and atmospheric correction parameters to process conversion of the ETM+ sensor measured radiances to surface leaving radiances.

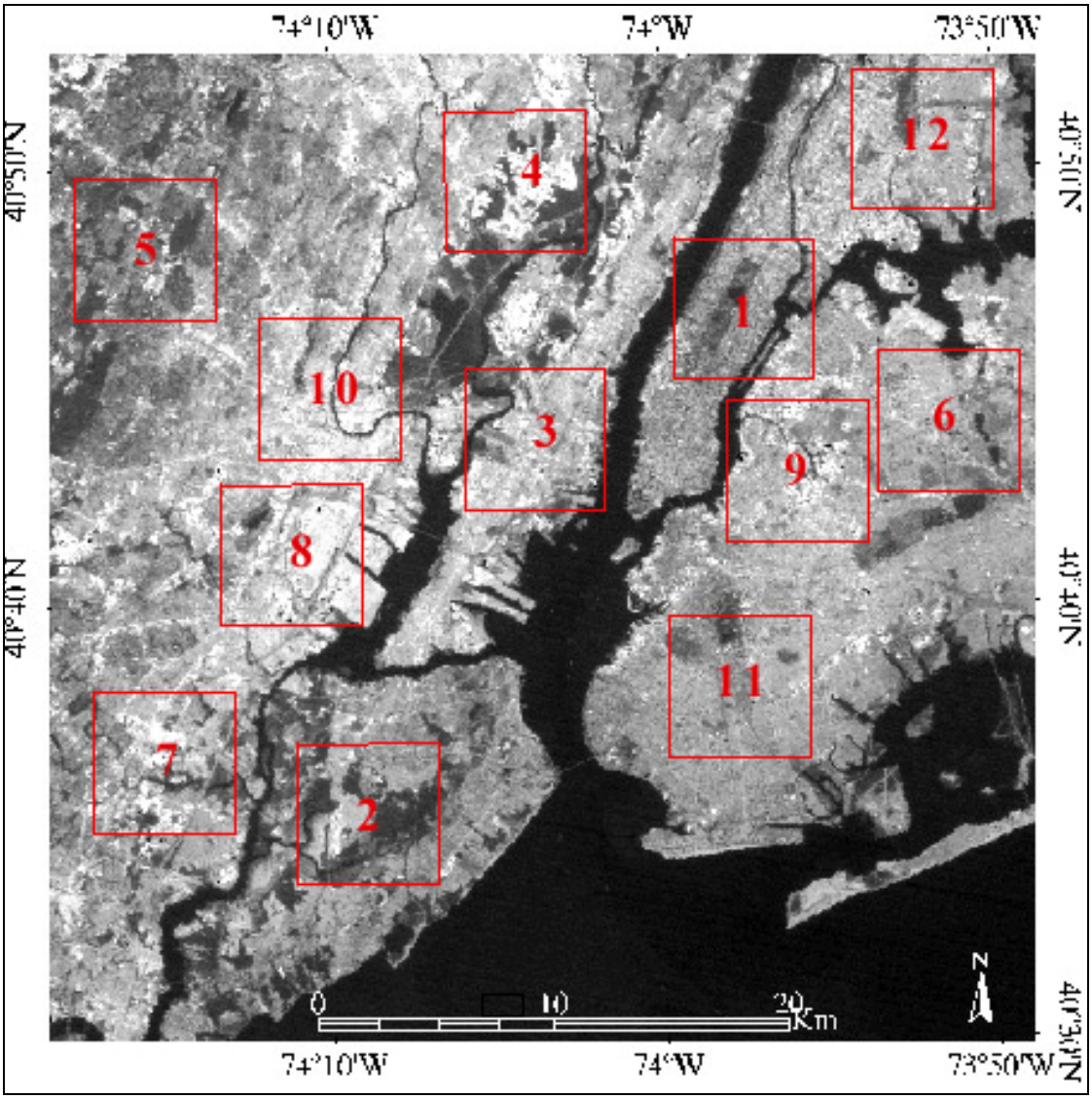

Figure 5.5. The 12 selected sites (red boxes with the size 3 km x 3 km) used for correlation analyses between the surface temperature derived from ETM+ and the ASTER LST.

The correlation for each site was derived from a scatter diagram that depicts a pixel-by-pixel comparison between the surface temperature retrieved from ETM+ thermal radiance measurements and the ASTER LSTs. Four scatter diagrams derived by overlaying the ETM+ surface temperature map generated from the classified emissivity

from ASTER band 14 and five different sets of atmospheric correction parameters with the ASTER LST are shown in Figure 5.6.

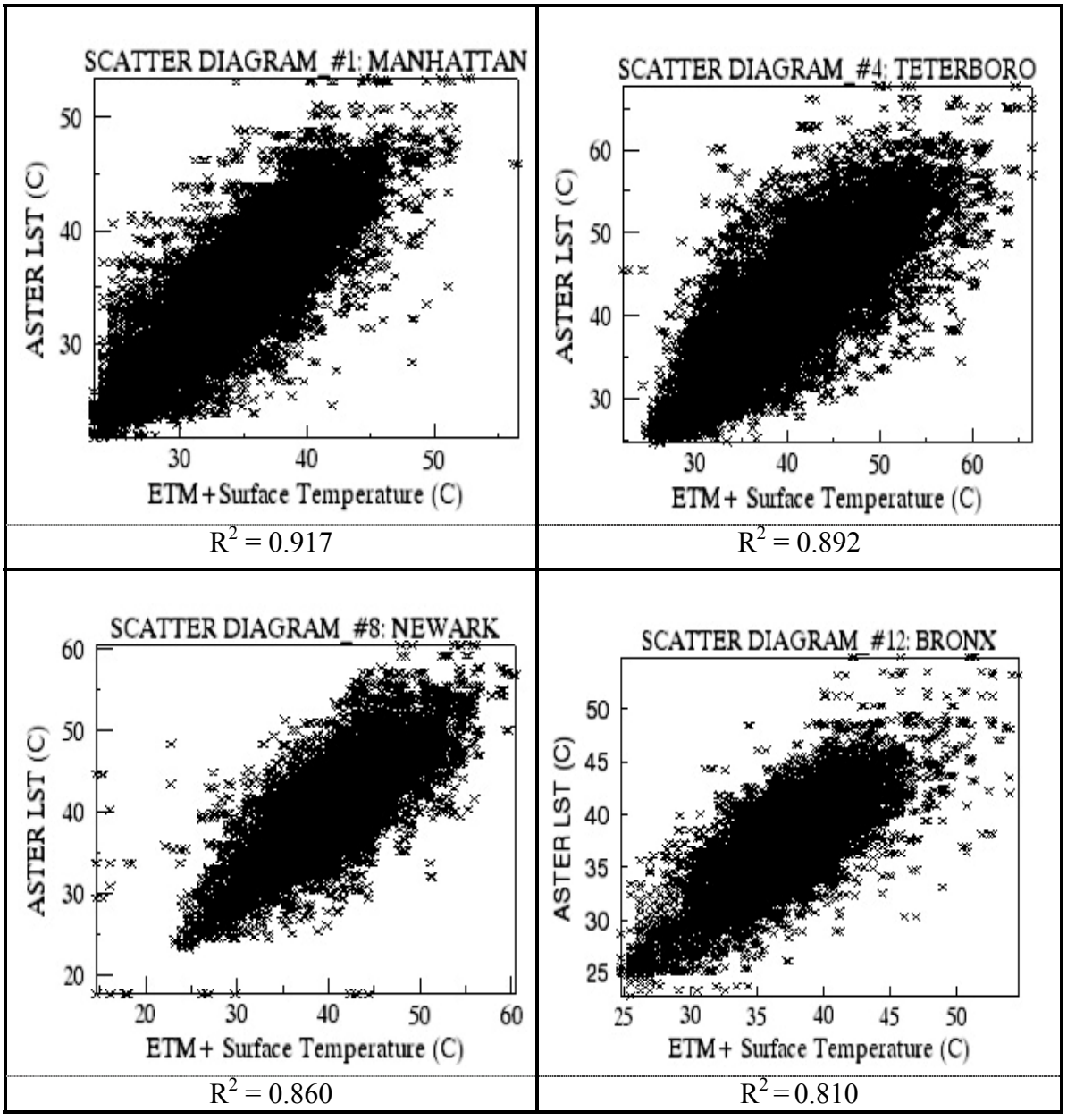

$R^2 = 0.917$ $R^2 = 0.892$

$R^2 = 0.860$ $R^2 = 0.810$

Figure 5.6. Scatter diagrams and correlation coefficients of four representative sites: The site #1 Manhattan in the upper left, the site #4 Teterboro in the upper right, the site #8 Newark in the lower left, and the site #12 Bronx in the lower right.

The highest correlation was observed in the scatter diagram #1 Manhattan with the R^2 of 0.917. The lowest correlation was by the site #12 Bronx with the R^2 of 0.810. The site #4 Teterboro showed the R^2 of 0.892, and the site # 8 Newark was the R^2 of 0.860.

The average temperatures estimated for the whole study area based on a detailed correlation analysis with five different input sources for estimating surface emissivities and five different application sets for the atmospheric correction parameters are presented in Table 5.1.

The correlation analysis shows that the result from the application of the original emissivity based on the ASTER LSE 10.95-11.65 μm band source with a single set of atmospheric corrections has the highest R^2 0.866. However, its average surface temperature estimated by this approach is 0.37 ºC lower than the mean surface temperature of ASTER measurements. This indicates that using a single set of the atmospheric correction parameters for the whole scene is not an appropriate approach to achieve accurate surface temperature.

The results derived from the application of original emissivities from the 10.25-10.95 μm band and the 10.95-11.65 μm band, indicate that using the original emissivity from the 10.95-11.65 μm band provides superior correlations as well as average surface temperature estimation than the emissivity derived with the 10.25-10.95 μm band. In general, using the emissivity from the10.25-10.95 μm band, either original or classified, results in lower surface temperatures than the ASTER surface temperatures. The test result of using the average emissivity from 10.25-10.95 μm and 10.95-11.65 μm bands also shows lower surface temperatures.

Table 5.1. Summary of the correlations in 12 selected sites and the average surface temperatures of whole study area based on different combination of emissivity source and atmospheric corrections.

Site		Different Numbers of the Atmospheric Correction Parameter Set								
		1 set					2 sets	3 sets	4 sets	5 sets
		Original Emissivity		Classified Emissivity			Classified Emissivity			
#	Description	10.25-10.95 μm	10.95-11.65 μm	10.25-10.95 μm	10.95-11.65 μm	Mean of 10.25-10.95 & 10.95-11.65 μm	10.95-11.65 μm			
1	Manhattan	0.9131	0.9150	0.9148	0.9150	0.9149	0.9172	0.9172	0.9181	0.9172
2	Staten Island	0.9140	0.9142	0.9109	0.9110	0.9109	0.9108	0.9103	0.9071	0.9107
3	Jersey city	0.9032	0.9026	0.9026	0.9028	0.9027	0.9050	0.9053	0.9056	0.9047
4	Teterboro	0.8929	0.8903	0.8911	0.8913	0.8912	0.8917	0.8916	0.8919	0.8916
5	West Orange	0.8718	0.8704	0.8643	0.8645	0.8644	0.8645	0.8649	0.8631	0.8645
6	Queens	0.8597	0.8606	0.8531	0.8537	0.8534	0.8538	0.8534	0.8508	0.8529
7	Linden	0.8575	0.8586	0.8533	0.8536	0.8534	0.8550	0.8555	0.8543	0.8544
8	Newark	0.8624	0.8578	0.8488	0.8491	0.8489	0.8504	0.8499	0.8480	0.8491
9	Maspeth	0.8411	0.8423	0.8417	0.8423	0.8419	0.8467	0.8457	0.8488	0.8459
10	East Orange	0.8410	0.8372	0.8361	0.8365	0.8363	0.8366	0.8365	0.8364	0.8359
11	Kings	0.8232	0.8259	0.8212	0.8221	0.8217	0.8228	0.8213	0.8284	0.8222
12	Bronx	0.8095	0.8167	0.8097	0.8107	0.8102	0.8107	0.8117	0.8165	0.8096
Correlation (R^2)		0.8658	0.8660	0.8623	0.8627	0.8625	0.8638	0.8636	0.8641	0.8632
Mean T. (ºC)		33.29	33.65	33.44	33.65	33.53	33.42	33.58	34.18	33.94
T (ºC). difference from the mean ASTER LST (34.01 ºC)		0.73	0.37	0.58	0.36	0.48	0.59	0.43	0.17	0.07

Further examinations applied the classified emissivities from the 10.95-11.65 μm band with the three different input sources for atmospheric corrections:

A High albedo surface,

B Low albedo surface, and

C. Water body.

In addition, four differentiated atmospheric corrections for high albedo, low albedo, vegetation/shadow/soil, and water surfaces were applied. The other is five differentiated ones as high albedo, low albedo, forest, grass, and water body. These three tests show that differences of their correlations are marginal with 0.001 based on the averages from 12 selected sites. However, their estimated average surface temperatures compared to the average temperature from ASTER are much larger deviation.

The average surface temperature estimated by the application of five differentiated atmospheric correction parameter sets for surfaces (Figure 5.7) shows much close to the ASTER surface temperature with 0.07 degree error. The correlation between ETM+ surface temperature and the ASTER measured LSTs for the whole study area is shown as a scatter diagram in Figure 5.8 with R^2 0.96.

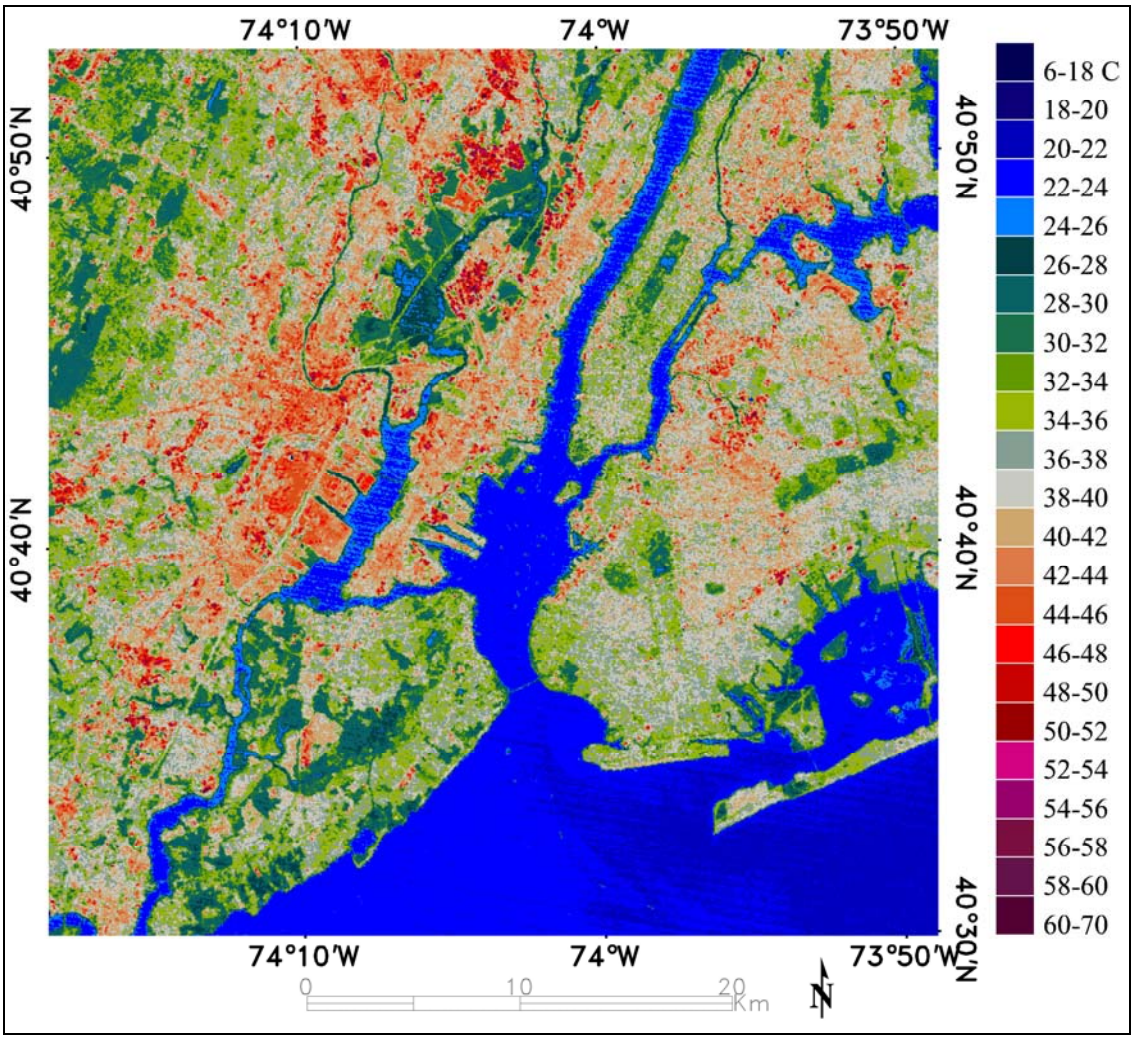

Figure 5.7. A 15 m ETM+ surface temperature map generated using classified emissivity from the ASTER band 10.95-11.65 μm and five different sets of the atmospheric correction parameters.

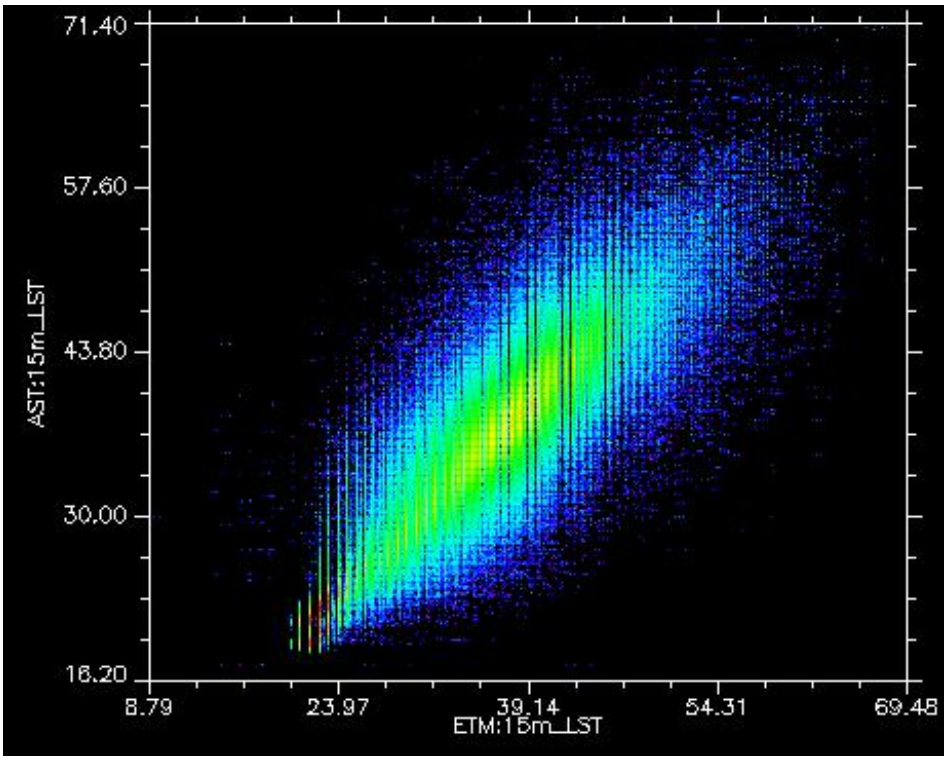

Figure 5.8. The scatter diagram distribution of 15 m pixel resolution ETM + surface temperature (x-axis) and ASTER LSTs (y-axis).

The final surface temperature maps generated from ETM+ and ASTER data were compared and further evaluated against ground truth data. As no *in situ* radiometric data of land surfaces were available during the satellite over-flight, coastal buoy SST measurements were used to compare *in-situ* temperature with the derived SST from ETM+ and ASTER. Considering the varying accuracy of radiance measurement by different satellite sensors, it was anticipated that errors could be better assessed over homogeneous surfaces like ocean water.

Among the four ground stations providing SST data in New York and New Jersey areas, only the Battery station, NY (Lat 40.70N, Lon 74.02 W) is within the study area.

Therefore, an extended analysis included three other ground measurement stations that were located within the coverage of the satellite images of ETM+ and ASTER LST.

The evaluation of ETM+ and ASTER surface temperature data, generated with the above classified emissivity method using atmospheric corrections, is based on ground truth SST measurement and is summarized in Table 5.2. Table 5.2 shows that both satellite derived SSTs appear to be slightly higher than the coastal buoy SSTs. One error introduced by the SST can be explained by the fact that satellite derived SST originates from the radiance emission of the skin temperature of the upper layer close to 0.1 mm. On the other hand, the sea water temperature measured by the Coastal-Marine Automated Network (C-MAN) and the National Ocean Service (NOS) stations is representing the bulk temperature at a depth of about 1 m from the air/sea interface. Kawai and Kawamura (1997) showed that satellite-derived sea surface temperature is higher compared to the *in situ* sea surface temperature by more than 1 ºC in summer but lower by more than 1 ºC in winter. These deviations can be explained by the combined effect of skin and diurnal temperature change in the upper meters.

The temperature differences between satellite observed SSTs and ground station measurement of SSTs show an average of 0.4 ºC by the ETM+, and an average of 0.6 ºC by the ASTER LSTs. The F values of regression analysis for both satellite estimations show smaller than the critical value of 18.51 at 95% confidence interval with the degrees of freedom at one and two. Therefore, both satellite measured surface temperatures are acceptable at the 95% confidence interval. Thus, the technique derived in this study is accurate in producing SST values with 0.4 to 0.6C.

Table 5.2. Comparison of SST derived from ASTER and ETM+: Sea water temperatures are from the Coastal-Marine Automated Network (C-MAN) and the National Ocean Service (NOS, NOAA). The acquisition date and time for all data was September 8, 2002, 10AM.

STATION	LAT (N)	LON (W)	GROUND DATA	ETM+	ASTER
			Water T (°C)	Surface T (°C)	Surface T (°C)
The Battery, NY[1]	40.70	74.02	22.5	22.3	22.8
Sandy Hook, NJ[1]	40.47	74.01	22.3	22.8	23.5
Kings Point, NY[1]	40.81	73.78	22.0	22.8	22.4
Ambrose Light, NY[2]	40.46	73.83	21.1	21.2	21.4
MEAN of temperature differences by Ground measurement T minus Satellite LSTs				0.4	0.6
SSR (Sum of Squares of Regression)[*a]				0.7578	0.9018
SSE (Sum of Squares of Error)[*b]				0.3897	0.2457
MSR (Mean Square of Regression)[*c]				0.7578	0.9018
MSE (Mean Square of Error)[*d]				0.1949	0.1229
F Ratio [*e]				3.89	7.34

a: SSR = $\sum$(the variation of the fitted values – the mean)^2

b: SSE = $\sum$(the variation of the observations – the variation of the fitted values)^2

c: MSR = SSR / the degree of freedom for the regression

d: MSE = SSE / the degree of freedom for the error

e: F = MSR / MSE

6. Conclusions

The main objectives of this study were to identify precise emissivity for urban surface covers, and enhance spatial details of urban surface temperature. From the research undertaken to meet the objective the following will summarize the major results.

The findings from the first investigation are:

Accurate surface classification for asphalt pavement, cement pavement, tar pavement, color painted metal roof, grasslands, forested parks, bare soil, etc. is one of the critical factors to derive emissivity values for precise temperature measurements from space. To overcome limited input band numbers from the ETM+ original data source, twelve additional input bands generated through band rationing, were efficient to enhance maximum likelihood classification result by 0.84% of overall accuracy and 0.05 of the Kappa coefficient. Adding three primary principal component bands also contributes an improvement of classification accuracy by 0.05 level in the Kappa coefficient.

An examination of maximum likelihood classification accuracy for vegetation coverage was accomplished by the Scaled Difference Vegetation Index method. Unlike the commonly used the Normalized Difference of Vegetation Index overestimation, especially over the interspersed non-park vegetation with uncertainties of quantities in the Normalized Difference of Vegetation Index measurement, Scaled Difference Vegetation Index provides highly accurate vegetation coverage within less than 0 to 0.4 % deviations. Therefore, using the Scaled Difference Vegetation Index is an effective way to achieve accurate estimation of urban vegetation coverage.

The emissivity values from ASTER land surface temperature band 13 or a unity 0.92 used for urban surface temperature mapping in previous studies appeared to be

either too high or too low than the actual emissivity values observed in our study area. Using land surface temperature band 13 of ASTER data generally results in too low urban surface temperatures. Our study shows that using band 14 of ASTER land surface temperature is more optimal.

In the application of the atmospheric correction parameters especially for classified emissivities of urban areas, a better approach is to apply at least four or above differentiated atmospheric correction sets. As appeared in our study, applying three differentiated sets such as high and low albedo surface, and water bodies do not provide optimal level of surface temperature data.

The cross examination of surface temperature and emissivity data from MODIS, ASTER, and Landsat ETM+ shows that the surface temperature of MODIS measurement is 1.3–1.7 ºC lower than the ASTER and ETM+ surface temperatures. This result is based on MODIS data that applied an emissivity of approximately 0.05 higher than the average emissivity of land surfaces that were estimated from ASTER.

This study shows that it is feasible to map surface temperature with a 15 m pixel resolution using 60 m ETM+ thermal radiance measurement with the accuracy up to 96%. Consequently, it is possible to identify surfaces or objects, which contribute critical temperatures above 40 ºC that occurred in 25% of our study area.

Fused images, by merging a high resolution of the QuickBird panchromatic band and its multi-spectral bands through the Principal Component Sharpening and Gram-Schmidt sharpening, were superior to other fusion methods in the conservation of the original data properties as well as in the enhancement of visualization on a ground survey role. Moreover, adding the principal components resulted in the fusion of Landsat 7

Enhanced Thematic Mapper Plus (ETM+) reflectance bands with the ETM+ panchromatic band, is an efficient approach to achieve more accurate surface classification.

Among the various classifiers tested, the maximum likelihood method resulted in the highest overall accuracy, and the Kappa coefficient was superior over the classification results from the spectral angle mapper, decision tree, and neural network classifiers. However, the maximum likelihood classifier shows a tendency to undersample narrowly arranged objects that are most representative for urban impervious surfaces, but oversample about 0.6%-1% vegetation coverage. This may be explained by its generic character, which is based on the assumption of a normal distribution for each class in each band that is assigned to a specific class with the highest probability.

A modified spectral angle mapper used the ratio bands in addition to seven multispectral ETM+ bands and provided better classification for impervious surfaces. For the surface cover type identifications, the thermal radiance band as an input provided better identification through supervised classification with the maximum likelihood, spectral angle mapper, and decision tree classification. The estimated impervious surface in the study area was between 47% and 48% and had an average emissivity of 0.92.

The findings from the second investigation are:

Surface temperatures above 40 ºC in the study area were related to low –albedo surfaces included black tar resin mixture pave, black granule synthetic membrane, gray synthetic membrane, dark color painted metals and dark gray asphalt pavement. These surfaces were estimated to cover approximately 15% of the investigated area. Among these low-albedo surfaces that showed surface temperature above 40 ºC, were dark gray

asphalt pavements that had a coverage of 11%. This indicates that replacing the dark gray asphalt pave to light tone cement concrete asphalt pave can reduce the average temperature about 1.5 ºC. Among the high-albedo surfaces, cooling effects seemed to be more efficient where a considerable thickness of white coating applied on cement concrete surfaces or illuminate coating applied on synthetic membrane cover.

To accomplish a successful atmospheric correction for the ETM+ image processing, higher resolution of the atmospheric correction parameters need to be developed. However, currently available atmospheric correction parameters for the Landsat ETM+ data is based on the NECP data, which is processed with the input source of an atmospheric profile that covers 1º by 1º. Therefore, urban scale temperature derived through application of only one set of atmospheric correction parameters from the Atmospheric Correction Parameter Calculator results in the average surface temperature to be approximately 0.5 ºC lower than the average surface temperatures of ASTER measurements. It indicates that application of multi-sets of atmospheric correction parameters for a subset of a Landsat ETM+ image, which is usually less than a half size of the National Centers for Environmental Prediction input data dimension, is necessary. We tested with five different sets of atmospheric correction parameters for surface high-albedo, low albedo, forest/shadow/soil, grasslands, and water bodies. The result shows that the correlations with ASTER surface temperatures in the five classified surfaces are less than 0.7 R^2. These five classes included one extremely low-albedo black glossy tar pave, dark color painted metal surface, two high-albedo surfaces coated by different thickness, and shadow region. Considering the characteristic spatial layout of these surfaces, which are highly fractionized with much smaller than the pixel size, the

best atmospheric correction parameters for these specific surfaces remains a challenging issue. Since this study focused on accurate surface temperature retrieval from Landsat ETM+ data by applying the classified emissivity method and atmospheric corrections with the emissivity classified surfaces in two separated processes, future development of processing has to deal with both tasks at the same time.

This study established a semi-automatic technique to retrieve 15 m pixel resolution surface temperature from the 60 m spatial resolution Landsat ETM+ sensor measurement. This technique includes increase of image pixel resolution through image fusion, improve surface classification through an increased number of input sources, extraction of emissivity values from synoptic ASTER land surface emissivity band 14 image, emissivity classification, and apply different level of atmospheric corrections. Therefore, the techniques developed in this study will serve to generate extensive surface temperature database from the Landsat satellites, which generated the longest period of image archives, and these expected data, can contribute for better improvement of urban climate modeling as well as global scale climate modeling.

Appendices

Appendix 4.3.

To generate top-of-atmosphere (TOA) band-averaged spectral radiance (W m^{-2} μm^{-1} sr^{-1}) from 16-bit integers, the conversion to band-integrated radiance used the following equation:

$$L_{pixel,\ band} = absCalFactor_{\ band} * q_{\ pixel,\ band}$$

where $L_{pixel,\ band}$ are TOA band-integrated radiance image pixels (W m^{-2} sr^{-1}), $absCalFactor_{\ band}$ is the absolute radiometric calibration factor (W m^{-2} sr^{-1} $count^{-1}$) for a given band, and $q_{\ pixel,\ band}$ are radiometrically corrected image pixels (counts). The second step was to divide the band-integrated radiance by an effective bandwidth ($\Delta\lambda$). The effective bandwidth for QuickBird panchromatic band is 0.398 μm, and the equation applied for this conversion was

$$L_{\lambda\ pixel,band} = \frac{L_{pixel,band}}{\Delta\lambda_{band}}$$

where $L_{\lambda pixel,band}$ are TOA band-integrated spectral radiance image pixels (W m^{-2} sr^{-1} μm^{-1}), $L_{pixel,band}$ are TOA band-integrated radiance image pixels (W m^{-2} sr^{-1}), and $\Delta\lambda_{band}$ is the effective bandwidth for a given band (DigitalGlobe, 2007).

Appendix Figure 4.3.1. A, B, C, & D

A. Vegetated park	B. Railroad yard
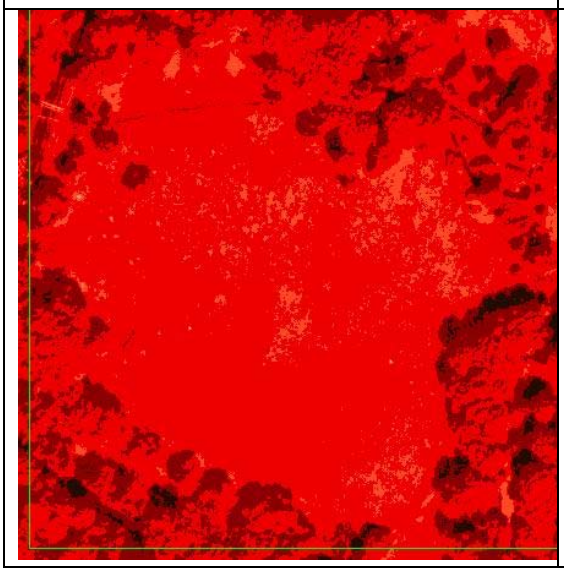	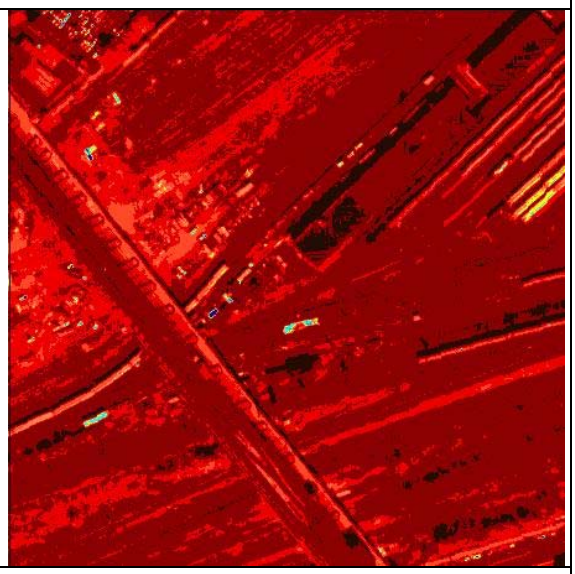
C. Single-story housing area	**D. Industrial zone**
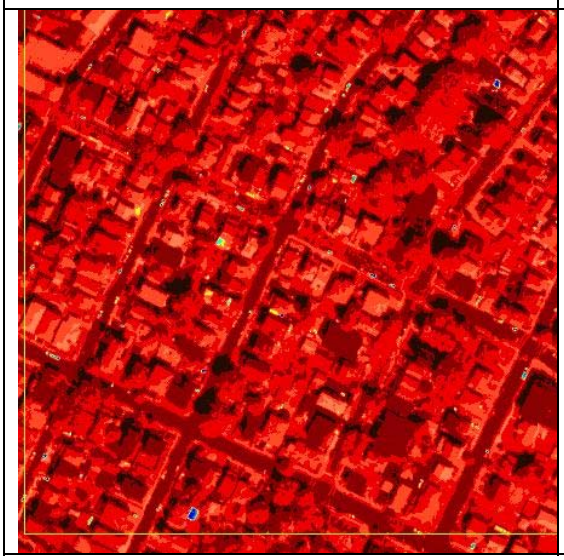	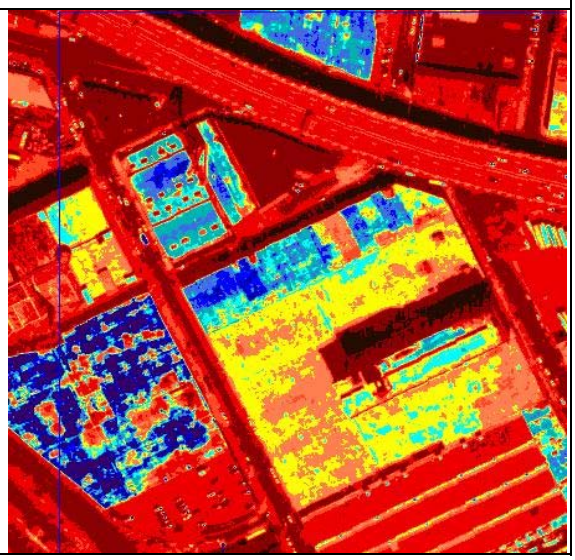

Appendix Table 4.3.2. Ground survey sites and their geo-positions as latitude and longitude.

#	Site	Latitude (N)	Longitude (W)	Surface Types	Surface roughness
1	7th Regiment Armory (66th-67th St, Lexington Ave)	40° 45.994’	73° 57.898’	White emulsion coated	smooth
2	Armory (25th, Park Ave)	40° 44.417’	73° 58.939’	Gray color coating layer	smooth
3	Baruch College	40° 44.483’	73° 59.014’	Aluminum metal/Glass	smooth
4	COSTCO 10th St, Vernon Blvd	40° 46.014’	73° 56.320’	Ivory color painting on metal	smooth
5	UN International School	40° 44.193’	73° 58.468’	White/Green synthetic material	Smooth
6	Javits Convention Center- pavilion	40° 45.535’	74 00.038’	Ivory color polysynthetic layer	smooth
7	White aluminum coating	40° 45.359	73° 55.810’	White laminate coating	smooth
8	Bellevue Hospital – east bld	40° 44.228’	73° 58.487’	Light brown stones chips	rough
9	Bright brown cement granule	40° 45.421’	73° 55.755’	Bright brown cement	rough
11	Public Parking Terrace 28th St QueensPlaza	40° 44.953’	73° 56.309’	Light gray paint on concrete	smooth
12	Hunter North	40° 46.122’	73° 57.910’	Gravels	rough
13	Dark brown black Tar layer	40° 45.359’	73° 55.810’	Tar membrane (dark brown black)	smooth
14	22-23 St, Queens Plaza-south bld	40° 45.097	73° 56.507	Black tar	rough
17	Columbus Circle	40° 46.091’	73° 58.865’	Gray concrete brick	rough
18	Plaza cross the Javits Center	40° 45.394’	74° 00.060’	Red brick paved	rough
19	Javits Center W37th-38th, 11th Ave	40° 45.462’	74° 00.050’	light /dark painting on concrete,	Smooth

Appendix 4.4

Spectral Angle Mapper (SAM)

The classifier SAM was originally developed for hyperspectral image data analysis. Therefore, it worked better when this classification was carried out with all reflectance bands including a thermal band of ETM+. The spectral angle mapper uses an n-dimensional angle to match pixels to reference spectra. The algorithm determines the spectral similarity between two spectra by calculating the angle between the spectra, treating them as vectors in a space with dimensionality equal to the number of bands. Endmember spectra used by SAM extracted directly from the image as region of interest average spectra. SAM compares the angle between the endmember spectrum vector and each pixel vector in n-dimensional space. Smaller angles represent closer matches to the reference spectrum (ENVI 2005). The classification result was much influenced by threshold radian applied.

Decision Tree Classifier

In decision tree classification, it was critical to having knowledge about the statistics for each band in each cluster. It became very complicated when the number of clusters or region of interests increased. Because of this complication, there was much error involved with the threshold values that decided and applied. This procedure was also great time demanding process. The diagram used for the decision tree is shown below:

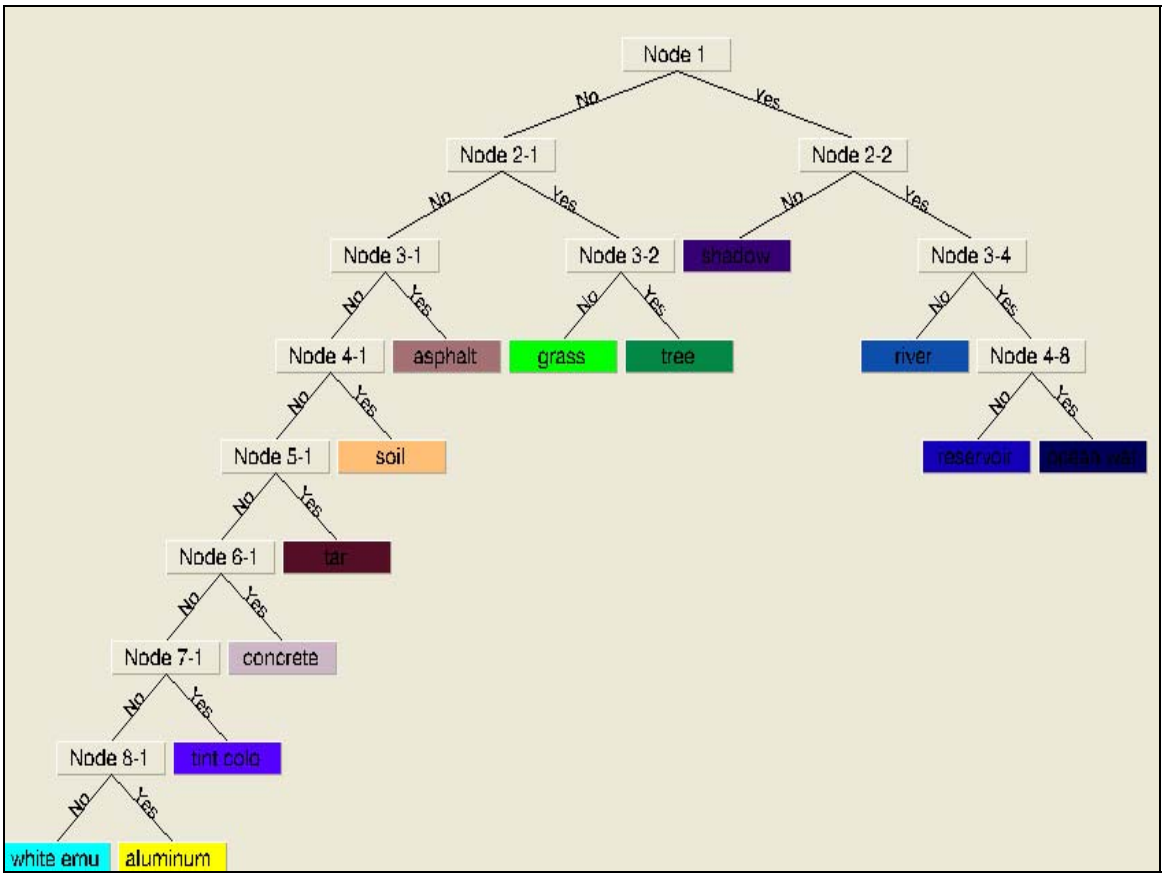

Neural Network

The neural network technique was also tested because it is known to be especially good for non-linear classification. Since this technique uses standard back propagation for supervised learning, it was very sensitive to applied regions of interest, and input bands. In case of ETM+ image classification, using only reflectance bands showed better classification than using all including thermal band. Also choosing optimal level of iteration was important to get good result. In this image processing, optimal iteration was between 1000 and 1500. Overall neural network classification accuracy compare to other classifications was relatively high and also very time efficient process.

Appendix Table 4.4.1. Surface class distributions by four different classifications.

CLASSIFIER	ETM+ image with 28.5 m pixel resolution				
	ML (%)	SAM (%)	DT(%)	NN (%)	
CLASSES	13 ROIs	13 ROIs	13 ROIs	13 ROIs	11 ROIs
Concrete pave	17.19	17.59	14.82	6.56	23.41
Asphalt pave	3.40	17.39	18.57	0.00	10.84
Tar pave	2.63	3.71	5.02	10.72	5.03
Tint colored concrete	2.50	0.37	2.81	1.52	1.88
White aluminum coated concrete	4.01	1.58	2.62	16.47	2.89
White emulsion smooth /metal	3.58	0.20	0.91	0.39	0.39
Tree	29.37	28.09	23.29	0.33	22.68
Grass	10.13	5.35	5.71	39.86	7.06
Soil/sand	1.96	0.36	1.17	0.76	0.66
Shadow	7.52	2.00	3.11	0.05	0.39
Open sea	11.84	9.36	7.92	0.00	
River/stream	5.54	5.74	7.07	22.68	
Lake/reservoir	0.32	8.28	6.99	0.67	

Appendix Figure 4.4.1. Classification Maps by maximum likelihood classifier, spectral angle mapper, decision tree classifier, and neural network.

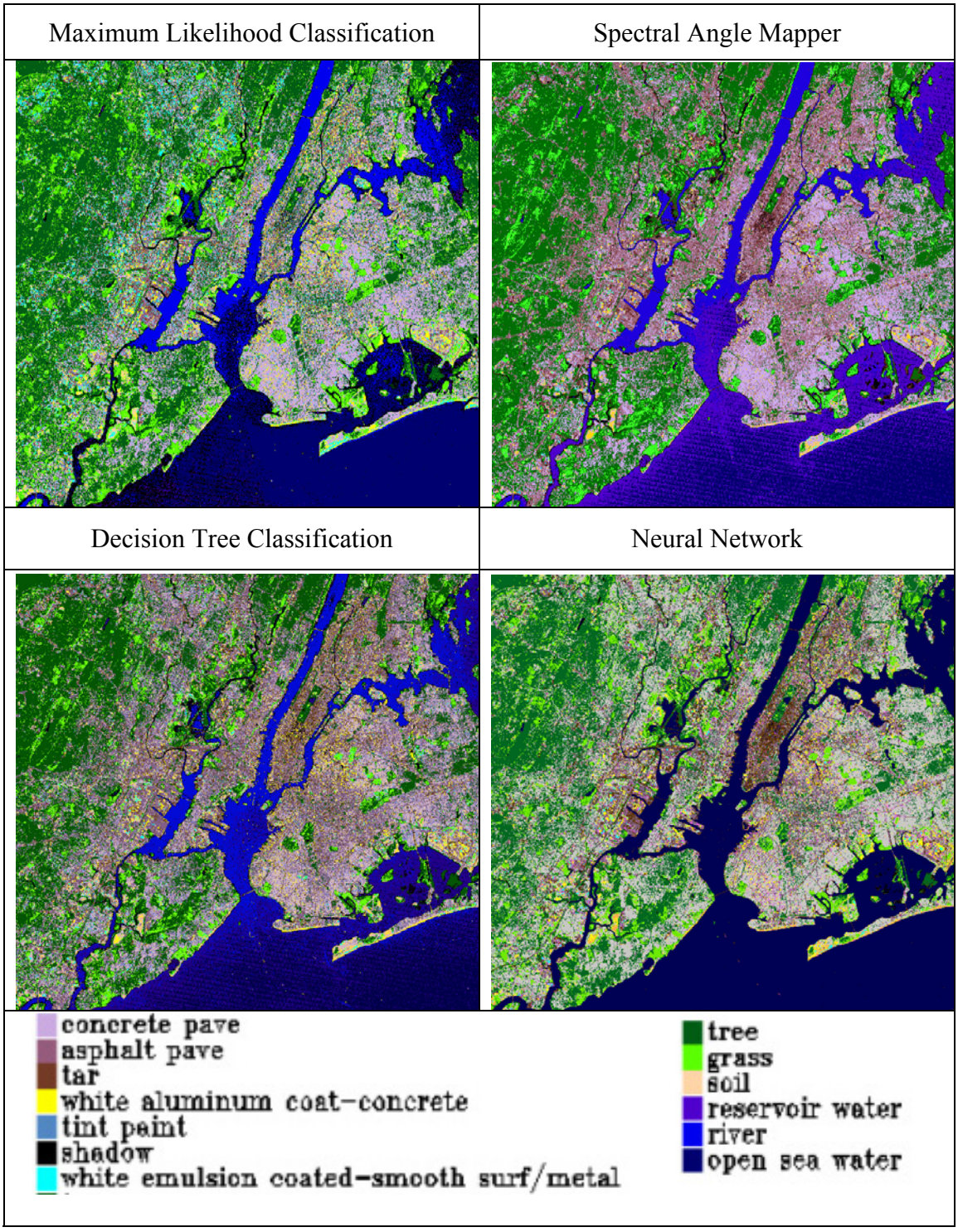

Appendix Figure 4.4.2.

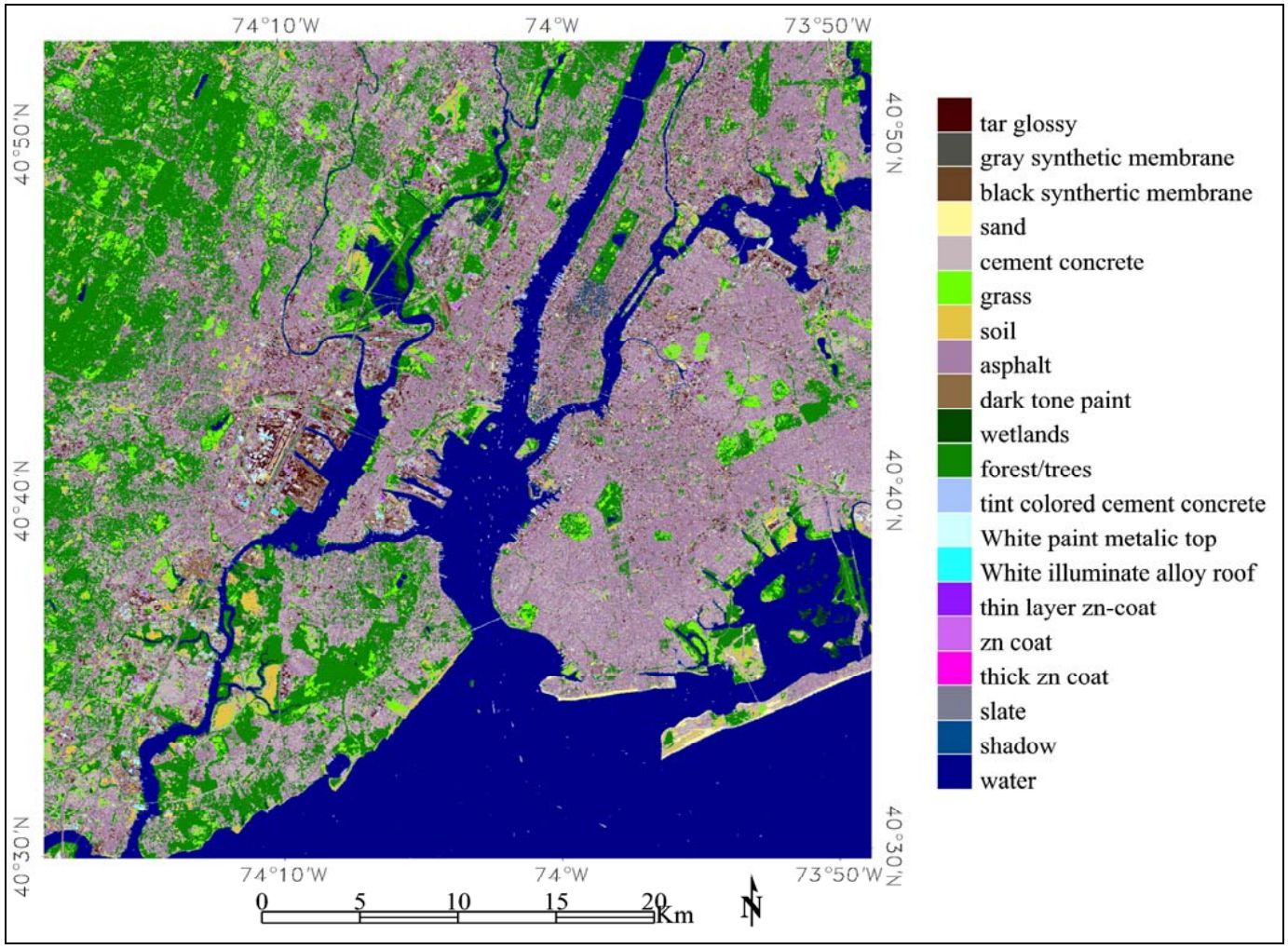

Figure 4.4.2. The ML classification result of the 15 m ETM+ image based on twenty training sites and used twenty two input bands.

Appendix Table 4.4.2. The ML classification results of 15 m resolution ETM+ and ASTER image with 20 selected training sites.

ML-CLASS	COVERAGE (%)	
	15 M ETM+	**15M ASTER**
Black glossy tar pavement	1.07	0.95
Gray synthetic membrane roof	0.77	0.37
Black granule sheet roof	0.68	0.22
Asphalt pavement	23.48	19.10
Lighter color cement (concrete pave)	17.34	21.37
Tint colored concrete roofs	0.69	0.38
White paint roof	0.59	1.34
White emulsion coating roof	0.09	0.12
Colored metal container	2.35	2.19
zinc coating roof (thick)	0.09	0.21
Silver coating roof (thin)	0.12	0.03
Metal roof, corroded	0.06	0.19
Gray slate roof	0.33	0.10
Shadow	1.14	0.59
Soil	2.28	2.71
Sand	0.23	0.10
Grass	4.03	4.48
Tree	19.93	19.99
Wetland	0.63	0.89
Water	24.10	24.70

Appendix Table 4.5.1 The emissivity of common urban surface cover types at 8-14 μm, reflectance at VNIR (0.4-0.9 μm), and air temperature rise.

Materials	Mean Emissivity at 8-14 μm	Reflectance at 0.4-0.9 μm	Air Temperature rise (°C)
White synthetic membrane*[1]	0.87	0.69	13.9
Aluminum coating-metal*[1]	0.25	0.61	26.7
Gray synthetic rubber membrane*[1]	0.87	0.23	37.8
White pigment coating*[1]	0.91	0.80	7.8
Paints: Red. Green /White/Black	0.95/0.94/0.92		
Camouflage green	0.85		
Glass	0.81-0.77		
Asphalt concrete	0.97-0.94		
Asphalt tar paper	0.93		
Slate	0.67–0.80		
Cement concrete (rough)	0.94		
Concrete tiles	0.63-0.62		
Gravels : White color*[1]	0.90	0.65	15.6
Light tone*[1]	0.90	0.34	31.7
Dark tone*[1]	0.90	0.12	42.2
Red brick (rough)	0.93		
Gray brick	0.75		
Metal, White coats on	0.85		
Galvanized steel, tin	0.04		
Water	0.989		
Broadleaf vegetation/Grasses	0.989		
Shrubs	0.975		
Organic soil	0.980		
Dry mineral soil	0.969		
Sand	0.760		

*[1] Source information from Lawrence Berkeley National Laboratory (LBNL) at http://eetd.lbl.gov/CoolRoofs.
The others from the Sierra Pacific Innovations (SPI) emissivity data at http://www.x20.org/library/thermal/emissivity.htm and Cole-Parmer technical library at http://www/coleparmer.com/techinfo/print.asp?htmlfile=Emissivity.htm.

Appendix Table 4.7. Full Width at Half Maximum (FWHM) for MODIS, ASTER and ETM+ sensors and their spatial resolution.

MODIS				ASTER				ETM+			
Spatial Resolution and FWHM (μm)			Band	Spatial Resolution and FWHM (μm)			Band	Spatial Resolution and FWHM(μm)			Band
250 x 250 m	500 x 500 m	1 x 1 km		15 x 15 m	30 x 30 m	90 x 90 m		15 x 15 m	30 x 30 m	60 x 60 m	
		0.405-0.420	8								
		0.438-0.448	9								
	0.459-0.479		3						0.450-0.515		1
		0.483-0.493	10								
		0.526-0.536	11	0.520-0.600			1		0.525-0.605		2
	0.545-0.565	0.546-0.556	12					0.520-0.900			Pan
			4								
0.620-0.670			1	0.630-0.690			2		0.630-0.690		3
		0.662-0.672	13								
		0.673-0.683	14								
		0.743-0.753	15						0.750-0.900		4
0.841-0.876			2	0.780 -0.860			3				
		0.862-0.877	16								
		0.890-0.920	17								
		0.931-0.941	18								
		0.915-0.965	19								
	1.230-1.250		5								
		1.360-1.390	26		1.600 – 1.700		4		1.550-1.750		5
	1.628-1.652		6		2.145 – 2.185		5		2.080-2.350		7
	2.105-2.155		7		2.185 – 2.225		6				
		3.600-3.840	20		2.235 – 2.285		7				
		3.929-3.989	21		2.295 – 2.365		8				
		3.929-3.989	22		2.360 – 2.430		9				
		4.020-4.080	23								
		4.433-4.498	24								
		4.482-4.549	25								
		6.535-6.895	27								
		7.175-7.475	28			8.125 – 8.475	10				
		8.400-8.700	29			8.475 – 8.825	11				
		9.580-9.880	30			8.925 – 9.275	12				
		10.780-11.280	31			10.250-10.950	13			10.40-12.50	
		11.770-12.270	32			10.950-11.650	14				

Appendix Table 4.7.1. Summary of MODIS surface temperature distributions in five counties of New York City and part of six counties in northeastern New Jersey.

County	Average Temperature (°C)	Area coverage above 36 °C (%/total land surface)
Brooklyn	33.6	3.1
Queens	33.6	2.7
Bronx	33.2	1.4
Manhattan	31.8	0.0
Staten Island	31.2	0.0
Sum of NYC	**33.0**	**7.3**
Passaic	35.8	2.2
Middlesex	35.6	0.5
Union	35.4	3.4
Bergen	34.8	4.3
Essex	34.2	5.1
Hudson	28.4	1.3
Sum of NJ	**34.0**	**16.8**

Appendix Table 4.7.3. Distributions (%) comparison between the average emissivities measured from 5 thermal bands and 2 thermal bands of ASTER data.

EMISSIVITY	DISTRIBUTION (%) from the average between **8.13 & 11.65 µm**	DISTRIBUTION (%) from the average between **10.25 & 11.65 µm**
Below 0.88	0.92	0.80
0.88-0.89	1.06	0.80
0.89-0.90	2.83	1.50
0.90-0.91	6.90	2.80
0.91-0.92	14.60	4.80
0.92-0.93	26.65	8.00
0.93-0.94	28.50	10.80
0.94-0.95	9.88	14.10
0.95-0.96	1.91	38.10
0.96-0.97	0.00	11.50
0.97-0.99	6.75	6.80

Bibliography

ABRAMS, M. J., HOOK, S., and ABRAMS, M. C., 2001, Imaging spectrometry in the thermal infrared. In *Imaging spectrometry,* F. D. van der Meer and S. M. de Jong (Eds), pp. 283-306 (Netherlands: Kluwer Academic Publishers).

ARTIS, D. A., and CARNAHAN, W. H., 1982, Survey of emissivity variability in thermography of urban areas. *Remote Sensing of Environment*, **12**, 313-329.

BARSI, J. A., SCHOTT, J.R., PALLUCONI, F. D., and HOOK, S. J., 2005, Validation of a web-based atmospheric correction tool for single thermal band instruments. In *Proceedings of SPIE,* vol.5882, pp. 58820E-1-58820E-7 (Bellingham: SPIE).

BECKER, F., and LI, Z. L., 1990b, Temperature-independent spectral indices in thermal infrared bands. *Remote Sensing of Environment*, **32**, 17-33.

BEN-DOR, E., 2001, Imaging spectrometry for urban applications. In *Imaging spectrometry,* F. D. van der Meer and S. M. de Jong (Eds), pp. 243-281 (Netherlands: Kluwer Academic Publishers).

BEN-DOR, E., and SAARONI, H., 1997, Airborne video thermal radiometry as a tool for monitoring microscale structures of the urban heat island. *International Journal of Remote Sensing*, **18**, 3039-3053.

CARNAHAN, W. H., and LARSON, R. C., 1990, An analysis of an urban heat sink. *Remote Sensing of Environment*, **33**, 65-71.

CHAVEZ, P. S., SIDES, S. C., and ANDERSON, J. A., 1991, Comparison of three different methods to merge multiresolution and multispectral data: TM & SPOT pan, *Photogrammetric Engineering and Remote Sensing*, **57**, 295-303.

CLARK, R. N., 1999, Spectroscopy of Rocks and Minerals, and Principles of Spectroscopy. In *Manual of Remote Sensing, volume 3, Remote Sensing for the Earth Sciences*, A.N. Rencz, (Ed.), pp. 3-58. (New York: John Wiley and Sons, Inc.).

CONGALTON, R. G., 1991, A review of assessing the accuracy of classifications of remotely sensed data. *Remote Sensing of Environment*, **37**, 35-46.

DASH, P., GOTTSCHE, R. M., OLESEN, F. S., and FISHER, H., 2002, Land surface temperature and emissivity estimation from passive sensor data: theory and practice-current trends. *International Journal of Remote Sensing*, **23**, 2563-2594.

DIGITAL GLOBE, 2007, Product guide. *QuickBird Imagery Products, Longmont, Colorado:DigitalGlobe,Inc*. Available at http://www.digitalglobe.com/downloads/QuickBird%20Imagery%20Products%20-%20Product%20Guide.pdf.

ENVI, 2005, ENVI user's guide version 4.2. *The Environment for Visualizing Images*, (Boulder, Colorado: Research Systems. Inc.).

FOODY, G.M., 1992. On the compensation for chance agreement in image classification accuracy assessment. *Photogrammetric Engineering and Remote Sensing*, **58**, 1459-1460.

GAFFIN, S., ROSENZWEIG, C., PARSHALL, L., EICHENBAUM-PIKSER, J., GREENBAUM, A., BLAKE, R., BEATTIE, D., and BERGHAGE, R., 2006, Quantifying evaporative cooling from green roofs and comparison to other land surfaces. *Presentation at Boston Green Roof Annual Conference, May 11, 2006, Boston, Massachusetts.*

GALLO, K. P., MCNAB, A. L., KARL, T. R., BROWN, J. F., HOOD, J. J., and TARPLEY, J. D., 1993, The use of a vegetation index for assessment of the urban heat island effect. *International Journal of Remote Sensing*, **14**, 2223-2230.

GILLESPIE, A. R., 1985, Lithologic mapping of silicate rocks using TIMS. *Proceedings TIMS Data User's Workshop* (Pasadena, CA: Jet Propulsion Laboratory), JPL Pub. **86-38**, pp. 29-44.

GILLESPIE, A. R., ROKUGAWA, S., MATSUNAGA, T., COTHERN, J. S., HOOK, S. J., and KAHLE, A. B., 1998, A temperature and emissivity separation algorithm for advanced spaceborne thermal emission and reflection radiometer (ASTER) images. *IEEE Transactions on Geoscience and Remote Sensing*, **36**, 1113-1126.

GLOBAL RURAL-URBAN MAPPING PROJECT, 2005, Urban extents. Center for International Earth Science Information Network, Columbia University, Palisades, New York. Available at http://beta.sedac.ciesin.columbia.edu/gpw.

GLUCH, R., QUATTROCHI, D. A., and LUVALL, J. C., 2006, A multi-scale approach to urban thermal analysis. *Remote Sensing of Environment*, **104**, 123-132.

GORSEVSKI, V., TAHA, H., QUATTROCHI, D., and LUVALL, J., 1998, Air pollution prevention through urban heat island mitigation: an update on the urban heat island pilot project. Available at http://www.ghcc.msfc.nasa.gov/uhipp/epa_doc.pdf.

HILL, J., DIEMER, C., STOVER, O., and UDELHOVEN, T. H., 1999, A local correlation approach for the fusion of remote sensing data with different spatial resolutions in forestry applications. *International Archives of Photogrammetry and Remote Sensing*, vol. 32, Part 7-4-3 W6, Valladolid, Spain, 3-4 June.

HUANG, C., YANG, L., HOMER, C., WYLIE, B., VOGELMAN, J., and DEFELICE, T., 2001, At-satellite reflectance: a first order normalization of Landsat 7 ETM+ images. Available at http:// landcover.usgs.gov/publications.html.

HUNT, G. R., 1977, Spectral signatures of particulate minerals in the visible and near-infrared. *Geophysics*, **42**, 501-513.

HUNT, G.R., 1980, Electromagnetic radiation: the communication link in remote sensing. In *Remote Sensing in Geology*, B. Siegal and A. Gillespie (Eds), pp.702 (New York: Wiley).

JENSEN, J. R., 2000, Thermal infrared remote sensing. In *Remote Sensing of the Environment: An Earth Resource Perspective*, K. C., Clarke (Ed.), pp.243-283 (Upper Saddle River, NJ: Prentice Hall).

JENSEN, J. R., 1996, Thematic information extraction: Image classification. In *Introductory Digital Image Processing: A Remote Sensing Prospective*, K.C. Clarke (Ed.), pp.197-256 (Upper Saddle River, New Jersey: Prentice Hall).

JIANG, Z., HUETE, A. R., CHEN, J., CHEN, Y., LI, J., YAN, G., and ZHANG, X., 2006, Analysis of NDVI and scaled difference vegetation index retrievals of vegetation fraction. *Remote Sensing of Environment*, **101**, 366-378.

JIN, M., and PETERS-LIDARD, C. D., 2005, Simulating urban heat island effects using an urban scheme coupled with global climate/land-surface models. *Journal of Hydrometeorology*, manuscript.

KAHLE, A. B., MADURA, D. P., and SOHA, J. M., 1980, Middle infrared multispectral aircraft scanner data: analysis for geological applications. *Applied Optics*, **19**, 2279-2290.

KAHLE, A. B., SCHIELDGE, J. P., ABRAMS, M. J., ALLEY, R. E., and LEVINE, C. J., 1981, Geologic application of thermal inertia imaging using HCMM data. *Jet Propulsion Lab, Tech. Rep*. 81-55.

KAWAI, Y., and KAWAMURA, H., 1997, Characteristics of the satellite-derived sea surface temperature in the oceans around Japan. *Journal of Oceanography*, **53**, 161-172.

KEALY, P. S., and GABELL, A. R., 1990, Estimation of emissivity and temperature using alpha coefficients. *Proceedings of the second TIMS Workshop*, *JPL Pub.* **90-95**, pp. 11-15 (Pasadena, CA: Jet Propulsion Laboratory).

KIM, H. H., 1992, Urban heat island. *International Journal of Remote Sensing*, **13**, 2319-2336.

LIU, J. G., 2000, Evaluation of Landsat-7 ETM+ panchromatic band for image fusion with multispectral bands. *Natural Resources Research*, **9**, 269-276.

LILLO-SAAVEDRA, M., and GONZALO, C., 2007, Multispectral images fusion by a joint multidirectional and multiresolution representation. *International Journal of Remote Sensing*, **28**, 4065-4079.

LO, C. P., QUATTROCHI, D. A., and LUVALL, J. C., 1997, Application of high-resolution thermal infrared remote sensing and GIS to assess the urban heat island effect. *International Journal of Remote Sensing*, **18**, 287-304.

LU, D., and WENG, Q., 2006, Spectral mixture analysis of ASTER images for examining the relationship between urban thermal features and biophysical descriptors in Indianapolis, Indiana, USA. *Remote Sensing of Environment*, **104**, 157-167.

MROZ, M., 2000, Radiometric and textural fusion of multiresolution Landsat 7 ETM+ channels for improvement of visual image interpretation and land cover classification. Available at http://www.data-fusion.org/pdf/wkshop/prague02/fusion-mroz.pdf.

MORAN, M. S., 1990, A window-based technique for combining Landsat Thematic Mapper thermal data with higher-resolution multispectral data over agricultural land. *Photogrammetric Engineering and Remote Sensing*, **56**, 337-342.

MODIS Emissivity Library of Institute for Computational Earth Science System (ICESS), University of California, Santa Barbara (UCSB). Available at http://www.icess.ucsb.edu/modis/EMIS/html/em.html.

NICHOL, J. E., 1998, Visualization of urban surface temperatures derived from satellite images. *International Journal of Remote Sensing*, **19**, 1639-1649.

NICHOL, J. E., and WONG, M. S., 2005, Modeling urban environmental quality in a tropical city. *Landscape and Urban Planning*, **73**, 49-58.

ORMSBY, J. P., 1992, Evaluation of natural and man-made features using Landsat TM data. *International Journal of Remote Sensing*, **13**, 303-318.

OWEN, T. W., CARLSON, T. N., and GILLIES, R. R., 1998, An assessment of satellite remotely-sensed land cover parameters in quantitatively describing the climatic effect of urbanization. *International Journal of Remote Sensing*, **19**, 1663-1681.

PINHEIRO, A. C. T., MAHONEY, R., PRIVETTE, J. L., and TUCKER, C. J., 2006, Development of a daily long term record of NOAA-14 AVHRR land surface temperature over Africa. *Remote Sensing of Environment*, **103**, 153-164.

POHL, C., and VAN GENDEREN, J. L., 1998, Multisensor image fusion in remote sensing: concepts, methods and applications. *International Journal of Remote Sensing*, **19**, 823-854.

PRICE, J. C., 1983, Estimating surface temperature from satellite thermal infrared data, A simple formulation for the atmospheric effect, *Remote Sensing of Environment*, **13**, 353-361.

PU, R., GONG, P., MICHISHITA, R., and SASAGAWA, T., 2006, Assessment of multi-resolution and multi-sensor data for urban surface temperature retrieval. *Remote Sensing of Environment*, **104**, 211-225.

QUATTROCHI, D. A., and RIDD, M. K., 1994, Measurement and analysis of thermal energy response from discrete urban surfaces using remote sensing data. *International Journal of Remote Sensing,* **15**, 1991-2022.

ROESSNER, S., SEGL, K., HEIDEN, U., and KAUFMANN, H., 2001, Automated differentiation of urban surfaces based on airborne hyperspectral imagery. *IEEE Transactions on Geoscience and Remote Sensing*, **39**, 1525-1523.

ROSENFIELD, G. H., and FITZPATRICK-LINS, K., 1986, A coefficient of agreement as a measure of thematic classification accuracy. Photogrammetric Engineering and Remote Sensing, 52, 223-227.

ROSENZWEIG, C., SOLECKI, W., PARSHALL, L., GAFFIN, S., LYNN, B., GOLDBERG, R., COX, J., and HODGES, S., 2006, Mitigating New York City's heat island with urban forestry, living roofs, and light surfaces. *Presentation at 86th American Meteorological Society Annual Meeting, Atlanta, Georgia.*

ROTH, M., OKE, T. R., and EMERY, W. J., 1989, Satellite derived urban heat islands from three coastal cities and the utilization of such data in urban climatology. *International Journal of Remote Sensing*, **10**, 1699-1720.

SABINS, F. F., 1987, Thermal infrared images. In *Remote Sensing Principles and Interpretation*, pp. 125-175 (New York: W. H. Freeman and Co.).

SEGL, K., and ROESSNER, S, 1999, Pixel oriented selection of endmember combinations for linear stochastic spectral unmixing applied to urban environments. *Imaging spectrometry V; Proceedings of the Meeting, CO; United States; 19-21 July 1999*. pp. 327-338.

SHEPHERD, J. M., PIERCE, H., and NEGRI, A. J., 2002, Rainfall modification by major urban areas: Observations from spaceborne rain radar on the TRMM satellite. *Journal of Applied Meteorology*, **41**, 689-701.

SMALL, C., 2001, Estimation of urban vegetation abundance by spectral mixture analysis. *International Journal of Remote Sensing*, **22**, 1305-1334.

SMALL, C., 2004, The Landsat ETM+ spectral mixing space. *Remote Sensing of Environment*, **93**, 1-17.

SNYDER, W. C., WANG, Z., ZHANG, Y., and FENG, Y. Z., 1998, Classification-based emissivity for land surface temperature measurement from space. *International Journal of Remote Sensing*, **19**, 2753-2774.

SCHÄDLICH, S., GÖTTSCHE, F.M., and OLSEN, F.S., 2001, Influence of land parameters and atmosphere on Meteosat brightness temperatures and generation of land surface temperature maps by temporally and spatially interpolating atmospheric correction. *Remote Sensing of Environment*, **75**, 39-46.

SOBRINO, J. A., COOL, C., and CASELLES, V., 1991, Atmospheric correction for land surface temperature using NOAA-11 AVHRR channels 4 and 5. *Remote Sensing of Environment*, **38**, 19-34.

SOBRINO, J. A., JIMENEZ-MUNOZ, J. C., and VERHOEF, W., 2005, Canopy directional emissivity: Comparison between models. *Remote Sensing of Environment*, **99**, 304-314.

STATHOPOULOU, M., CARTALIS, C., and PETRAKIS, M., 2007, Integrating Corine Land Cover data and Landsat TM for surface emissivity definition: application to the urban area of Athens, Greece. *International Journal of Remote Sensing*, **15**, 3291-3304.

TOM, V. T., CARLOTTO, M. J., and SCHOLTEN, D. K., 1984. Spatial resolution improvement of TM thermal band data. *Proceedings of the SPIE*: *Applications of Digital Image Processing VII*, **504**, 384-390.

UNITED NATIONS, 2006, World Urbanization Prospects: The 2005 Revision. United Nations. Available at http://www.un.org/esa/population/publications/wup2005/WUP2005 report.htm.

US CENSUS BUREAU, 2000, United States Census Bureau 2000. Available at http://www.census.gov/geo.

VALOR, E., and CASELLES, V., 1996, Mapping land surface emissivity from NDVI: application to European, African, and South American areas. *Remote Sensing of Environment*, **57**, 167-184.

VAN DER MEER, F. D., 2001, Basic Physics of Spectrometry, In *Imaging Spectrometry,* van der Meer F. D. and de Jong S. M. (Eds.). pp. 3-16. (Netherlands: Kluwer Academic Publishers).

VANI, K., and SANJEEVI, S., 2001, Fusion of ASTER image data for enhanced mapping of Landover features. Available at http://www.gisdevelompment.net/application /environment/pp/envp0005pf.htm.

VOOGT, J. A., and GRIMMOND, C. S. B., 2000, Modeling surface sensible heat flux using surface radiative temperatures in a simple urban area. *Journal of Applied Meteorology*, 39, 1679-1699.

VOOGT, J. A., and OKE, T. R., 1997, Complete urban surface temperatures. *Journal of Applied Meteorology*, **36**, 1117-1132.

VOOGT, J. A., and OKE, T. R., 2003, Thermal remote sensing of urban climates. Remote Sensing of Environment, 86, 370-384.

WAN, Z., and DOZIER, J., 1996, A generalized split-window algorithm for retrieving land-surface temperature from space. *IEEE Transcations on Geoscience and Remote Sensing*, **34**, 892-905.

WATSON, K., 1992, Spectral ratio method for measuring emissivity. *Remote Sensing of Environment*, **42**, 113-116.

WENG, Q., 2001, A remote sensing-GIS evaluation of urban expansion and its impact on surface temperature in the Zhujiang Delta, China. *International Journal of Remote Sensing*, **22**, 1999-2014.

WENG, Q., LU, D., and LIANG, B., 2006, Urban surface biophysical descriptors and land surface temperature variations. *Photogrammetric Engineering and Remote Sensing*, **72**, 1275-1286.

WENG, Q., and QUATTROCHI, D. A., 2006, Thermal remote sensing of urban areas: An introduction to the special issue, *Remote Sensing of Environment*, **104**, 119-122.

WILBER, A. C., KRATZ, D. P., and GUPTA, S. K., 1999, Surface emissivity maps for use in satellite retrievals of longwave radiation. NASA/ TP-1999-209362, National Aeronautics and Space Administration, Langley Research Center, Hampton, Virginia 23681-2199. Available at http://techreports.larc.nasa.gov/ltrs/PDF/1999/tp/NASA-99-tp209362.pdf.

WU, L., 1996, An integration of a surface energy balance climate model with TIN and GRID in GIS. *Third International Conference/Workshop on Integrating GIS and Environmental Modeling, Jan 1996, Santa Fe, NM, USA*. Available at http://www.ncgia.ucsb.edu/conf/SANTA_FE_CD-ROM/sf_papers/wu_lin/wu_lin.html.

XIAN, G., and CRANE, M., 2004, Evaluation of urbanization influences on urban climate with remote sensing and climate observations. *American Geophysical Union, Fall Meeting 2004*. Available at http://www.isprs.org/commission8/workshop_urban/xian.pdf.

YANG, J., and WANG, Y. Q., 2001, Estimation of land surface temperature using Landsat-7 ETM+ thermal infrared and weather station data. Available at http:// www.ltrs.uri.edu/LST_page/paper4.doc.